Computational Modeling of Optical Projection Tomographic Microscopy

Ryan L. Coe

A dissertation
submitted in partial fulfillment of the
requirements for the degree of

Doctor of Philosophy

University of Washington

2013

Reading Committee:

Eric J. Seibel, Chair

Ruikang K. Wang

Paul A. Wiggins

Program Authorized to Offer Degree:
Department of Bioengineering

University of Washington

Abstract

Computational Modeling of Optical
Projection Tomographic Microscopy

Ryan L. Coe

Chair of the Supervisory Committee:
Professor Eric J. Seibel
Department of Mechanical Engineering

Lung cancer is the leading cause of cancer related deaths worldwide with 1.37 millions deaths per year. In 2011, Computed Tomography became the first method approved for early detection, however it is hindered by safety concerns due to its use of radiation and it is only capable of detecting masses greater than 2mm in diameter. In an effort to perform early detection before masses are visible, VisionGate Inc. is developing a microscope based on Optical Projection Tomographic Microscopy (OPTM) to detect cancer at the cellular level. OPTM reconstructs three-dimensional images of single cells from projection images acquired from different perspectives around the cell. This dissertation presents a computer simulation that is designed to analyze all aspects of OPTM image formation, such as degree of specimen staining, refractive index matching, and objective scanning. The computer simulation is used in conjunction with experimental methods to refine conclusions and improve system design in a robust methodology. While this work is currently driving improved microscope design, in the long term it will provide a framework to develop quantitative microscopy where pixel values are directly related to cellular optical properties. These improvements will provide improved sensitivity and specificity for early detection and ultimately reduce lung cancer mortality.

TABLE OF CONTENTS

LIST OF FIGURES

LIST OF TABLES

ACRONYMS

AFP	Analytical Field Propagation
CCD	Charge-coupled device
CT	Computed Tomography
CPML	Convolutional Perfectly Matched Layer
DFT	Discrete Fourier Transform
EM	Electron Microscope
FEM	Finite Element Method
FOV	Field of View
MOM	Method of Moments
MPI	Message Passing Interface
NA	Numerical Aperture
NTFF	Near-to-far Field
NTNF	Near-to-near Field
OCT	Optical Coherence Tomography
OPTM	Optical Projection Tomographic Microscopy
PEC	Perfectly Electric Conducting
PSF	Point Spread Function

PTV	Peak-to-valley
PWS	Partial Wave Spectroscopy
ROC	Receiver Operator Curve
RI	Refractive Index
SSE	Sum Squared Error
TFSF	Total Field Scatter Field
1D	One-dimensional
2D	Two-dimensional
3D	Three-dimensional

ACKNOWLEDGMENTS

Foremost, I would like to express my deep appreciation for the guidance, encouragement, and continuous support provided by my advisor, Professor Eric Seibel. Eric allowed me the opportunity to grow profesionally as a scientist and engineer both inside and outside of lab by always having my best interests in mind. He allowed me to attend seminars and conferences throughout the country and even opened the door for an internship that took me away from my research for three months. Beyond my scientific development, he was fully supportive of my desire to develop business acumen through additional classes and projects that at times hindered my research progress. Besides my advisor, I would like to thank the rest of my committee: Professor Vikram Jandhyala, and Professor John Sahr, Professor Ruikang Wang, and Professor Paul Wiggins, for their encouragement, insightful comments, and direction.

I am grateful to Michael Meyer, Jon Hayenga, and Alan Nelson of VisionGate Inc. for their insightful comments and the use of the Cell-CT imaging device. Furthermore, I am thankful for the experimental setup and support work provided by the VisionGate staff, including Christy Lancaster, Wayne Breidford, Ryland Bryant, David Steinhauer, Sarah Shimer, and Ben Hawthorne. The entire Human Photonics Laboratory contributed to important discussions and guided my development throughout this project.

The National Science Foundation awarded me with financial support to pursue this work uninhibited for three years through the Graduate Research Fellowship Program on grant DGE-0718124 and grant CBET-1014976. Their financial support allowed me to pursue many personal and career development activities throughout my studies that would have been otherwise impractical.

Graduate school has been an undeniable once-in-a-lifetime opportunity where I have explored the world and grown as an individual. I appreciate all of the friends I have made and the people who have impacted my life. I am especially thankful to have met Catherine Louw who has provided me with so much love and support. She has impacted my life in a way I never could have imagined and I am excited for our life-long journey together.

My parents, Steve & Roxann, and brother, Ross, have been a source of unwavering support and I am completely indebted to the generosity and persistent selflessness that they have shown me through out my entire education. Despite our many moves, the number one requirement growing up was to live in an area with the absolute best schools. My parents always believed that mine and my brother's education was the number one priority. They always pushed me to work harder, pursue better opportunities, and they were always there when things weren't going the right way. Without their support this acheivement would not have been possible.

DEDICATION

to my parents

Chapter 1

INTRODUCTION

1.1 Significance

Lung cancer is the leading cause of cancer-related deaths worldwide with approximately 1.37 million deaths each year [127]. Currently, patients presenting with symptoms associated with lung cancer are referred for expensive, radiation-based Computed Tomography (CT) scans or chest radiographs to determine the cause. If a mass is detected using either of these techniques, the patient then undergoes an invasive bronchoscopy procedure to image and biopsy the mass. Following the biopsy, a cytopathologist fixes the cells and performs optical microscopy of the histological sections using Hematoxylin and Eosin (H&E) stain. This procedure is qualitative and cancer diagnoses are determined by expert opinion rather than as a quantitative decision, which inherently introduces some intrinsic error into the system. Under this paradigm, two-thirds of lung cancer cases are currently diagnosed after they have already reached the metastatic stage [48]. This fact is even more troubling since the 5-year survival rate of patents with Stage II-IV cancer ranges from 5-40% [84].

New evidence shows that screening for lung cancer using CT promotes a 20% reduction in mortality compared with screening based on x-ray alone [1]. While this conclusion puts to rest the debate concerning the clinical effectiveness of lung cancer screening, CT is hindered by its high cost [1] and the large number of false positives

due to its increased sensitivity compared to chest x-rays. These criticisms present the opportunity for another, less expensive technique with reduced harmful effects. Potential early detection procedures should take into account that asymptomatic patients will be especially cost adverse and any procedure must have high sensitivity and specificity or it will not be diagnostically relevant. Rather than continuing to detect lung cancer and other diseases on the macroscopic scale, detection could be performed at the microscopic scale before macroscopic tumors are detectable on CT or chest radiography.

Several studies have shown that cancer develops in a multistage pathway where cells exhibit morphological changes individually before a larger mass forms [132]. These morphological changes are known as biomarkers, which come in a variety of forms including decreased cytoplasm-to-nucleus ratio and nuclear membrane indentations [45]. Based on this understanding, a potential procedure could detect lung cancer biomarkers in sputum cells for evidence of pre-neoplastic cells or cancer cells. Sputum is a mixture of mucus, saliva, and cells dislodged from the lung epithelium [94]. Böcking showed that 85.4% of the sputum from cancer bearing hosts have abnormal cell morphologies [6] and Neumann *et al.* demonstrated that the cancer cell occurrence rate in sputum is similar irrespective of various diagnostic criteria: Squamous Carcinoma vs. Adenocarcinoma, Stage I versus Stage IV cancer, and others [88].

1.2 Lung Cancer Pathology

Lung cancer arises in the pulmonary system as a group of neoplastic cells, either as a primary tumor or metastases. While lung cancer is strongly linked to smoking, 15% of cases occur in nonsmokers [117] and remains a health issue despite small decreases in diagnoses over the past 20 years [51]. Epithelial lung cancer is classified into four primary cell types: squamous cell carcinoma, small cell carcinoma (middle column of Fig. 1.1), large cell carcinoma (right column of Fig. 1.1), and adenocarcinoma [76, 125]. Each subdivision has a distinct etiology, pathology, characteristic histological features, treatment regimes, and prognosis. However, clinically there is one main distinction between small cell carcinomas and the other three cell types (often referred to as non-small cell) because only small cell cancers respond to chemotherapy. The remainder of cell types must be surgically removed.

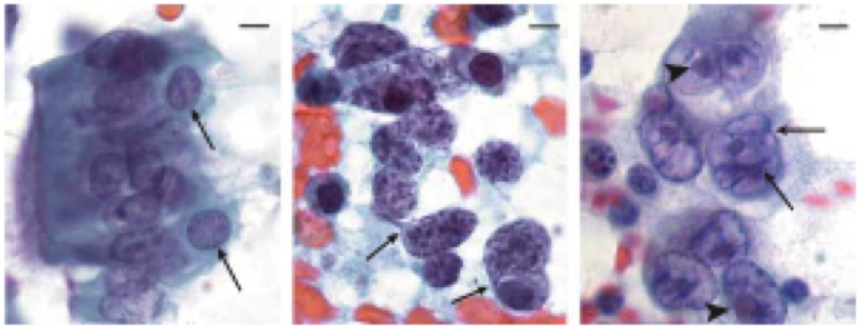

Figure 1.1: Hematoxylin and Eosin stained normal lung epithelial cells (left), small-cell lung carcinoma (middle), and large-cell lung carcinoma (right) [36].

Small cell carcinoma and squamous cell carcinoma are the two most prevalent types of lung cancer, accounting for approximately 20-30% and 30-40% of all lung cancers, respectively. Small cell carcinoma is normally identified by a low cytoplasm-

to-nucleus ratio, which contains a higher percentage of dark blue to pink with H&E staining as seen in Fig. 1.1 [128]. Additionally, small cell carcinoma exhibits clumping of chromatin within a floppy nuclear-envelope rather than a distinct nucleolus [36]. Squamous cell carcinoma, on the other hand, commonly grows in the central areas of the lung and is found histologically in a wide range of states, from well differentiated to anaplastic [62]. The nucleus of squamous cell carcinoma type cells is similar to small-cell lung cancer, where the nucleoli is inconspicuous [36]. Due to the centralized growth locations of both small cell carcinoma and squamous cell carcinoma, they are often seen together in sputum histology.

1.3 Microscopic Detection Techniques

1.3.1 Two-Dimensional Microscopy

Over the last hundred years, two-dimensional (2D) optical microscopy of biopsy and cellular specimens has become the gold standard for disease diagnosis [36]. Microscopic images of cells and tissue are correlated to clinical outcomes, forming the basis of clinical pathology. For cancer diagnosis based on tissue specimens, pathologists routinely image at low magnification to determine tissue architecture [3]. Higher magnification is typically required for isolated cells, as cytological analysis relies on viewing the morphology, densitometry, and texture of the chromatin within the nucleus [66, 123]. Image contrast from light transmittance is provided by absorptive and counter stains to the chemically fixed cells. These stains reveal certain morphological signatures in the cells that guide various clinical objectives. For example, the stain used in the Pap test has helped to reduce the cervical cancer mortality rate from

the leading cause to now the eighth most common cause of cancer death for women [36]. Also, H&E continues to be the standard contrast agents for diagnostic surgical pathology [50, 38]. Another contrast mechanism is provided by fluorescence where molecular probes bind to specific cellular components. Unfortunately, both cost and tradition have inhibited their use in diagnostic procedures where doctors are more comfortable with absorptive stains.

Optical microscopy is constrained by the diffraction limit, which limits the resolution of standard bright-field microscopes to ~200 nm laterally and ~700 nm axially. These limits are a hindrance for early detection of nanoscopic cellular changes exhibited in cells prior to becoming pre-neoplastic [2, 70]. The purely 2D perspective has also been shown to hinder diagnostic capabilities [79]. Early techniques to improve resolution worked within the diffraction limit by reducing the ray's wavelength, leading to discoveries like the electron microscope (EM) with resolutions below 0.5Å [33]. However, the combination of exorbitant costs and toxic fixation procedures has reduced its applicability to purely research related fields.

Resolution has also been improved by altering the point spread function (PSF) of the system, which is the inherent blurring of a point source when imaged using an optical device. For example, the confocal microscope improves the PSF by the use of a laser light source and a spatial pinhole to reject out-of-focus light; however, its throughput is limited since the light source and pinhole must be scanned throughout the entire field-of-view (FOV). These throughput problems limit the use of 2D confocal microscopy in clinical applications.

1.3.2 Three-Dimensional Microscopy

In an effort to eliminate the problem of imaging cells on a single plane, many 3D microscopy techniques have been developed. Confocal microscopy, for example, has been expanded to the third dimension and has become the conventional form of 3D optical microscopy in research [83]. However, clinical practice has not moved into the third dimension for disease diagnosis, due to the expense involved with confocal equipment, technical difficulties associated with use, and because transmission confocal microscopes cannot utilize absorptive stains [30, 129]. 3D confocal microscopy is also limited by anisotropic images where the degradation in axial resolution hinders quantitative computer-aided analysis. Within the last decade, there have been tremendous advances in 3D optical microscopy bringing unprecedented spatial resolution [39, 44, 47, 53], but their high cost, low throughput, and reliance on fluorescence present significant barriers to entry into the clinical fields of pathology and cytology.

Techniques have been proposed for generating 3D images based on the method of computed tomography (CT). Three important criteria make this technology feasible: first, the ability to image absorptive stains as well as fluorescence from fixed cells; second, to provide high throughput for imaging thousands of cells to make a diagnosis for an entire specimen; and third, to be cost effective in dollars per sample analyzed. The use of CT techniques in 3D optical microscopy is also able to overcome the anisotropy in spatial resolution of all single-perspective optical microscopes (limited NA objective lens), such as confocal microscopy [39]. Advanced optical 3D imaging techniques can provide isometric resolution by imaging from multiple perspectives.

One technique involves scanning a beam of light through a stationary specimen

from different angles of incidence [56, 57, 64, 87]. This method allows for rapid image acquisition times due to fast optical scanning, which is ideal for live cells and tissues [17, 114]. However, the use of a single objective lens to deliver all the scanned beams, requires *a priori* assumptions about the specimen for performing the 3D reconstruction, and there remains some degradation in the axial resolution versus the lateral resolution. Alternatively, multiple objective lenses can surround the specimen to compensate for the reduction in axial resolution in any single lens [58, 111]. This method increases signal collection for weak fluorescence imaging with a significant increase in cost and complexity. Optical Projection Tomography rotates the specimen within a transmission optical imaging system that remains stationary [10, 59, 106]. The necessity of rotating the specimen makes this technique less attractive for imaging live cellular organisms, but it also eliminates the risk of biohazard where disease diagnosis is made after the cellular specimen is fixed.

1.3.3 Flow and Image Cytometry

Flow cytometry has long been the standard for high throughput cell analysis by combining optical scattering with the principles of hydrodynamic focusing. Flow cytometers analyze hundreds of cells in a matter of seconds by measuring both forward and side light scatter from fluorescently labeled molecules. However, the main disadvantage of flow cytometry is that morphology, structure, and subcellular localization are all important features that are lost without actual images [91]. According to several authors, microscopes of the future will incorporate flow cytometry allowing for high throughput image acquisition of single cells [91, 110]. This combination could

prove to be a significant improvement for diagnostic medicine. The idea of imaging cytometry is not necessarily new; however, only recent technological advances are making this idea come to fruition [4]. In this manner, large sample sizes may be imaged in a matter of seconds without the loss of morphology, structure, and subcellular localization. The problem with these techniques, however, relates back to one of the problems with 2D microscopy: the single plane perspective skews cell morphology and impairs diagnosis.

1.4 Optical Projection Tomographic Microscopy

Optical Projection Tomographic Microscopy (OPTM) is a novel three-dimensional (3D) imaging technology being developed at the University of Washington, Arizona State University, and Cornell University for the early detection and diagnosis of disease, such as lung cancer, from cellular samples [81]. Motivation for developing OPTM is provided, in part, by a three-fold reduction in false negative rates for diagnosing cancer in a controlled comparison of 3D versus two-dimensional (2D) images of the same cells using automated classifier analysis [79]. For individual and isolated cell analysis, VisionGate Inc. (Phoenix, AZ) is commercializing OPTM for early disease detection using sputum as the cellular sample. The instrument is referred to as the optical Cell-CT (trademark of VisionGate) because 3D cell images are reconstructed from 2D optical projections analogous to that of X-ray Computer Tomography (CT) [35].

The 3D OPTM images are reconstructed from standard 2D bright field microscope images, acquired over multiple projections by rotating a micro-capillary around its

central axis. A simplified diagram is shown in Fig. 1.2. Cells are fixed, stained, and immersed in a solution of optical gel, and pushed through a micro-capillary that passes between a condenser and objective. Once a cell is within the FOV, flow is arrested so that projections can be acquired. At each step in rotation, the focal plane is scanned through the cell, leaving the camera (CCD) shutter open to obtain a single optical projection by optically integrating through the entire cell. The micro-capillary (and cell) is rotated to the next position and another projection is acquired. After projections are acquired from all desired angles, a 3D image is reconstructed using the filtered backprojection method [54] and visualized on a computer monitor.

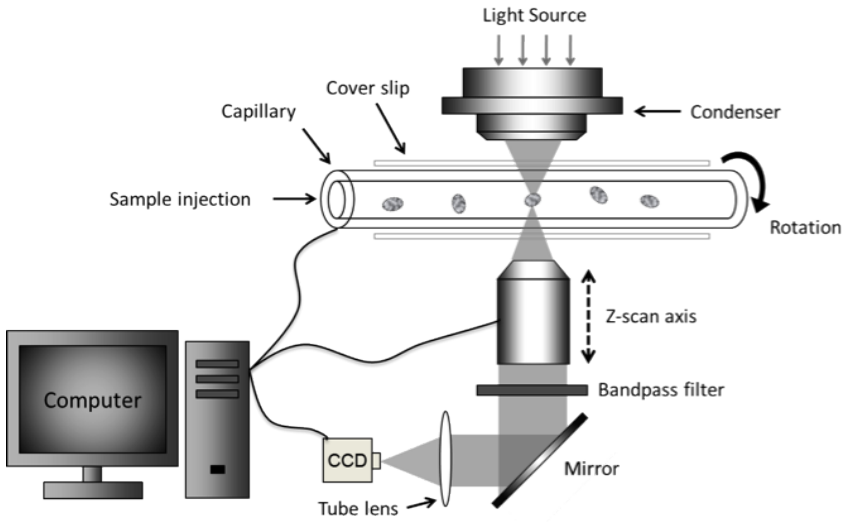

Figure 1.2: Diagram of the image formation process utilized in OPTM where projection images are produced by scanning the focal plane of the objective to optically integrate through the cell. Projections are acquired from desired angles by rotating the micro-capillary between the condenser and objective and reconstructions are calculated using the filtered back-projection and visualized on a computer monitor.

While theoretically possible to image cells over 180°, practical experience shows that residual refraction and scattering produce images at 0° and 180° that depart

from the mirror image ideal. To average these differences, cells are imaged over 360°. Various commercial applications of the Cell-CT device require different resolutions in the 3D image. For research, a total of 500 projections are typically acquired over 360° equating to a rotational step of 0.72° between projection acquisitions. The objective focal plane scanning is determined *a priori* in accordance with the size of the cells being imaged. For example, lung epithelial cells are approximately 10 μm in diameter, so the scan distance is set to 12 μm. The micro-capillary has a similar refractive index as the optical gel and index-matching immersion fluid such that its cylindrical geometry is transparent and non-refractive [35].

An example dual-stained alveolar macrophage image produced by the Cell-CT is shown in Fig. 1.3 [89]. Alveolar macrophages can be an indicator of gastroesophageal reflux disease where reflux can cause stomach contents to enter the lungs. In the lungs, reflux is phagocytosed by alveolar macrophages and presents as lipid droplets inside the cells. The cell in Fig. 1.3 was dual-stained with Hematoxylin and the lipid stain Oil-Red-O and imaged to capture the color of the two stains.

1.5 Lung Cancer Diagnosis

The possibility of the Cell-CT to provide high-speed, automated classification of specimens based on 3D imaging represents its most significant potential. 3D imaging represents cells comprehensively, thus eliminating slice selection and perspective biases. These biases can result in classification errors causing disease ridden patients to be not detected or disease free patients to be identified for unnecessary follow up procedures. Meyer *et al.* assessed the potential for reducing error rates in specimen classification

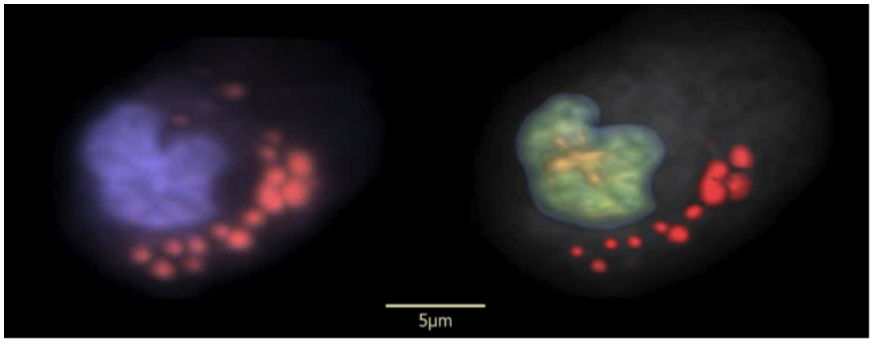

Figure 1.3: Dual-stained alveolar macrophage imaged with a color CCD using the Cell-CT. On the left, the cell is rendered with a maximum intensity projection and on the right, the cell is volume rendered with color and opacity adjusted to better illustrate cell features of interest. The cytoplasm is represented as a white cloud. The lipid droplets within the cytoplasm show up in bright red. The cell nucleus is imaged with the nuclear envelope and loose chromatin in translucent blue-green. Condensed chromatin within the nucleus was imaged in opaque orange.

by imaging a set of normal and abnormal cells in 2D and 3D using OPTM. The study shows a dramatic increase in the area under the receiver operator curve (ROC) for 3D analysis over the 2D analysis [79]. Also, 3D image analysis opens the potential for a new set of features that can only be assessed in 3D using an automated classification system [80]. For example, nuclear invaginations in cancerous cells can only be verified in 3D [52].

Fig. 1.4 shows the progression of features from normal cellular morphology to cancer in three sputum cells imaged by the Cell-CT. The cells are stained with Hematoxylin and the images are false colored to better depict cell features. A normal squamous metaplastic epithelial cell is shown in the top row. The middle row shows a moderate dysplasia cell and the last row shows a squamous carcinoma cell. As dysplasia progresses, the cytoplasm shrinks, the nucleus enlarges, and the cell chromatin becomes more irregularly distributed throughout the nuclear compartment.

This process illustrates basic cytological features that have been known about for 100 years.

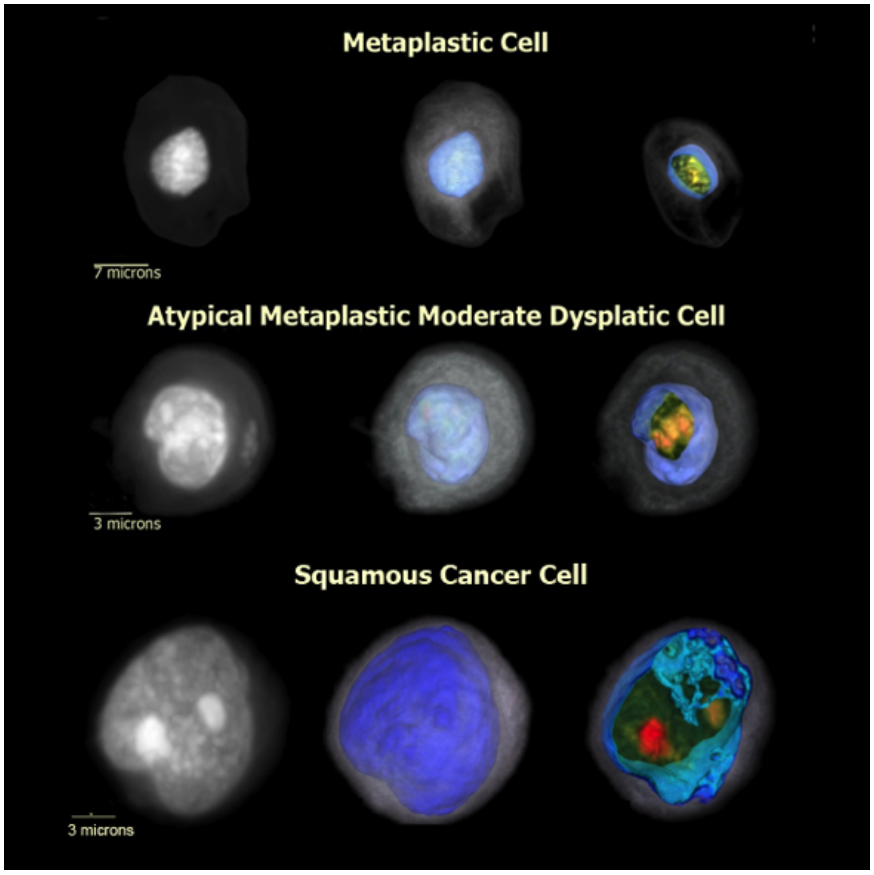

Figure 1.4: A normal metaplastic epithelial cell (top row), a moderate dysplatic cell (middle row), and a squamous carcinoma cell (bottom row). The left most images show the cell in maximum intensity projection. The middle column shows the volume rendered to include added color and opacity to better visualize cell features: cell cytoplasm (translucent white), nuclear wall (opaque blue), nucleoplasm (translucent green), and condensed chromatin (opaque red). Finally, on the right, the cell is cropped to reveal inner nuclear detail. The figure shows the dramatic changes in cell morphology as the cell makes its way through the process of dysplasia and on to adenocarcinoma.

1.6 Motivation and Specific Aims

While OPTM has already shown its diagnostic capabilities [79], it could have a greater impact if it were transformed into a quantitative device where pixel values are directly correlated with specimen properties. Clinicians would no longer qualitatively decide whether disease is present or not; instead a quantitative metric would diagnose disease, which should lead to higher sensitivity and specificity. Quantitative microscopy has been proposed previously [131], but the large number of variables associated with both the microscope and the sample make this a difficult proposition. For example, filament intensity variations, ambient light, and staining variations highlight just a few of the many variables that affect the final image. Rather than attacking this problem experimentally, computational modeling provides the opportunity to precisely vary individual parameters, which would otherwise be difficult to decouple from one another.

Recently, the role of simulations in developing quantitative microscopy has gained traction among different research groups [9] leading to many publications. For example, simulations played a fundamental role in correlating scattering coefficients with refractive index (RI) in Partial Wave Spectroscopy (PWS) [113], analyzing spectral variations in microspheres [16], and analyzing scattering produced by a biological cell from a focused Gaussian beam [109]. In each case, the simulations provided increased understanding of the underlying results that would otherwise have been difficult to interpret.

Simulations of OPTM could evaluate the effects of diffraction, refraction, and absorption on the reconstruction of 3D images of standards, such as microspheres

and micro-shells. The theoretical model would also provide a framework to quantify system errors and inconsistencies, including nonlinear scanning of the objective, hysteresis in focal-plane scanning and cell motion. All of these analyses could eventually lead to quantitative OPTM. The formal long-term goal and specific aims to begin accomplishing this goal are as follows:

Long-term Goal: Transform the Cell-CT into an automated quantitative microscope, capable of improving early detection of lung cancer through the quantification of biomarkers. Quantification would translate into superior automated biomarker recognition by statistically removing optical (e.g., diffraction and refraction), mechanical (e.g., rotation of the micro-capillary and objective scanning), and sample (e.g., H&E quality of staining) differences from the reconstructed images that would otherwise impair automated biomarker detection.

Specific Aim 1: Develop a more accurate algorithm to compute near-field electromagnetic radiation outside a limited computational domain. Numerically calculating electromagnetic wave propagation is computationally intensive in certain aspects. In order to mitigate this problem, scattering is often computed inside a limited computational domain around the cell and then mapped to points outside the domain. The method developed under this aim provides a better opportunity to limit the computational domain while producing the most accurate possible results.

Specific Aim 2: Develop a computer model to simulate images of arbitrary objects to examine the effect of optical, mechanical, and sample parameters on reconstructed 3D images. The computer model simulates projection images acquired by OPTM and reconstructs them into 3D images. The model is used to examine optical effects, such as refraction, and mechanical effects, such as objective scanning, on the final reconstructions.

Specific Aim 3: Develop an alternative illumination algorithm to simulate microsphere images in a computationally efficient method. The computational model developed in Aim 2 has the ability to image arbitrary objects, but its computational cost is quite high. An alternative method capable of simulating images of microspheres using a computationally efficient algorithm is provided and allows examination of mechanical effects such as micro-capillary rotation that would otherwise be prohibitive.

Specific Aim 4: Experimentally validate the computer model by comparison of simulated and experimentally produced reconstructions of known objects. The computer models developed in Specific Aims 2 and 3 are verified through experimental means for the purposed of validating their use in more difficult simulations. These simulations will eventually provide a means of evaluating independent factors that cannot be decoupled experimentally.

Chapter 2

IMPROVED NEAR FIELD CALCULATIONS

2.1 Background

The Finite Difference Time Domain (FDTD) method provides a simple and accurate solution to Maxwell's curl equations for arbitrary objects in which an analytical solution does not exist. Unfortunately, FDTD requires discretization of light waves at high resolution, requiring at least twenty cells per wavelength where each cell contains six vector components (three electric and three magnetic). Despite implementing the algorithm on large core, unified memory computers or distributed memory computer clusters, the computational cost is unreasonable for 3D spatial domains any larger than tens (maybe hundreds) of wavelengths, even on a super computer [120].

To overcome these computational limitations, FDTD is commonly used to calculate scattering within a limited volume that encloses an object of interest and then an alternative method is used to determine the electromagnetic fields at points outside the computational grid. These methods have been generalized into two main categories: Near-To-Near Field (NTNF) and Near-To-Far Field (NTFF) transformations. The difference between these two methods is simply the distance from the FDTD grid to the observation point, which determines whether certain far field approximations can be used or not. In general, NTNF and NTFF transformations operate in much the same way where the object of interest is enclosed by an artificial surface, which

the electromagnetic waves pass through. The fields calculated at the artificial surface are individually weighted based on their relative position to an arbitrary observation point before being integrated to provide the total response. This idea of an integral based transformation to observe electromagnetic radiation outside the FDTD lattice was originally presented in two-dimensions by Umashankar *et al.* [124] and later expanded to three-dimensions [116].

One of the main difficulties in implementing the artificial surface in FDTD is the fact that the electric and magnetic fields are located at different temporal and spatial locations. The magnetic fields are temporally located at a half time step difference compared to the electric fields and none of the six vector components are located at the same position. While temporal differences are easily accounted for by a simple phase correction, spatial differences make it impossible to obtain a single integration surface directly from FDTD. Most implementations obtain a single surface by interpolating between two adjacent magnetic fields slightly inside and outside the electric field surface so as to obtain magnetic fields, which lie on the electric field surface.

Interpolation between two magnetic field surfaces was originally performed using the arithmetic mean, but this method introduces phase errors, especially for high frequency content and in the backscatter direction of a strongly forward scattering object [99]. Reduction of phase errors can be achieved by interpolation using the geometric mean, first introduced for impedance calculations [34] and later applied to the NTFF transformation [99]. In fact, phase errors theoretically should be completely eliminated for plane waves using the geometric mean; however, limitations in numerical precision and sampling rate for high frequency content are inherent drawbacks in

any implementation and result in some degree of numerical inaccuracy. Furthermore, unlike the arithmetic mean, these surfaces can only be averaged following completion of the FDTD time stepping, thereby increasing the computational and storage cost.

Alternatively, Martin proposed using two separate surfaces that were postulated to produce even better results than interpolation methods [71]. This method received little recognition until a recent publication showed its accuracy for strongly forward scattering objects [72]. Borrowing ideas from the Huygens's sources, Martin acquires electric fields from their regular positions, but assumes they come from the magnetic field's position during the weighting process. The opposite is also true where the magnetic fields are acquired from their regular position but assumed to be located on the electric field surface. This idea of switching calculated and perceived locations reduces the computational and storage costs required for two separate magnetic fields. To date this method has only been utilized in far field formulations that ignore the vector components normal to the surface of integration.

The majority of electromagnetic scattering applications only require far field calculations. Typical applications include the radar cross section of antennas, planes, or boats [93], circuit board analysis [20], or low numerical aperture (NA) microscopy simulations [16]. However, in some cases near field calculations are required. One such example is the simulation of a high NA microscope [121]. In the simulation of images of biological cells produced by a high NA microscope, where cells are strongly forward scattering objects, phase errors could be a major limitation, especially in the backscatter direction. With this idea in mind, a more accurate implementation of near field scattering calculations could provide major advancements in the simulation

of reflection based high NA microscopes. Application of the mixed surface to near field transformations could build upon the improved accuracy offered by the geometric mean at reduced computational and storage costs. Improvements in simulation tools could have a profound impact on our ability to understand the effect of certain organelles on light scattering [31]. Detection of subcellular changes such as organelle size could improve sensitivity and specificity when diagnosing diseases, such as cancer [60].

Several methodologies have been developed to determine the near field scatter pattern including the vectorial integral theorem of Kirchhoff, the vectorial Rayleigh-Sommerfeld theory, and the Stratton-Chu integrals. Interestingly the Kirchhoff and Rayleigh-Sommerfeld theories may be obtained from the Stratton-Chu integrals thus it is the more general of the three approaches [121]. For this reason a vectorial version of the mixed surface is applied to the Stratton-Chu diffraction integrals and compared to both the arithmetic and geometric means in near field calculations from FDTD derived scattering. The method described is applied to a single sphere and an ensemble of flow cytometry calibration standards, where the single sphere has a well-known analytical solution, known as the Mie Series [82]. The ensemble of flow cytometry calibration standards provides a practical example that produces a meaningful diffraction pattern. Both examples set the stage for developing a more accurate microscopy simulation tool that could improve the early detection of disease.

Background and Considerations

Near and far field transformations have been developed for both the time and frequency domains [115]. Selection of one domain over the other requires consider-

ation of the tradeoffs associated with each for a given implementation. The time domain formulations run concurrently with the FDTD simulation to allow the fields to be calculated for a specific observation point or a relatively small number of points for wide-band incident light [115]. These methods allow you to see how the fields change over time for pre-determined observation points. If another observation point is desired after the fact then the entire FDTD simulation must be rerun, which is an obvious disadvantage. The main problem with these methods is that they have relatively large storage and computational costs. On the other hand, frequency domain formulations provide a means to determine the fields at a large number of observation points for a small number of frequencies [67, 115]. In most implementations, a Discrete Fourier Transform (DFT) runs concurrently with the FDTD simulation over the surface of integration. Following completion of the simulation, the fields on the surface are utilized to determine the electromagnetic fields at any desired observation point. The frequency domain methods have relatively small storage and computational costs because the DFT requires storage of only two values (real and imaginary parts) for each desired frequency for each point on the surface of integration. Unfortunately most implementations require that the entire simulation be complete prior to looking at the fields, though in some cases windowing has been used to look at the response over time, but this requires additional computational cost [96, 115].

In the far field ($kr \gg 1$, where k is the wavenumber and r is the distance), the scatter pattern can be constructed using scalar approximations in the weighting process that allow the entire transformation to be treated as a superposition of plane waves. Additionally, the use of plane waves eliminates the need to compute the radial

components of the electromagnetic fields, since there is no electric field component in the direction of propagation for a plane wave. This approximation substantially simplifies the transformation. However, as the distance to the observation point is decreased coming closer to the near field, these scalar approximations are not accurate and the waves must be treated as spherical waves instead. In this case, there is an electric field component associated with the direction of propagation. It is important to note that NTNF methods can be used for far field calculations as well, but they do not provide improved results so the additional computational cost is not worth the trade-off.

2.2 Mixed Surface Near To Near Field Transformation

The Stratton-Chu integrals are derived from a combination of Gauss's Divergence theorem and vector analogs of Green's first and second identities. The vector variants are essential for computation of the near field electromagnetic radiation pattern. This vector diffraction theory was originally presented as a means to calculate electromagnetic fields inside a closed surface provided the surface does not contain any sources or sinks of radiation. Over the years, this theory has been expanded to allow for field calculations on the surface of integration as well as outside of the surface [49, 120]. The so-called modified formulation is utilized, allowing electromagnetic fields to be calculated outside the surface. Readers interested in the derivation are invited to

refer to [120]. The Stratton-Chu integrals utilizing the $exp(-j\omega t)$ time variation are:

$$\begin{aligned}\mathbf{E}(r_P) &= -\oiint_S [j\omega\mu\,(\hat{n}\times\mathbf{H})\,G(r_S,r_P) - (\hat{n}\times\mathbf{E})\times\nabla G(r_S,r_P) \\ &\quad -(\hat{n}\cdot\mathbf{H})\,\nabla G(r_S,r_P)]\,dS' \end{aligned} \tag{2.1}$$

$$\begin{aligned}\mathbf{H}(r_P) &= \oiint_S [j\omega\mu\,(\hat{n}\times\mathbf{E})\,G(r_S,r_P) - (\hat{n}\times\mathbf{H})\times\nabla G(r_S,r_P) \\ &\quad +(\hat{n}\cdot\mathbf{E})\,\nabla G(r_S,r_P)]\,dS' \end{aligned} \tag{2.2}$$

where $\hat{n}$ is the outward surface normal, $G(r_S, r_P)$ is the free-space Green's function:

$$G(r_s, r_P) = \frac{\exp\left(-jl\,|r_s - r_p|\right)}{4\pi\,|r_s - r_p|} \tag{2.3}$$

$$|r_s - r_p| = \sqrt{(x-x_p)^2 + (y-y_p)^2 + (z-z_p)^2} \tag{2.4}$$

with $r_P = (x_p, y_p, z_p)$ being the observation point and $r_S = (x, y, z)$ being the coordinates of the fields on the surface of integration S. The first two terms of Eqs. 2.1 and 2.2 are similar to the standard NTFF transformation, except they are often referred to as equivalent electric and magnetic currents. The dot product in the third term of the integrals is the source of the normal component that is not normally seen in NTFF transformations, which requires expansion of the original mixed surface technique presented by Martin [71].

In order to better understand the deployment of these equations in FDTD, it is assumed these equations will be implemented as a box surrounding the object of

interest. As an example, Fig. 2.1 and Fig. 2.2 show the FDTD electromagnetic fields around the $\hat{n} = -\hat{z}$ face on the surface of integration. Fig. 2.1 shows the fields necessary for the interpolation methods, while Fig. 2.2 shows the fields necessary for the mixed surface approach. The fields represented in these figures project spatial half-cell variations in the x-direction onto a single plane with the fields on the x-plane as dark black and the fields half a cell different in the x-direction shown in gray. Solid circles represent the electric fields and hollow circles represent the magnetic fields. The temporal variation between the electric and magnetic fields has been suppressed in these figures. In the single surface implementations, the desired surface, S, is represented by the solid horizontal black line. Arithmetic or geometric averaging would be used to find the fields $E_z(m, n, p)$, $H_y(m + 1/2, n, p)$ and $H_x(m, n + 1/2, p)$ such that they are on the surface S. These fields are not shown in the figure, but they are found by averaging in the z-direction. The mixed surface method represented in Fig. 2.2 is similar to Fig. 2.1 only the exterior surface is not necessary in this case. Two surfaces, S_{TE} and S_{TM}, are defined to hold the electromagnetic fields where S_{TM} contains the transverse magnetic fields, while S_{TE} contains the transverse electric fields. In this context, transverse is referred to relative to the normal. In NTFF transformations the normal components are not necessary (i.e. there are no E_z and H_z components for the $\hat{n} = -\hat{z}$ face currently being considered) so one surface only contains electric fields and the other surface only contains magnetic fields. As was performed by Martin, each of these fields is weighted by Green's functions as though they are obtained from the opposite surface (i.e. even though the E_z component is obtained from the S_{TE} surface, the Green's function weights the field as though it is

obtained from the S_{TM} surface).

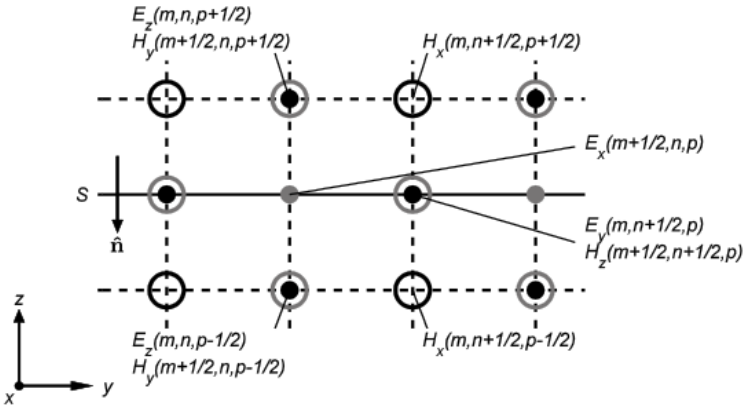

Figure 2.1: Electromagnetic fields necessary for computing NTNF transforms on the $\hat{n} = -\hat{z}$ face using interpolation based methods such as arithmetic and geometric means.

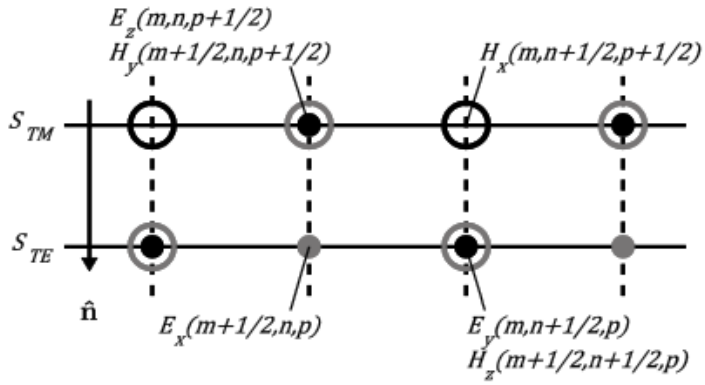

Figure 2.2: Electromagnetic fields necessary for computing NTNF transforms on the $\hat{n} = -\hat{z}$ face using the mixed surface method.

One could be tempted to leave the normal electromagnetic components in the same position as they are calculated such that all electric fields are on one surface and all

magnetic fields are on another. However, it is better to treat the transverse electric and transverse magnetic fields separately and then use the principle of superposition to determine the arbitrary polarization. This idea is used in many other electromagnetic field applications [49]. The mixed surface implementation of the Stratton-Chu integrals is presented in Eqs. 2.5 and 2.6 where the r_P vector has been suppressed in the Green's functions for space considerations.

$$\begin{aligned}\mathbf{E}_{\mathrm{FDTD}}(\mathbf{r}_P) &= -\oiint_{S_{TE}} [j\omega\mu(\hat{\mathbf{n}} \times \mathbf{H}|_{S_{TM}})G(\mathbf{r}_{S_{TE}})]\, dS' \\ &\quad -\oiint_{S_{TM}} [(\hat{\mathbf{n}} \times \mathbf{E}|_{S_{TE}})\nabla G(\mathbf{r}_{S_{TM}}) + \\ &\quad +(\hat{\mathbf{n}} \cdot \mathbf{H}|_{S_{TE}})\nabla G(\mathbf{r}_{S_{TM}})]\, dS' \end{aligned} \tag{2.5}$$

$$\begin{aligned}\mathbf{H}_{\mathrm{FDTD}}(\mathbf{r}_P) &= -\oiint_{S_{TM}} [j\omega\mu(\hat{\mathbf{n}} \times \mathbf{E}|_{S_{TE}})G(\mathbf{r}_{S_{TM}})]\, dS' \\ &\quad +\oiint_{S_{TE}} [(\hat{\mathbf{n}} \times \mathbf{H}|_{S_{TM}})\nabla G(\mathbf{r}_{S_{TE}}) + \\ &\quad +(\hat{\mathbf{n}} \cdot \mathbf{E}|_{S_{TM}})\nabla G(\mathbf{r}_{S_{TE}})]\, dS' \end{aligned} \tag{2.6}$$

The double integral in Eqs. 2.5 and 2.6 is split into two parts since integration is performed over two different surfaces. In practice, each term is integrated by double summation over each of the six faces of an FDTD box and subsequently summed together. The spatial variations of the electromagnetic fields require different limits of integration for each field on each face. The Total Field Scatter Field (TFSF) limits of integration (or indices) presented by Taflove are used for the tangential components

[115]. The normal electric fields are integrated over the entire range of indices, from the first-to-last. On the other hand, the magnetic fields are integrated from the second to the second-to-last index in each direction, such that no component is outside the surface.

Martin published a subsequent paper displaying the effectiveness of the mixed surface in the time domain [73]. Similar vector analogs could be used for a time domain version of NTNF equations. The time domain equations are similar to the frequency domain corollaries except, instead of using Green's functions, the electromagnetic fields are weighted by retarded times that are based on the position on the artificial surface relative to the desired observation point. The same process of altering calculated versus perceived position would be performed for the time domain.

2.3 Results

2.3.1 Strongly Forward Scattering Sphere

In order to compare the mixed surface implementation of the vectorial Stratton-Chu diffraction integrals with the arithmetic and geometric mean implementations, light scattering is simulated in free space from a strongly forward scattering sphere. This type of sphere has been used as the gold standard to look at the accuracy of far field backscattered light from strongly forward scattering objects in several far-field papers [65, 72, 99, 115]. Not only does the sphere allow for direct comparison with the analytical Mie series solution, providing an easy method to determine the accuracy of the transformation, but it also provides an extreme case to look at the effect of phase errors in the backscatter direction. While previous examples used the far field Mie

series formulation, this simulation requires the more complicated and less familiar near field method [107]. The Mie series solution provides an analytical solution to Maxwell's equations for scattering of an incident plane wave by a sphere. For the purposes of this work, accuracy is defined as the error between the simulated results and the analytical calculations provided by the Mie Series.

Near field scattering of a plane wave by the sphere is accomplished using FDTD where plane waves are introduced using the TFSF formulation [115]. The NTNF boundary is located in the scatter field portion of the grid. A two-dimensional cross section of the simulation setup is illustrated in Fig. 2.3 where the object is shown as an arbitrary ellipse. The TFSF boundary is implemented using a one-dimensional auxiliary grid to eliminate the effect of numerical dispersion on the calculations. Numerical dispersion is an inherent effect in FDTD where waves travel at slower than desired velocities due to the number of cells per wavelength with which they are discretized and the angle that they travel with respect to the grid axes [115]. Z-polarized plane waves traveling in the x-direction are modeled as a Gaussian modulated sine-wave of the form:

$$E^i = \exp\left(-((t - t_)/\tau)^2/2\right) \sin(2\pi f_0(t - t_0)) \tag{2.7}$$

where $\tau = 2$fs, $f_0 = 4.283 \times 10^{14}$ Hz, and $t_0 = 9\tau$. The TFSF boundary is held at five cells away from the edge of the sphere for each of the simulations. It should be noted that the simulation defines the origin at the center of the grid in contrast to conventional methods where waves are introduced from a corner (or a side). For this reason, other implementations would utilize smaller t_0 values to make sure the entire plane wave travels through the grid before the maximum time step. The sphere is

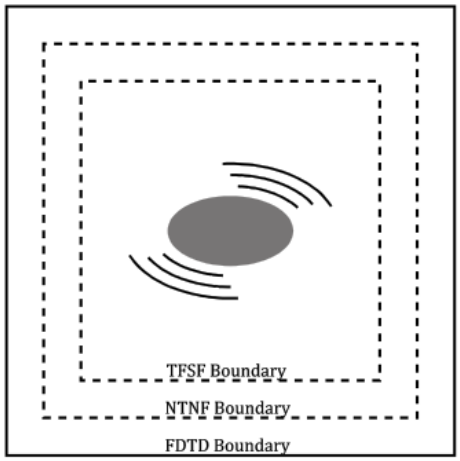

Figure 2.3: Two-dimensional cross section of basic simulation setup where a microsphere is radiating electromagnetic waves inside the FDTD computational grid. The TFSF and NTNF boundaries are imaginary cubes inside the FDTD grid.

simulated as a dielectric with a relative permittivity of 1.21 and a radius of 1.5 μm. Grid spacing is set at 25 nm ($\Delta x = \Delta y = \Delta z$), producing 60 cells along the radius of the sphere executed using the staircasing method. Staircasing is a standard technique in FDTD where curved boundaries are represented as a series of block like steps. The simulation is run at 95% of the 3D Courant limit ($0.95/\sqrt{3}$) for 2048 time steps. The grid is $190 \times 190 \times 190$ cells and terminated using an eleven cell Convolutional Perfectly Matched Layer (CPML) [100, 115]. The FDTD algorithm is implemented in parallel utilizing Message Passage Interface (MPI) to transfer magnetic fields between the sub cubes in the 3D topology. The DFT necessary for the NTNF calculations is run concurrently with the FDTD simulation.

The Stratton-Chu integrals are used to calculate the electromagnetic fields for 1002.94 nm wavelength light with the three methods (arithmetic average, geometric

average, and mixed surface method) at only 5λ away from the origin or approximately one wavelength away from the edge of the sphere. To compare the effect of phase errors on the different implementations, the number of cells are varied between the edge of the sphere and the NTNF box ($D = 10$, 15, and 20) and the normalized cross section is calculated as defined in Eq. 2.8. The normalized cross section is borrowed from far field calculations after eliminating the limit as the observation point goes to infinity. The E_r and E_φ components are ignored recognizing that the greatest variation in the magnitude of this component offered the best opportunity to assess the accuracy of the different implementations.

$$\sigma_{NTNF} = \frac{4\pi r^2}{\lambda^2} \frac{|\hat{E}_\theta(\theta, \phi)|^2}{|\hat{E}^i_\theta|^2} \tag{2.8}$$

Only the results for the arithmetic mean and the mixed surface method are shown in Fig. 2.4 and Fig. 2.5, as there is very little visual difference between the geometric mean and the mixed surface method in this representation. Generally the transformations look accurate for all angles for all three implementations except from 140° to 180° for the arithmetic average where variations due to phase errors are noticeable.

To better illustrate the difference between the three methods the relative error between each implementation and the Mie series is plotted where the relative error is defined as:

$$\eta = \frac{|\sigma_{Mie} - \sigma_{NTNF}|}{|\sigma_{Mie}|} \tag{2.9}$$

The results are shown in Fig. 2.6, Fig. 2.7, and Fig. 2.8. The effect of phase errors on these calculations is much more apparent in the arithmetic and geometric transfor-

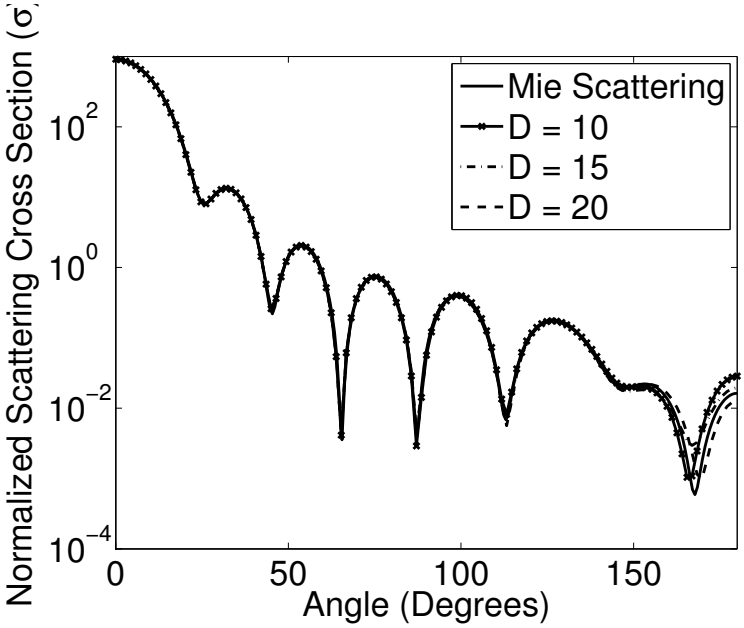

Figure 2.4: Normalized scattering cross section calculated using the arithmetic mean along a 4λ arc away from the origin. The scattering is calculated for a 1000 nm wavelength plane wave interacting with a forward scattering microsphere.

mations where the calculations vary significantly based on where the NTNF surface is located relative to the TFSF surface. This is seen as the plots in Fig. 2.6 and Fig. 2.7 do not align very well as D is varied. On the other hand, phase errors had almost no effect on the mixed surface method as the calculations in Fig. 2.8 generally lie on top of each other regardless of the position of the NTNF surface. In the backscatter direction, the relative error of the arithmetic mean calculations goes from 0.7489 ($D = 10$) to 0.2004 ($D = 15$) to 0.2180 ($D = 20$), which is illustrated in Fig. 2.6 by the wide variation at 180°. The geometric mean provides better results, as the wide variation is not apparent in the relative error backscatter ranges from 0.1984 to 0.2037 for the three simulations. The mixed surface implementation performs the best as the result for all three simulations hover right around 0.160.

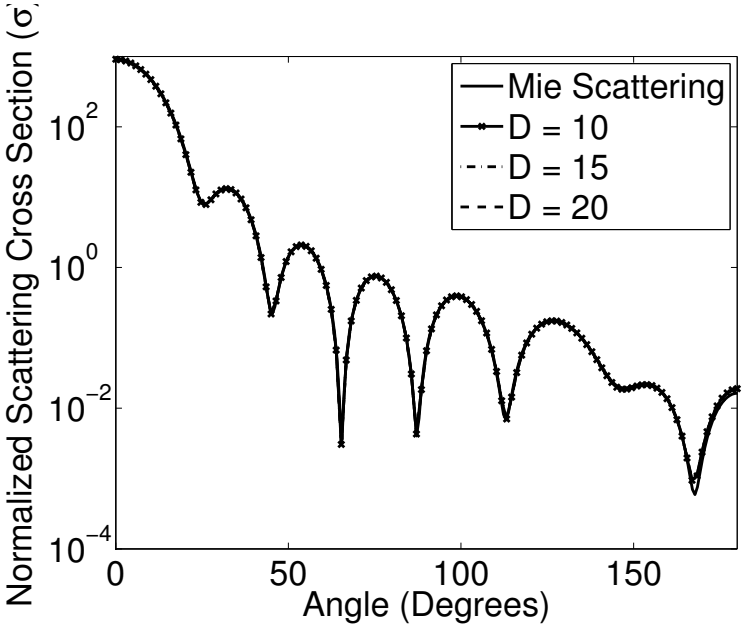

Figure 2.5: Normalized scattering cross section calculated using the mixed surface along a 4λ arc away from the origin. The scattering is calculated for a 1000 nm wavelength plane wave interacting with a forward scattering microsphere.

For some angles (such as 30°), the arithmetic and geometric averages produce more accurate calculations than the mixed surface method, but in general the mixed surface method produces more accurate results for the majority of angles. In fact for $D = 10$, the mixed surface implementation provides the more accurate result for approximately 70% of the angles. The majority of the angles for which the arithmetic and geometric mean are better than mixed surface are in the forward scattering direction. For example, the arithmetic mean provides a more accurate result compared to the mixed surface for angles ranging from 0° to 43° . However, this analysis ignores the fact that the relative error for these particular angles is often an order of magnitude smaller than that of the backscatter direction.

For many angles, the $D = 20$ simulation produced the most accurate result es-

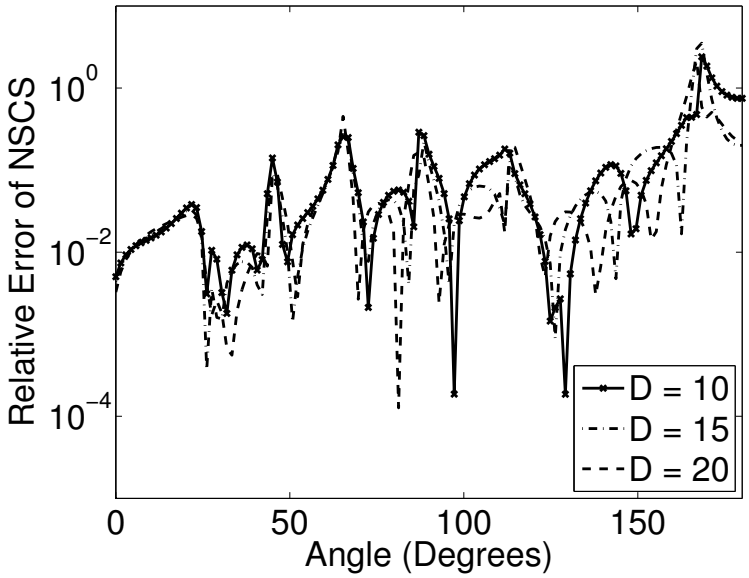

Figure 2.6: Relative error of the normalized scattering cross section calculated using the arithmetic mean on an arc 4λ away from the origin.

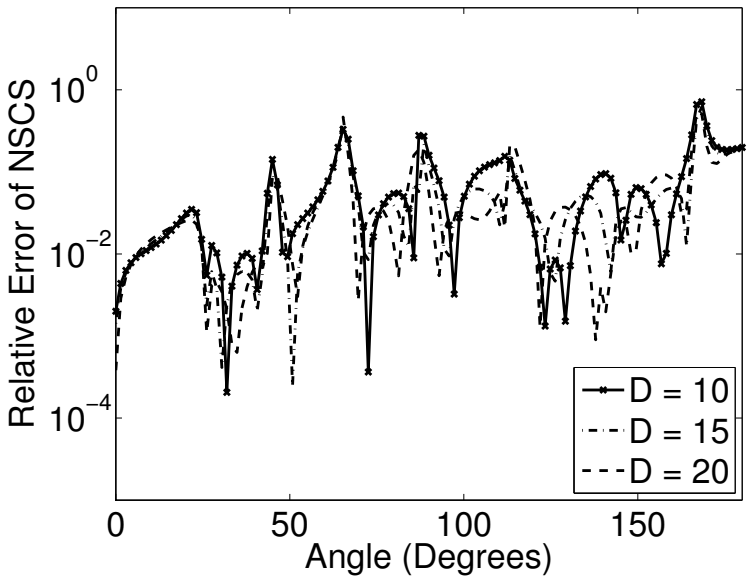

Figure 2.7: Relative error of the normalized scattering cross section calculated using the geometric mean on an arc 4λ away from the origin.

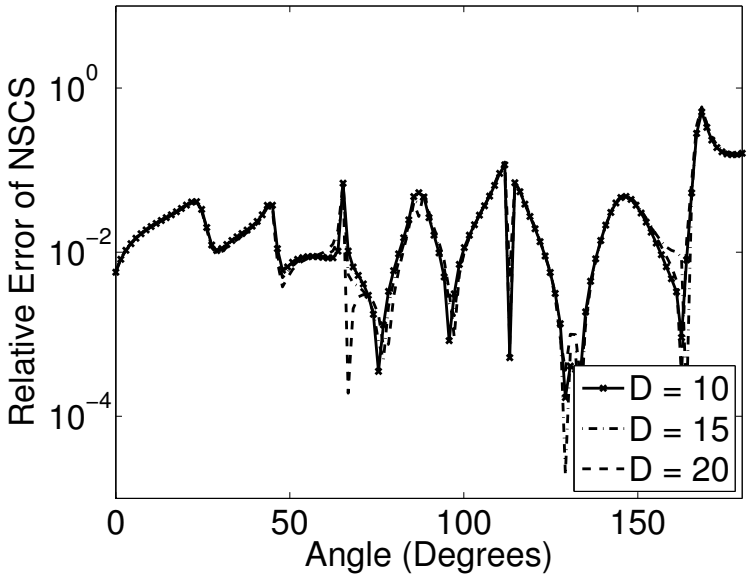

Figure 2.8: Relative error of the normalized scattering cross section calculated using the mixed surface on an arc 4λ away from the origin.

pecially for the arithmetic mean where the radiation has had a greater chance to stabilize as it travels through the grid thus phase errors have a smaller effect on the calculations. However, the larger D value requires a larger computational grid, which increases the overall computational cost of both the FDTD simulation and the NTNF calculations. Thus the best implementation could be characterized as the most accurate transformation with the smallest possible grid. By combining the analysis of the relative error with the accuracy results where $D = 10$, it is safe to say the best transformation is the mixed surface implementation.

Additionally the accuracy of the different implementations is probed for backscattered light over 500-1000 nm incidence at $z = -2.5\mu m$. These wavelengths correspond to twenty to forty cells per wavelength in the FDTD grid, which should have a noticeable effect on the accuracy of the transforms. The same parameters are used for

this simulation, only the number of time steps is doubled to 4096 to increase the number of wavelengths that could be calculated, which is inherently limited by the DFT. Fig. 2.9 shows the results. The geometric mean and the mixed surface methods accurately follow Mie theory for all wavelengths each producing a Pearson correlation coefficient above 99%. The arithmetic mean seems to improve as the number of cells per wavelength is increased; however, it never reaches the accuracy of the other two methods. Over the total range the correlation coefficient for the arithmetic mean is 74.2%.

It should be noted that the one-dimensional (1D) auxiliary grid is essential for these backscatter calculations, as numerical dispersion became a major source of error for small cell per wavelength ratios. For backscatter from incident light not aligned with one of the Cartesian axes it is postulated that an advanced dispersion compensation approach, such as the Analytical Field Propagation TFSF method [103], is required to maintain accuracy.

2.3.2 Diffraction by Three Spheres

Next the mixed surface implementation is applied to a practical problem that does not have an analytical solution. In this example the diffraction pattern of three spheres is calculated for both x- and y-polarized light traveling in the z-direction. This particular simulation provides an example of scattering from an ensemble of flow cytometry calibration standards whose near field electromagnetic scattering could be used to simulate images produced by a high NA microscope. Flow cytometry calibration standards are utilized rather than a theoretical cell because they provide

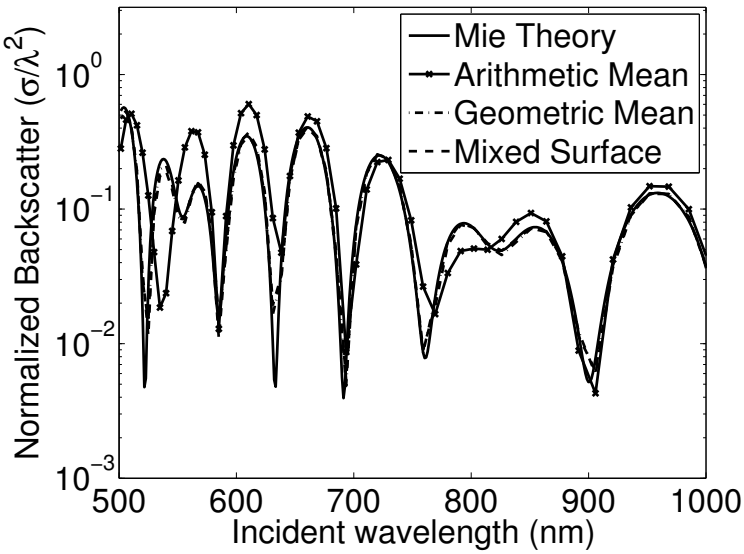

Figure 2.9: Normalized backscatter cross section calculated at 4λ behind the origin using 500-1000 nm wavelength light.

a more distinguishable diffraction pattern. This approach shows the power of the Stratton-Chu integrals and their ability to calculate near field scattering outside the artificial surface.

The spheres are designed to mimic 1 μm diameter flow cytometry calibration standards similar to Invitrogen's (Life Technologies, Carlsbad, California) F-13838 line whose refractive index is 1.591. The spheres are placed in media with a refractive index of 1.45 similar to Nye's OC431A-LVP Optical Gel (Nye Synthetic Lubricants, Fairhaven, MA). Optical gel is utilized in some microscopy applications to hold objects of interest in place [35]. In practice the refractive indices of both materials vary with wavelength. For example, the refractive index of the optical gel changes 0.02 over 500-700nm. Since these variations are small, they are ignored for this simulation. Three spheres are placed in the orientation described by Fig. 2.10 where all three

spheres are placed on the plane. This particular orientation was previously utilized with perfectly electric conducting (PEC) spheres in free space [120]; however, the refractive indices used in this example are chosen to better mimic a practical problem that could be seen in life sciences microscopy. The PEC example was performed as a stepwise check and the results are the same as those achieved by Török *et al.*, but they are not included due to space considerations. The spheres are discretized using 40 cells along the diameter and subjected to 1017.98 nm incident light. Again the spheres are implemented using the staircasing method. Careful consideration is required to make sure the spheres are correctly oriented in the grid such that they do not overlap. The backscatter diffraction pattern is computed on the plane $z = -2\lambda$, which is directly applicable to high NA reflection microscopy. The backscatter direction was previously shown to have the most potential errors and is where the mixed surface implementation of the Stratton-Chu integrals is really able to outperform the interpolation methods. For this reason, the interpolation results are not shown.

The intensity of the scattered electromagnetic radiation as a result of x-polarized incident light is shown in Fig. 2.11, while Fig. 2.12 shows the results of y-polarized light. Each figure is individually normalized. The intensity is defined as:

$$I = |\mathbf{E}|^2 \tag{2.10}$$

As shown in Fig. 2.11 and Fig. 2.12, there is an obvious difference between the diffraction patterns produced by the x-and y-polarized light. Also, there are very slight variations in the symmetry of side lobes from the left and right sides of each image.

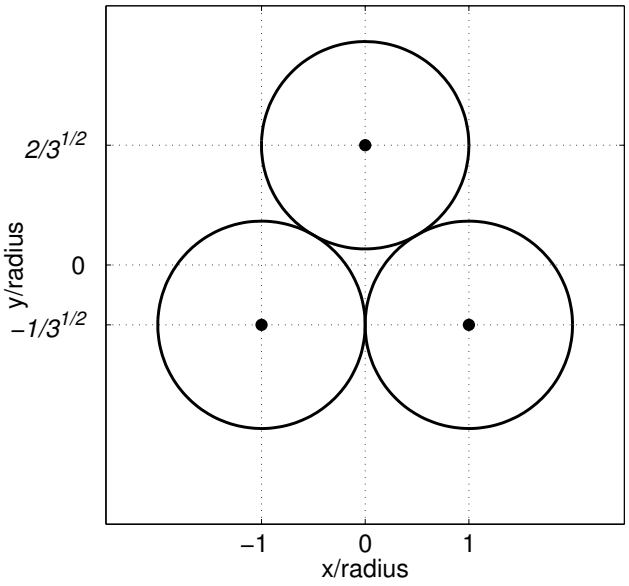

Figure 2.10: Orientation of three spheres used for the two diffraction simulations where the spheres are shown in the plane $z = 0$. Adapted from [120].

This is explained by the way the spheres are discretized and the orientation described in Fig. 2.10, where the center of the spheres are not directly in line with the grid indices. Pearson's correlation coefficient is used to determine the variations between the corresponding left and right sides of each image and in both cases it is above 99.8%. If the spheres are discretized such that there are 80 cells along the diameter then the symmetry would have been even more negligible. Forty cells per wavelength already represents the higher end of the standard number of cells per wavelength. Understandably near field calculations are more susceptible to variations in the way objects are discretely represented as compared to far field calculations. Despite these small fluctuations, the results of the previous example suggest these results embody the best method for calculating near field electromagnetic fields.

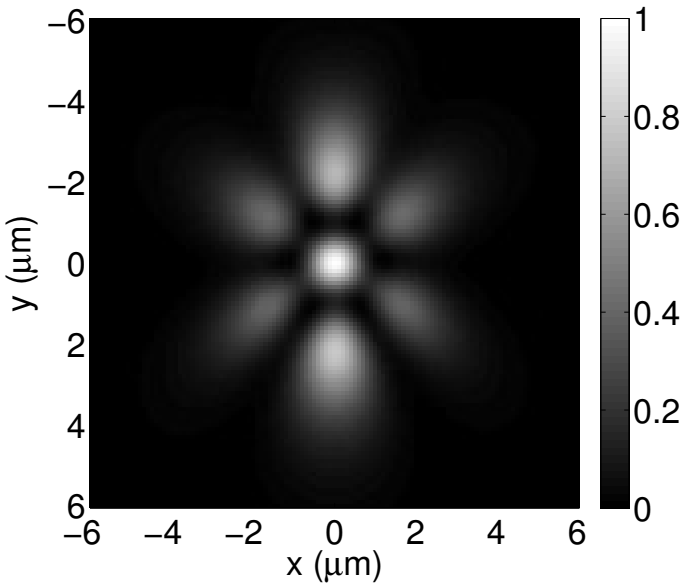

Figure 2.11: Normalized intensity of scattered field in the plane $z = -2\lambda$ for x-polarized light incident on the three diffraction spheres.

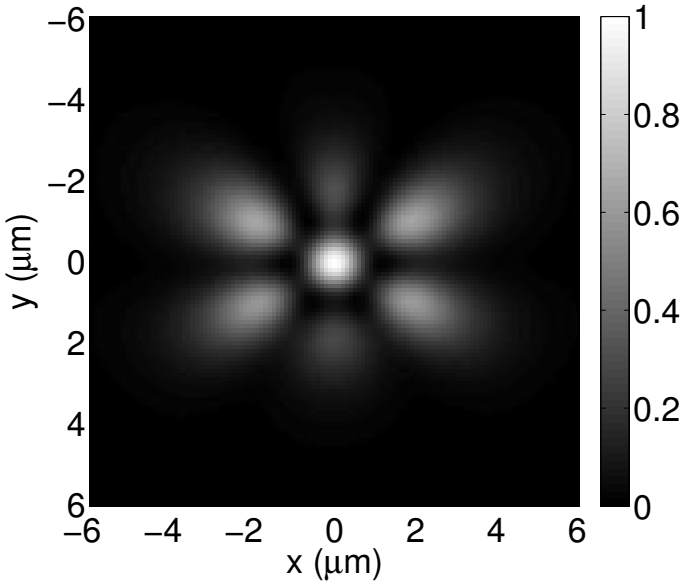

Figure 2.12: Normalized intensity of scattered field in the plane $z = -2\lambda$ for y-polarized light incident on the three diffraction spheres.

2.4 Conclusion

In this chapter, the mixed surface implementation described by Martin is expanded from the NTFF transformation to the NTNF transformation. The power of the implementation is shown over the previous methods using the strongly forward scattering sphere as the gold standard where an analytical solution exists. Additionally the algorithm is applied to an ensemble of flow cytometry calibration standards where an analytical solution does not exist. The results show the mixed surface implementation of the Stratton-Chu vectorial diffraction integrals provides improved near field calculations compared with interpolation-based methods. These electromagnetic fields are readily applied to high NA microscopy simulations, especially in the backscatter direction.

Chapter 3

SIMULATING 3D OPTM IMAGES

3.1 Background

This chapter outlines a computational model of the Cell-CT where improved interpretation of light scattering, image reconstruction, and image analysis techniques will eventually lead to quantitative measurements. The simulation will be used to evaluate the effects of diffraction, refraction, and absorption on the reconstruction of 3D images of standards, such as nano and micro-particles. It will also provide a framework to quantify system errors and inconsistencies, including nonlinear scanning of the objective, hysteresis in focal-plane scanning and cell motion. This is the first computational model of a high NA optical microscope for the field of optical projection tomography.

A computational model of light propagation through a cell within the microcapillary is derived to improve imaging parameters in OPTM. Computational modeling of the imaging process associated with OPTM is complicated by the use of high NA condensers and objectives, which preclude the use of most theoretical simplifications. For example, Fourier optics techniques, such as Fresnel and Fraunhoffer diffraction, are only valid for paraxial applications [86]; furthermore, such models ignore the effect of refraction, multiple scattering [122], and polarization. The most accurate method of modeling microscopes requires directly solving Maxwell's curl equations. While an-

alytical solutions are preferred, solutions are only available for spheres and cylinders using Mie theory [40, 107], which cannot be extended to arbitrary objects, such as a cell.

A variety of methods are available to numerically solve Maxwell's equations, including finite-difference time-domain (FDTD), method of moments (MOM), and finite element modeling (FEM). Each of these methods is computationally limited, in that it is impossible to propagate light waves all the way from the condenser to an image detector due to the distance per number of wavelengths [120]. To compensate, several groups have designed computational models that break image formation into multiple steps whereby different techniques can be used over the course of propagation to reduce the computational load. Generally, these steps cover four main aspects: illumination [15], near-field scattering [115], resampling [22], and image formation [85]. This four-step process allows near-field scattering to be computed using a computationally intensive numerical method from which the final image is computed. This model supplements the original illumination technique with one that provides a more straight forward method of performing transmission imaging [15].

This model is also differentiated by a number of programmatic elements that provide greater computational expediency and accuracy. These include pre-computing coefficients necessary for calculating near-field scattering for improved computational cost and reduced numerical dispersion [103]. Additionally, the resampling technique used for this work has produced more accurate results compared to previous methods [22]. The 2D model is also extended to produce simulated 3D images similar to the Cell-CT using micro-shells and idealized conditions for improved computational

efficiency.

3.2 Theory

The theory of OPTM image formation and its implementation are provided below where the cell can be of arbitrary size, shape, and material properties and it can sit in media with any refractive index. Since the micro-capillary and slide/coverslip provide near refraction free imaging they are ignored for this analysis [35]. Future research could be performed to include their minor effects in the model. A general diagram of the modeling components used in image formation is illustrated in Fig. 3.1. The illumination is introduced into a numerical method to compute the near-field scattering (scattering is used broadly to encompass the effects of refraction, reflection, and absorption) around the object, which is then resampled to determine the scattering that would be seen on an infinite plane in the direction of the condenser. The scattering calculated on this plane is mapped to the final image. Since each of these four steps is well described elsewhere [15, 121], they are only summarized here where two of the steps are implemented in an alternative way to produce a more accurate and computationally effective algorithm. Each part is linked together in Section 3.2.5 to fully understand the entire process required to simulate a projection. The projections are finally reconstructed to form a 3D representation of a micro-shell, which could represent an isolated nuclear membrane from a cell.

3.2.1 Illumination

Illumination in a high NA bright-field microscope is normally partially coherent Köhler illumination where point sources on the back focal plane of the objective

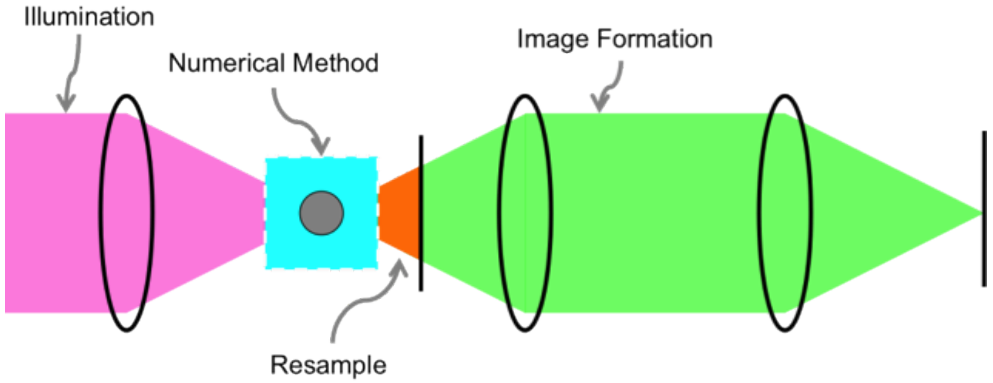

Figure 3.1: Diagram of the image formation model for a high NA bright-field, transmission microscope. The model consists of four main parts: illumination, numerical method, resampling, and image formation.

result in plane waves near the focal plane in the image space. In order to simulate partial coherence, scattering due to a large number of orthogonal sets of plane waves is computed using separate simulations for each plane wave and the intensity from each simulation is summed to produce a final image [16]. While this method would produce the best possible results, the computational cost of this technique is quite high and becomes impractical when the objective focal plane is scanned as is performed in OPTM. Instead, the model assumes a coherent, polarized focused pulse, which is scanned throughout the object space and the intensity resulting from the scattered light at each scan position is integrated to form a final image. This assumption reduces the computational cost of one simulation, described below, by over eight times to approximately twenty-four hours using an eight-core workstation. Beyond the computational cost considerations, modeling using coherent illumination is supported experimentally by the use of an incidence filter designed to emphasize absorption of Hematoxylin bound to DNA. The illumination filter is a 60 nm bandpass

filter centered at 588 nm, which boosts the coherence length to approximately five times that of standard white light, or 1.75 μm. While some of the objects that will be simulated are a little larger than 1.75 μm, the use of a coherent pulse will provide results with accuracy high enough for this application such that coherent waves will approximate partial coherence for the illumination bandpass.

Illumination is mathematically derived in the time-domain using coherent, polarized light, which is focused through a thin aplanatic converging lens [15]. Light rays polarized in the x-direction travel parallel to the optical axis interacting with the lens before being diffracted by the exit pupil. The direction of each ray after interacting with the lens is determined by geometric optics. The rays describe the direction and polarization of the plane waves propagating proximal to the focus. The resulting electric field around the focal plane is a superposition of plane waves:

$$E(r,t) = \frac{f}{2\pi c}\iint_S \frac{\hat{e}^w(\theta',\varphi')}{s'_z}\dot{E}(t')\cos^{1/2}(\theta')\,ds'_x\,ds'_y \tag{3.1}$$

integrated over the domain $S = \{(s_x, s_y)\in\mathbb{R}^2 \mid s_x^2+s_y^2 \leq n\sin\theta_{max}\}$ where f is the focal length of the condenser and c is the speed of light. The Cartesian coordinate variables of integration s'_x, s'_y, and s'_z are directly matched with their spherical coordinate counterparts where $\hat{\theta}' = \cos^{-1}(s'_z)$ and $\hat{\varphi}' = \text{atan2}(s'_y, s'_x)$. The maximum θ' is θ_{max}, which is the maximum angle of intersection with the optical axis as defined by the numerical aperture (NA$= n\sin(\theta_{max})$). The unit vector $\hat{e}^w(\theta',\varphi\prime)$ is the polarization vector found using geometric optics that is directly related with the position vector of the ray interacting with condenser lens. The polarization angle is defined as the angle

the electric vector makes with the meridonal plane. The $\cos^{1/2}(\theta')$ factor is a result of the intensity law of geometric optics, dampening the intensity of waves coming from the edge of the lens as compared to those propagating a shorter distance from the center of the lens [97]. The dot above the incident electric field indicates the time derivative and the incident electric field, $E(t')$, is a function used to describe the time variations in the electric field along the propagating plane wave. The plane waves can be introduced with any desired wavelength range using a Gaussian modulated sine wave.

The focused pulse represented by Eq. 3.1 can be approximated discretely using numerical integration methods. While a two-dimensional integration would be preferred, it is often difficult to implement these techniques. Instead, this work follows the previously defined one-dimensional technique, in which integration is performed using extended midpoint. Çapoglu *et al.* uses spherical variables of integration to discretize the aperture [15], leading to a large number of plane waves propagating from the center of the aperture and an inadequate number of plane waves propagating from the outer circle of the aperture sampling. The only way to sample the outer dimensions of the aperture with enough rays in this scheme is to significantly oversampling the inner portion of the aperture. Instead, an alternative procedure is performed where a Cartesian grid is placed on top of the circular aperture and the incident rays are introduced at equally spaced Cartesian intervals throughout the entire aperture. This procedure significantly reduces the oversampling performed using spherical decomposition.

The number of rays representing the focused pulse in the Cartesian grid is dictated

by the sampling theorem such that there is no statistical correlation between two adjacent points on the sample plane. The so-called "mutual coherence function" [7] quantifies this correlation and provides a means to determine the appropriate anti-aliasing criteria. A closed form solution provided in [14] is replicated here for completeness:

$$\Delta s_x \leq \frac{2\pi f}{k \max\{D, W_c\}}, \ \Delta s_y \leq \frac{2\pi f}{k \max\{D, W_c\}} \tag{3.2}$$

where D is the sample dimension, W_c is the value at which the mutual coherence function falls below a negligible value ($W_c = 1/(k \sin(\theta_{max})) = 1/(k_0 \mathrm{NA}_{illum})$), and the smallest wavelength in the excitation dictates the wavenumber for the anti-aliasing condition.

3.2.2 Numerical Method

The illumination is employed in the FDTD method as it provides a simple and elegant framework to solve Maxwell's curl equations in the time domain. FDTD allows an entire broadband pulse to be simulated in a single run. A brief overview of FDTD is described below while the reader is referred to Taflove and Hagness for a more detailed presentation of the technique [115]. Maxwell's curl equations are often written:

$$-\mu \frac{\partial \mathbf{H}}{\partial t} = \nabla \times \mathbf{E} \tag{3.3}$$

$$\sigma \mathbf{E} + \varepsilon \frac{\partial \mathbf{E}}{\partial t} = \nabla \times \mathbf{H} \tag{3.4}$$

where ε is permittivity, μ is the permeability, σ is the conductivity, $\mathbf{E}$ is the electric field vector, and $\mathbf{H}$ is the magnetic field vector. These equations show that the

magnetic fields vary temporally with the spatial variations in the electric fields and vice versa. In this scheme it is important to understand that the relative permittivity and permeability are directly linked to the complex refractive index ($\tilde{n} = \sqrt{\mu_r \hat{\varepsilon_r}}$), where the real portion represents pure refraction and the complex portion represents absorption. At optical frequencies, the relative permeability is very close to one, so the complex refractive index is simplified to $\hat{n} = \sqrt{\hat{\varepsilon_r}}$. The complex refractive index can also be written to explicitly show the absorption, or extinction coefficient (κ), in $\tilde{n} = n + i\kappa$.

Discretization of the electric field is performed using the Yee Cube in which the electric and magnetic fields are spatially and temporally located at half step differences [130]. These spatial and temporal differences allow the electromagnetic fields to be approximated using finite differences. As an example, the E_z field is discretized using finite differences:

$$\begin{aligned} E_z^{q+1}\left[m,n,p+\frac{1}{2}\right] &= \frac{1-\frac{\sigma\Delta_t}{2\varepsilon}}{1+\frac{\sigma\Delta_t}{2\varepsilon}} E_z^q\left[m,n,p+\frac{1}{2}\right] + \\ &\frac{1}{1+\frac{\sigma\Delta_t}{2\varepsilon}}\left(\frac{\Delta_t}{\varepsilon\Delta_x}\left\{H_y^{q+\frac{1}{2}}\left[m+\frac{1}{2},n,p+\frac{1}{2}\right]\right.\right. \\ &\left. -H_y^{q+\frac{1}{2}}\left[m-\frac{1}{2},n,p+\frac{1}{2}\right]\right\} \\ &-\frac{\Delta_t}{\varepsilon\Delta_y}\left\{H_x^{q+\frac{1}{2}}\left[m,n+\frac{1}{2},p+\frac{1}{2}\right]\right. \\ &\left.\left. -H_x^{q+\frac{1}{2}}\left[m,n-\frac{1}{2},p+\frac{1}{2}\right]\right\}\right) \end{aligned} \tag{3.5}$$

where Δt is the change in time per time step, Δx, Δy, and Δz are the spatial increments, and m, n, and p are the spatial indices. There are five similar equations to

describe the other two electric field components and all three magnetic field components.

The spatial and temporal time increments are tightly linked together by the Courant Number, which is required to maintain numerical accuracy in explicit time-marching schemes used to solve partial differential equations. It is generally accepted that 20 points per wavelength are required to maintain accuracy where the error of finite differences is $O(\Delta^2)$ [115]. Since discretization of light waves at such a high resolution is computationally costly, the computational grid should contain as few grid points as possible. For this reason, light traveling in an infinite space is modeled using absorbing boundary conditions [115]. This work relies on the Convolution Perfectly Matched Layer (CPML) (a variation of Berenger's PML [5]), which absorbs waves at the boundary of the grid with much greater accuracy compared to previous boundary conditions [100].

Electromagnetic waves are introduced into the FDTD grid as either point sources or plane waves. Plane waves are more applicable to this work due to the plane wave decomposition of the illumination described previously [15]. Plane waves could be introduced using the pure scatter field formulation, which reduces the amount of energy in the grid thereby reducing potential errors, but at a high computational cost. Alternatively, they can be introduced with arbitrary direction and polarization using the total-field scatter-field (TFSF) formulation [77]. Using this method the grid is separated into two regions: the total field and the scatter field. The total field is in the inner portion of the grid enclosing the cell and includes both the incident and scatter fields. The scatter region, on the other hand, only contains the scattered

electromagnetic radiation. The two regions are separated by altering the fields at the total-field/scatter-field boundary based on the time step, wave direction, and polarization. The cell interacts with the illumination in the total field and the waves that are scattered propagate to the scatter field and are mapped to the final image.

3.2.3 Resampling

The scattered fields collected in FDTD are resampled in preparation for the final image formation component, which requires an infinite plane that is not capable of being acquired directly from the finite FDTD lattice. Additionally, the high NA microscope theory requires the plane to be close to the focal plane. Together, these two requirements necessitate the use of a NTNF transformation [121]. Here the NTNF is briefly described but the reader should refer to Chapter 2 for a more in-depth discussion. In this work, the NTNF transformation uses the Stratton-Chu vectorial diffraction integrals defined as:

$$\begin{aligned}\mathbf{E}(r_P) &= -\oiint_S [j\omega\mu\,(\hat{n}\times\mathbf{H})\,G(r_S,r_P) - (\hat{n}\times\mathbf{E})\times\nabla G(r_S,r_P) \\ &\quad -(\hat{n}\cdot\mathbf{H})\,\nabla G(r_S,r_P)]\,dS' \end{aligned} \tag{3.6}$$

$$\begin{aligned}\mathbf{H}(r_P) &= \oiint_S [j\omega\mu\,(\hat{n}\times\mathbf{E})\,G(r_S,r_P) + (\hat{n}\times\mathbf{H})\times\nabla G(r_S,r_P) \\ &\quad +(\hat{n}\cdot\mathbf{E})\,\nabla G(r_S,r_P)]\,dS' \end{aligned} \tag{3.7}$$

where $\hat{n}$ is the outward surface normal, $G(r_s, r_P)$ is the free-space Green's function:

$$G(r_s, r_P) = \frac{\exp\left(-jl\left|r_s - r_p\right|\right)}{4\pi\left|r_s - r_p\right|} \tag{3.8}$$

$$\left|r_s - r_p\right| = \sqrt{(x - x_p)^2 + (y - y_p)^2 + (z - z_p)^2} \tag{3.9}$$

with $r_P = (x_p, y_p, z_p)$ being the observation point and $r_S = (x, y, z)$ being the coordinates of the fields on the surface of integration S. The spatial offsets among the electromagnetic fields makes it impossible to obtain a single surface of integration directly from FDTD. Traditionally, a single surface is obtained by interpolating fields using the arithmetic mean. However, the accuracy of the arithmetic mean is strongly hindered by phase errors [71, 99]. Though the geometric mean produces better results [99], the alternative mixed surface method presented in Chapter 2 was implemented to dramatically reduce phase errors associated with the other two methods [22].

Borrowing ideas from the Huygens's sources, the mixed surface technique acquires electric fields from their regular positions, but assumes they come from the magnetic field's position during the weighting process. The opposite is also true where the magnetic fields are acquired from their regular position but assumed to be located on the electric field surface. This idea of switching calculated and perceived locations reduces the computational and storage costs required for two separate magnetic fields [71, 72]. The mixed surface Stratton-Chu diffraction integrals are implemented in FDTD as a box or rectangle and calculated for each desired frequency. The resulting electromagnetic fields on the infinite plane are transformed through the objective to the detector space for each frequency.

3.2.4 Image formation

Image formation is treated as a coherent superposition of equivalent magnetic dipoles using the Debye-Wolf integral [121]. The image from each point is computed separately and subsequently summed to determine the overall electric field at the detector. The m-theory of diffraction determines the contribution from each equivalent magnetic dipole across the infinite plane to find the electromagnetic field at any observation point on the infinite half plane extending to $z = \infty$. The electric field at point $P = (x_P, y_P, z_P)$ is a result of the superposition of spherical waves from points $Q = (x_Q, y_Q, z_Q)$ situated on surface S_o [121]:

$$\mathbf{E}_{img}(P) = \frac{-jk}{2\pi} \iint\limits_{S_o} (r \times (n \times \mathbf{E}(Q))) \frac{\exp(-jkr)}{r^2} dS \tag{3.10}$$

where $r = (x_P - x_Q, y_P - y_Q, z_P - z_Q)$ is a vector pointing from Q to P. This theory fits directly with the Debye-Wolf diffraction integral to determine the resulting image at the detector as a result of propagating through the objective. The effect of the objective is incorporated through expansion of generalized Jones matrices used to describe the transformation based on geometric optics simplifications. The image for each equivalent magnetic dipole, $n \times E(Q)$, is determined as though it sits on the optical axis and the lateral image position is subsequently altered using the actual dipole position and the magnification of the objective:

$$\mathbf{E}_{img}(r_d) = \frac{-jk}{2\pi} \iint\limits_{S_o} \mathbf{E}^{n \times E^i(Q)}_{eq,on-axis}(r_d + \beta q)\, dS \tag{3.11}$$

where q is a vector from the intersection of S_0 and the z-axis to the point Q and β is the magnification. The total intensity or image at the detector is found from the electric field found at the detector:

$$I = |\mathbf{E}_{img}|^2 \tag{3.12}$$

An image at each desired focal plane is a result of summing the contribution from each desired frequency. The process of computing images for each desired focal plane is simplified by altering the relative position of the resampled plane in relation to the focal plane of the objective. This means that only the final Debye-wolf algorithm must be recomputed for each desired focal plane. Fig. 3.2 illustrates the physical arrangement of the condenser and the objective where the condenser never changes position, meaning the scattered light calculated at the infinite plane does not change regardless of the position of the objective. The only difference is the distance between the infinite plane and the focus of the object. This idea is particularly important for modeling OPTM where projections are created by optically integrating through the cell.

3.2.5 Simulating a Projection

The image produced from the description above is from a single focused pulse whose point spread function is potentially not wide enough to illuminate the entire cell. As such, the focused pulse is scanned throughout the imaging plane interacting with the cell. The intensity image resulting from each scan position and wavelength is subsequently integrated to produce the final image at each focal plane. A projection

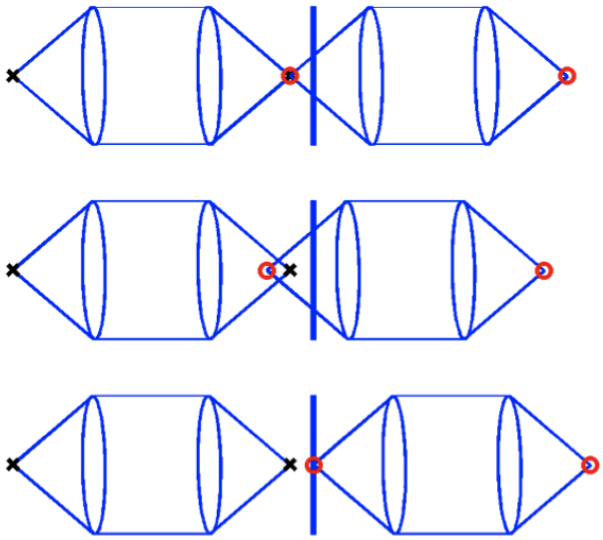

Figure 3.2: Representation of axially scanning the objective in comparison to the condenser illumination. Three different positions of the objective (on the right with red focal circles) are shown in relation to the condenser (on the left with black focal crosses) and the resampled infinite plane (vertical line). These diagrams show that the near-field scattered light produced by the object would be the same on the resampled infinite plane irrespective of the objective position. The only difference is the distance between the infinite plane and the focus of the objective (i.e. distance between red cross and infinite plane) meaning only the final image formation portion of the algorithm has to be repeated to axially scan through the object.

is the result of optically integrating different focal planes as the objective is axially scanned through the cell. The entire illumination and objective scanning process required to simulate a projection is mathematically encapsulated as:

$$P = \int_{z_{min}}^{z_{max}} \int_{\lambda_{min}}^{\lambda_{max}} \int_{0}^{2\pi} \int_{0}^{r_{max}} I(r, \theta, \lambda) r dr d\theta d\lambda dz \tag{3.13}$$

where (r, θ) are the polar coordinates of the focused pulse scan position, r_{max} is the maximum radial scan position dictated by the field of view and/or the cell size, I is intensity found due to each scan position using Eq. 3.12, λ is the wavelength interrogated between the minimum (λ_{min}) and the maximum (λ_{max}), and z defines the height of the objective focal plane between the minimum (z_{min}) and the maximum (z_{max}). The scan positions are implemented in Eq. 3.13 using a polar coordinate scheme due to the fact that these simulations employ radially symmetric objects, but they could be implemented using a Cartesian coordinate system.

Integration of Eq. 3.13 can be approximated using various discrete integration techniques such as extended midpoint and Gauss-Legendre. This work utilizes extended midpoint due to its ease of implementation. The radial and angular sampling intervals (Δr and $\Delta\theta$) are dictated by divisibles of the Rayleigh lateral resolution of an optical microscope, which is defined as:

$$R_{lateral} = \frac{1.22\lambda}{\mathrm{NA_{obj}} + \mathrm{NA_{cond}}} \tag{3.14}$$

The actual sampling interval is found by altering the scan distance in divisibles of the Rayleigh criteria and comparing the correlation coefficient produced in the final image stack. The angular sampling interval ($\Delta\theta$) is also found using the lateral resolution by setting the radial scan interval as a chord on a circle whose radius is the maximum radial scan distance. The angle is found by relating the chord and the radius to find the maximum common denominator of 360° where non common denominators unequally weight rotations at the beginning/end of the rotations. Mathematically

this relationship is described as:

$$\Delta\theta = \frac{360}{\left\lceil \frac{360}{2\sin^{-1}\left(\frac{\Delta r}{2\Delta r S_N}\right)} \right\rceil} = \frac{360}{\left\lceil \frac{180}{\sin^{-1}\left(\frac{\Delta r}{2\Delta r S_N}\right)} \right\rceil} \tag{3.15}$$

where S_N is the maximum number of scans. Since the maximum radius is found by multiplying the scan interval and the number of scans, this relationship is simplified, eliminating the radial sampling interval.

Fig. 3.3 illustrates Eq. 3.13 and the entire process required to compute a single projection utilizing the theory presented in Sections 3.2.1-3.2.4. Rather than running each simulation step a single time to produce an image, a projection is the result of running each step several times to acquire all the required data. All the data is subsequently integrated to produce a single projection. For OPTM, projections need to be produced for every desired perspective prior to reconstructing a 3D representation of the cell.

3.2.6 Three-dimensional Image Reconstruction

Experimentally acquired projections are reconstructed using the filtered backprojection method based on the projection-slice theorem [55]. This reconstruction technique mimics CT where x-rays are assumed to travel in a linear direction and absorption is the major contrast mechanism while refraction is the minor contrast mechanism. In OPTM, there are some obvious inconsistencies with the underlying linear, non-refraction assumptions used in the filtered backprojection, and thus the model provides the opportunity assess the range of NAs and scattering coefficients that the

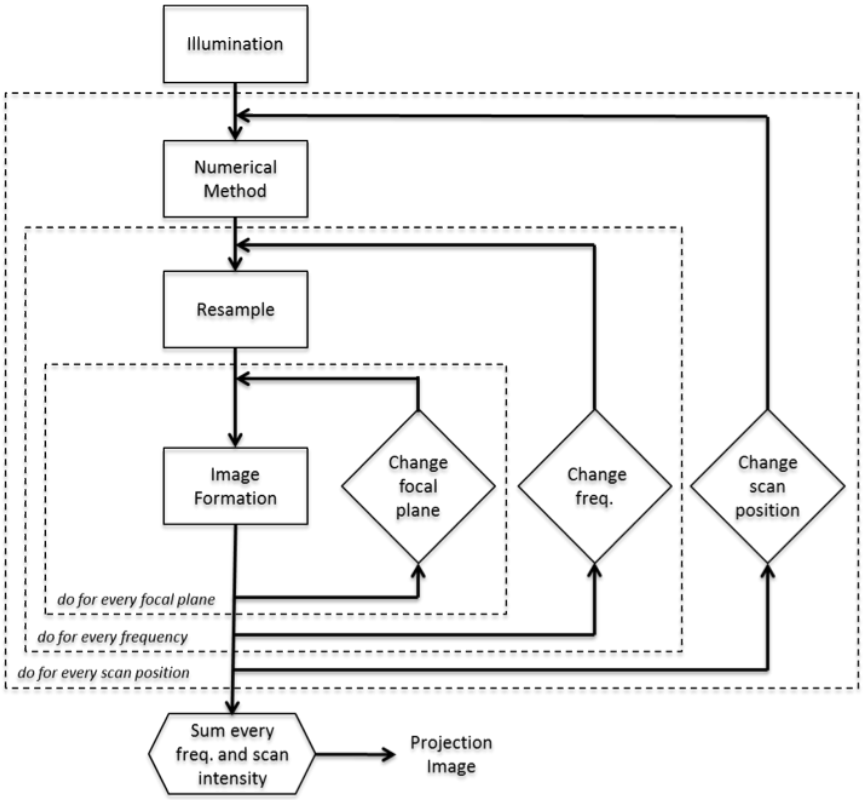

Figure 3.3: Diagram of the process to simulate an OPTM projection using visual for-loops. The illumination is defined for the desired illumination source and numerical aperture, which is incorporated in a numerical method to determine the near-field scattering from a cell. The near-field scattering is resampled for a particular frequency and used to compute an image at every desired focal plane. The near-field scattering is then resampled for another desired frequency and images are computed for all of the same focal planes. This entire process is performed for every scanning position to illuminate the entire cell. Each of these images is finally integrated to produce a single projection. Projections are acquired for each rotation of the cell and these projections are reconstructed into a three-dimensional image in a final post-processing step (not shown).

filtered backprojection is adequate for reconstruction.

The filtered backprojection can be performed for each position along the optical axis such that 1D projections are transformed to 2D slices rather than transforming

2D data to 3D. In this way, 1D Fourier transforms are taken on projections along the dimension associated with the angle of rotation. These 1D transforms are placed at the angle of rotation in a 2D matrix and the final slice is computed by taking the inverse 2D transform. The backprojection by itself acts as a low pass filter, producing blurry reconstructions. To reduce the effect of the transformation, a filter is often applied to the 1D transformed data to eliminate low frequency information and emphasize high frequency information. OPTM currently utilizes a variation of the ramp function where higher frequency is amplified and then removed beyond a point to reduce aliasing. The filtered backprojection is described mathematically as:

$$f(x,y,z) = \int_0^{2\pi} \int_0^{\infty} H(\xi) G(\xi,\theta,z) \exp\left(j2\pi\xi(x\cos\theta + y\sin\theta)\right) d\xi d\theta \tag{3.16}$$

where the 1D Fourier transformed projection data is $G(\xi,\theta)$ and $H(\xi)$ is the filter. The final reconstructed image is a 3D representation of the entire cell, which can be analyzed to understand the impact that each parameter has on the final reconstruction.

3.2.7 Methods

The OPTM model is implemented in this paper for the purpose of understanding the effect of condenser NA and object complex refractive index on image reconstruction of purely scattered light. This particular work reduces the computational complexity of the preceding model by assuming a micro-shell at the condenser focal plane, which reduces the number of projections to only one since every rotation produces the exact same projection. Further, laterally scanning the illumination is reduced as scans at

a single radial distance for various angles are approximated as pure rotations of the final intensity image. While polarization has a larger impact at high NA, reducing the accuracy of this assumption, its overall contribution is actually fairly small and is neglected in the theory of many high NA applications [43]. Without the preceding assumptions the computational cost, especially for high NA, becomes time intensive and beyond the computational capabilities of a single PC workstation.

The incident plane waves described in Eq. 3.1 are modeled as Gaussian modulated sine waves of the form: where $\tau = 2fs$, $f_0 = 4.283{\times}10^{14}$Hz, and $t_0 = 9\tau$. These parameters result in a pulse centered at 588 nm, mimicking OPTM incident light, which is bandpass filtered (see Fig. 1.2) to look specifically at the Hematoxylin stain. The focused pulses, ranging in NA from 0.1 to 1.3, illuminate micro-shells with an outer radius of 1.5 μm and inner radius of 1.35 μm. The micro-shells are situated in media similar to optical gel whose refractive index is set at 1.45, similar to that of glycerol [74]. The refractive index inside the micro-shell matches that of the surrounding media so the only source of contrast is the shell. The refractive index of the shell is similar to experimentally tested microspheres [68] with a complex refractive index of $1.50 + j0.001$. Complex refractive indices of $1.45 + j0.001$ and $1.50 + j0.0$ are also simulated to better understand the individual impact of absorption and refraction on the final reconstruction.

The micro-shells are executed using the staircasing method, which is a standard technique in FDTD where curved boundaries are represented as a series of block-like steps. The FDTD grid spacing is set at 15 nm ($\Delta x = \Delta y = \Delta z$) and the simulation is run at 95% of the 3D Courant limit ($0.95/\sqrt{3}$) for 2048 time steps. The

FDTD grid is terminated using an eleven cell CPML with the total grid dimensions of 360×240×240cells. One dimension is extended such that scanning is performed in a single grid by moving the micro-shell instead of the focused pulse. For the first scan position, the micro-shell is placed at one end of the grid and the focused pulse is aimed at the center of the micro-shell. The remaining scan positions are the result of focusing the illumination at the same position and moving the micro-shell at pre-defined intervals toward the extended grid dimension. The scanning intervals, found using the method described in Section 3.2.5, are set to a maximum of $3/4R_{lateral}$, which produced correlation coefficients in the final image stack above 0.99. The scan intervals are further dictated by the grid spacing such that the actual sampling intervals are 0.36 μm for NA 0.1, 0.27 μm for NA 0.5, 0.225 μm for NA 0.9 and 0.195 μm for NA 1.3. Each scan is extended to 1.8 μm in radial distance from the center of the micro-shell. The FDTD algorithm is implemented in parallel utilizing Message Passage Interface (MPI) to transfer magnetic fields between the sub cubes in the 3D topology. MPI is also used for the remainder of the implementation to parallelize computation among the available computer resources.

The illumination TFSF coefficients are pre-computed for the entire FDTD time sequence where the superposition of each plane wave is performed concurrently to reduce the overall computer memory burden. Once the TFSF coefficients are computed for a specific grid size, the FDTD algorithm can be run in the time required to introduce a single plane wave. This has an obvious advantage for lateral scanning the micro-shell. Additionally, the TFSF coefficients are computed using the Analytical Field Propagation (AFP) method, which offers significant advantages when dealing

with numerical dispersion related to introducing plane waves at angles close to the Cartesian axes [103]. Numerical dispersion is an inherent effect in FDTD where waves travel at slower than desired velocities due to the number of cells per wavelength with which they are discretized and the angle that they travel with respect to the grid axes [115]. AFP requires a significant upfront computational demand, particularly when performed for a superposition of such a large number of plane waves, but the numerical dispersion advantages outweigh the computational cost disadvantage. TFSF coefficients are periodically loaded into memory throughout the FDTD algorithm to reduce the memory burden on the computer system. Most 3D implementations of the TFSF technique rely on either the single frequency compensation [115] or the matched numerical dispersion [42] techniques. These techniques are not as accurate as AFP [115], but they have reduced computational costs in situations where scanning relative to a focused pulse is not performed in a single grid.

The scattering is calculated for three different wavelengths spanning the 60 nm bandpass filter centered at 588 nm. There is no significant variation between the scattering produced by the upper and lower bounds of the bandpass filter, justifying the limited number of frequencies. Specifically in one test, the two wavelengths produce a Pearson Correlation coefficient above 0.99. This high degree of similarity reduces the computational cost significantly. The previously defined simulation parameters and the DFT dictate the interrogated wavelengths are 555.3 nm, 581.7 nm, and 610.8 nm.

The infinite plane, used in the resampling, is placed at 2.5 μm along the optical axis from the focus of the illumination and the width is set to 20 μm in both lateral

directions with a sampling of 200 nm. Both the width and the sampling interval are found by computing the correlation coefficient of final reconstructions using subsequently smaller sampling intervals and larger widths. The final width and sampling interval are determined where the correlation coefficient for the final reconstruction is above 0.99 produced using windows with adjacently computed parameters. Depending on the application, a correlation coefficient below 0.99 could be afforded to improve computational efficiency, but visual inaccuracies were noticeable for out-of-focus illumination in the axial cross section with lower correlation coefficient standards.

The light on the infinite plane is imaged through an objective with the same parameters across all simulations with a 1.3 NA and 100× magnification. The detector space has a refractive index of 1.0 and the focal plane is scanned axially through the object from -5 μm to 5 μm at 0.2 μm increments. The axial scanning interval was determined to maintain a correlation coefficient of 0.99 in the reconstruction. In the magnified detector space, the images are calculated from -400 μm to 400 μm at 8 μm increments mimicking pixel spacing in standard CCD and CMOS cameras. All image units are demagnified in the figures presented below.

As previously mentioned, the final images are approximated by reducing the illumination to a single radial direction and all other angles are approximated as rotations of the intensity image for that radial distance. Rather than using Eq. 3.15 to determine the scan position of the focused pulse, it is instead used to determine the rotation interval for the final intensity images; all rotations are performed in MATLAB (Mathworks, Natick MA) using the *imrotate* function with linear interpolation. The projection is the result of integrating every frequency, focal plane, and scan position

(Eq. 3.13 and Fig. 3.3). Reconstructions using the projections are performed with the MATLAB *iradon* function using the Ram-Lak filter where the simulated projection is replicated 500 times to mimic OPTM acquisition every 0.72° over the entire 360° of rotation.

3.3 Results

The best point to start analyzing OPTM image formation is prior to axially summing the 3D image stack to produce a projection. A set of micro-shell images produced with varying condenser NAs and an idealized representation are shown in Fig. 3.4. The micro-shells have an extinction coefficient of 0.001 while their real refractive index is matched to the surrounding media. The resulting image cross sections are individually normalized.

The image stack produced using the 0.1 NA condenser is unable to focus on the micro-shell where there are two hot spots symmetrically located at approximately 5 μm, well outside the actual dimensions of the micro-shell. The actual location of the micro-shell only contains interference fringes. Since these results provide such an inadequate means to focus on the micro-shell, they are ignored for reconstruction and further analysis. The 0.5 NA condenser provides a more effective means to focus on the micro-shell as the object shape is starting to resemble the idealized cross section; however, the axial dimensions are extended to approximately $\pm 3.5 \mu m$. This extension is due directly to the large depth of field, approximated as three times the lateral resolution (i.e. Eq. 3.14). As the condenser NA gets larger, the depth of field gets smaller and the image stacks begin to better resemble the idealized representation.

The 0.9 NA condenser extends the maximum intensity to approximately $\pm 1.8 \mu m$ while the 1.3 NA condenser does not extend the micro-shell axially by any appreciable amount.

The 0.9 NA condenser also slightly distorts the out of focus edges of the micro-shell creating a boxy looking representation at either edge. This distortion is the result of constructive and destructive interference by out of focus waves, which is verified using a thinner micro-shell with an inner radius of 1.35 μm. Using this particular sized micro-shell, reduces the effect material properties have on imaging where the illumination and object shape have greater importance. While these results are not shown, the thinner micro-shell causes distinct interference fringes where the 0.9 NA condenser produces a large destructive interference pattern through the optical axis center of the micro-shell. The fringes produced by the 1.3 NA condenser are greater in number, but smaller in size. These constructive and destructive fringes become less noticeable as the micro-shell increases in thickness due to increased scattering.

While a smaller depth of field provides better representation of the physical dimensions, it does a worse job of illuminating out of focus edges of the micro-shell. The 0.9 NA condenser reduces the out-of-focus micro-shell edge contrast to only 75-80% of the in-focus plane contrast, while the out of focus portion of the micro-shell illuminated using the 1.3 NA condenser is only 60-65% of the in-focus plane. These variations in intensity at different focal positions impact the reconstructions, as the projections are unequally weighted towards the portion of the object closer to the condenser focal plane. The fact that depth of field gets smaller with increasing NA is verified by looking at the maximum value from each plane in the axial cross section.

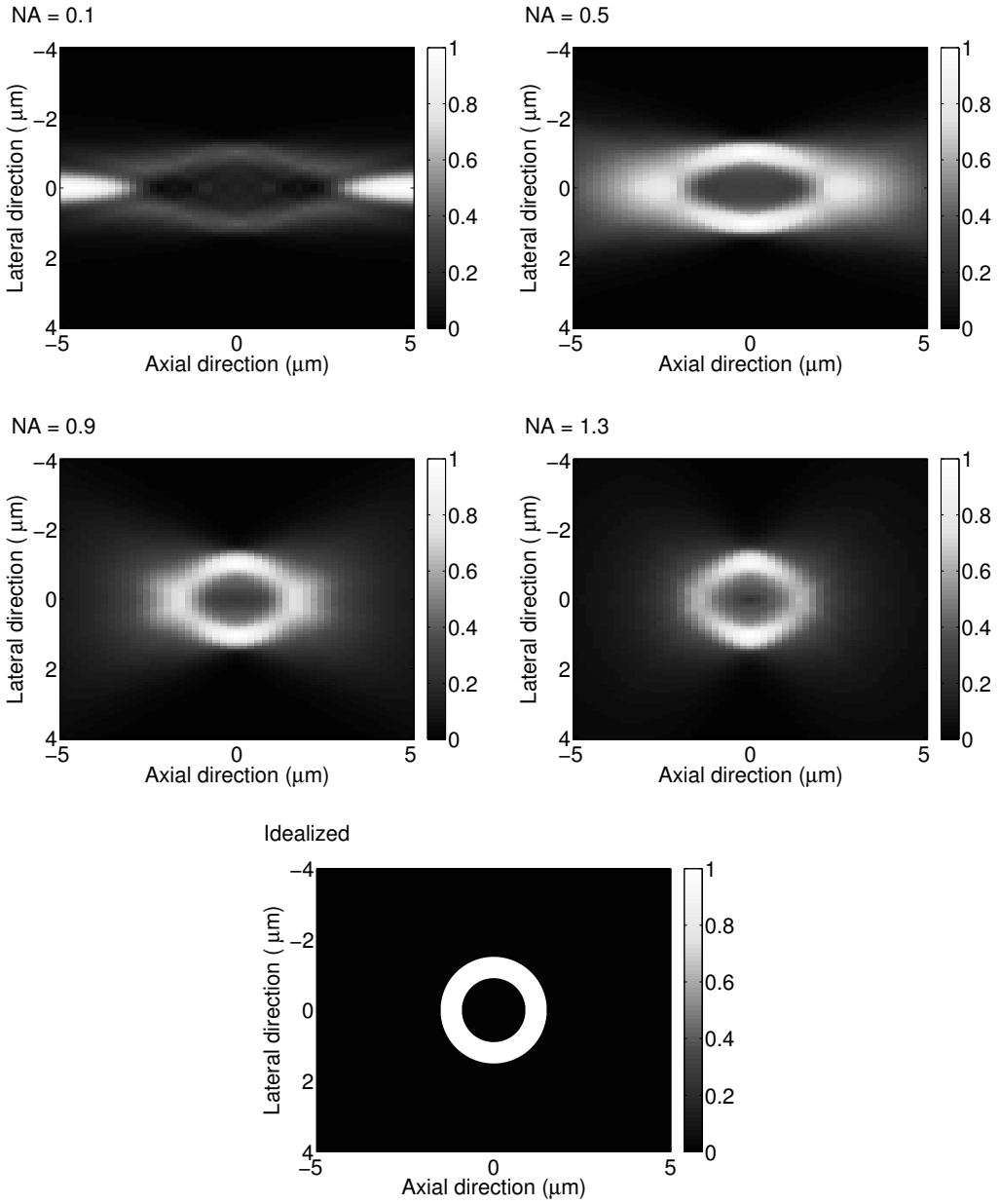

Figure 3.4: Axial cross section for varying numerical apertures of scattered light with a constant micro-shell refractive index of $1.45 + j0.001$ in media with a refractive index of 1.45. The idealized cross section is also provided for comparison purposes. Each cross section is individually normalized.

Ideally the maximum should be constant throughout the outer radius dimensions of the micro-shell and then be completely zero outside the micro-shell; however, it is apparent that the maximum intensity begins to fall immediately as the objective scans away from the condenser focal plane.

Fig. 3.4 also shows symmetric scattering above and below the focal plane in the pure absorption cross sections. As real refractive index is incorporated into the micro-shell, the image stack is no longer symmetric along the zero focal plane and it becomes imbalanced to one side, depending on the mismatch. This particular feature is seen more explicitly in the 0.5 NA condenser results of Fig. 3.5 where the maximum intensity on the right side of the micro-shell is only 90% of that on the left side. If the micro-shell has real refractive index less than the surrounding media then light is focused beyond the micro-shell in the positive direction. Alternatively, a micro-shell real refractive index greater than the surrounding media causes the hot spot to be reflected in the negative direction. This same lensing effect is described using microspheres in the optical trap literature [11, 19, 104]. As in the optical trap work, the effective focal length (i.e. the location of the hot spot) is reduced with increasing NA [19]. These results seem to indicate that changes in real refractive index have a smaller effect on the image stacks produced with higher NA condensers than those produced with smaller NA condensers. This conclusion has been verified using both microspheres and micro-shells with real refractive indices ranging from 1.4 to 1.55, which encompass the majority of biologically relevant refractive indices. It is also important to note that for these simulations the pure absorption images are three orders of magnitude smaller than those with the real refraction, meaning the real refraction

is providing greater contrast than the absorption.

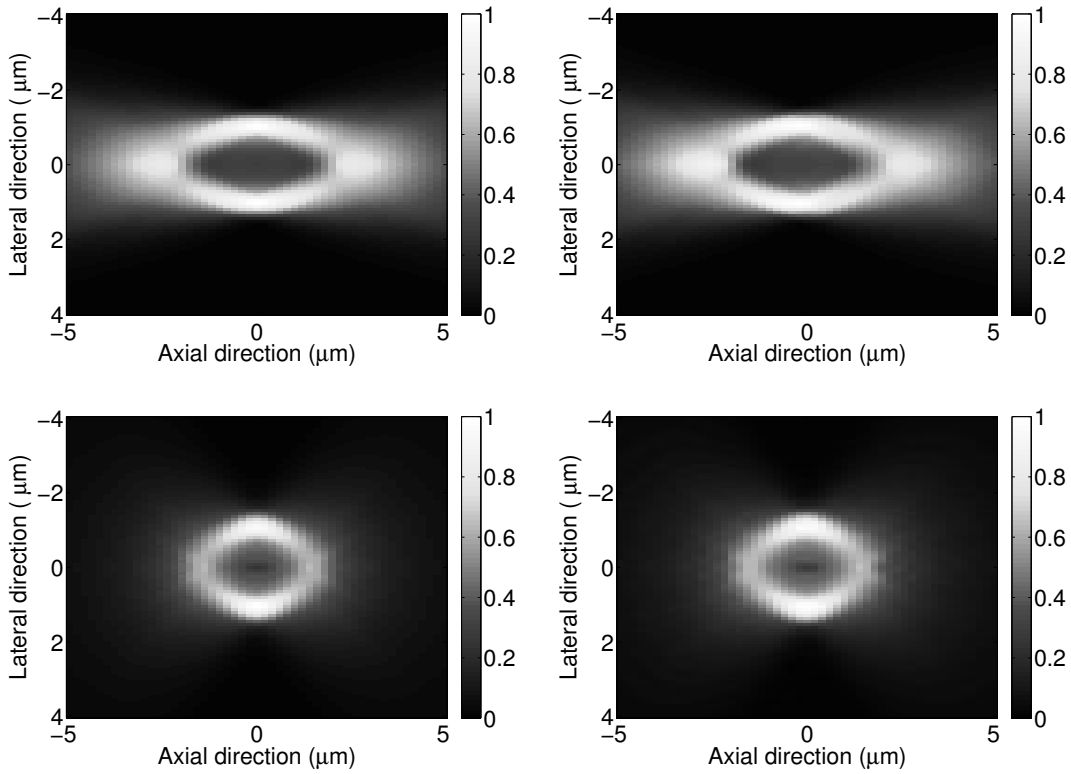

Figure 3.5: Axial cross sections produced using the 0.5 NA condenser (top row) and the 1.3 NA condenser (bottom row) for micro-shells with complex refractive indices of $1.45 + j0.001$ (left column) and $1.5 + j0.001$ (right column). The micro-shells are placed in media with a refractive index of 1.45. Each image is individually normalized, but the pure absorption micro-shells have approximately three orders of magnitude less contrast.

Finally, the axial stacks of images are summed to produce projections, which are reconstructed using the filtered backprojection and displayed with the idealized micro-shell reconstruction. Fig. 3.6 shows superimposed plots of the cross section of the reconstructed images with varying NA where the cross section is the same in all directions. Both the axial and lateral cross sectional reconstructions are the

exact same due to the symmetry in the reconstruction, thus the axial cross section is arbitrarily displayed. The 1.3 NA reconstructed image is also provided in Fig. 3.6 for the reader's curiosity. All cross sections reach their maximum at approximately the same position, but the peak widths are smaller for increasing NA where the peaks better represent the dimensions of the micro-shell.

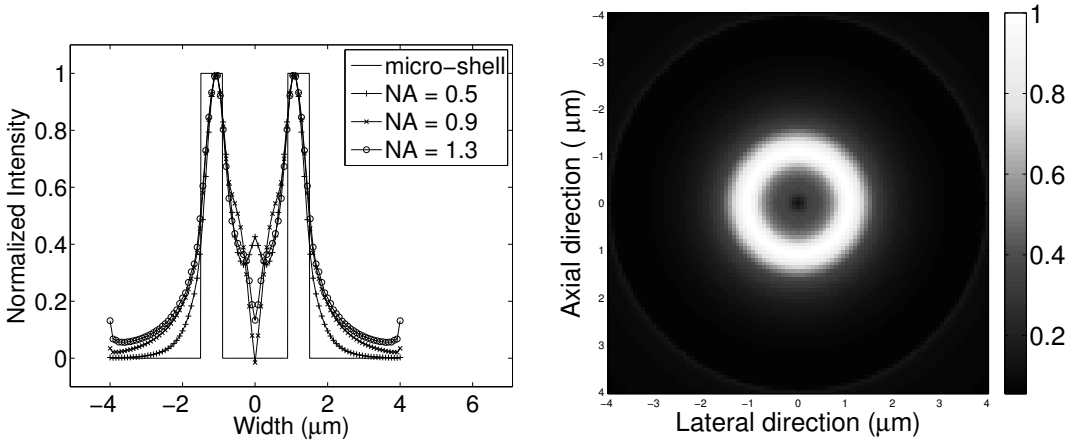

Figure 3.6: Cross sectional reconstruction plot (left) for varying NA for 0.5, 0.9, and 1.3 with a constant micro-shell refractive index of $1.5 + j0.001$. A 1.3 NA reconstruction (right) is also provided. Each NA intensity plot is individually normalized.

Interestingly, the 0.9 NA cross section reaches a lower center value than the 1.3 NA cross section due to better illumination of out of focus edges with the worse depth of field. These parameters mean there is a greater distinction of shell versus non-shell, despite the dimensions not being represented as well. If a larger shell were used then the 0.9 NA condenser would still illuminate more of the shell, but not be able to illuminate the out of focus edges as well as this example. These results could justify altering the illumination used in OPTM.

One apparent down side of increasing NA is the excess energy outside the dimen-

sions of the micro-shell reconstruction as seen in Fig. 3.6. This excess energy is due to the blooming effect seen at out-of-focus points in Fig. 3.4. The image stacks resulting from lower NA condensers are cylindrically shaped patterns while the higher NA condensers produce hourglass shaped scattering as a result of incident rays propagating from larger angles. The hourglass shape introduces energy outside the actual dimensions and changes in the projections depending on the sweeping distance. In Fig. 3.7, reconstructions with NA of 1.3 are displayed where projections produced by sweeping from -2 μm to 2 μm are compared to those produced by sweeping from -5 μm to 5 μm. These images show that by limiting the amount of axial information included in the projections there is a major impact on the overall reconstruction where there is less energy outside the micro-shell dimensions while the reconstruction inside the dimensions of the micro-shell is approximately the same. In the inner diameter of the micro-shell, there is also less energy by limiting the sweeping distance. The negative value in the $\pm 2\mu m$ sweep is due to the MATLAB assuming the maximum value is at the center of the projection, which is not the case for micro-shells. The projections do not contain any negative values.

3.4 Discussion

The model presented above provides the ability to analyze OPTM image formation in a much more systematic way than can be performed experimentally. For example, where analyzing different condenser NA configurations would each require their own condenser, the model can predict results by simply changing a few parameters. Also, the model provides the ability to isolate various refractive index components to deter-

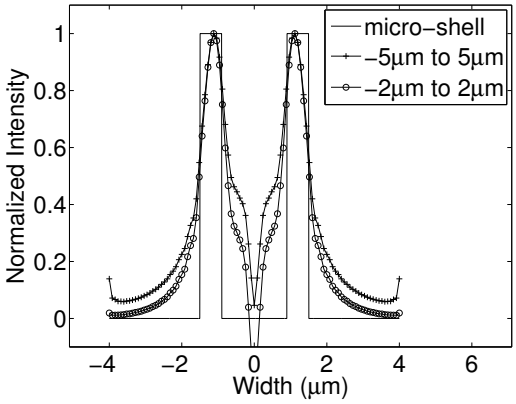

Figure 3.7: Cross sectional reconstructions produced with a condenser whose NA is 1.3. The projection consists of axial scanning from $\pm 5\mu m$ or $\pm 2\mu m$ for a micro-shell with a refractive index of $1.5 + j0.001$. Each plot is individually normalized.

mine their overall affect, which would be otherwise impossible to do experimentally. The preliminary data offered above is synthesized into four take away points that should be utilized in the future for improved image reconstructions using OPTM. These include:

1. High NA condensers preserve axial shape information more effectively when compared to low NA condensers;

2. High NA condensers should be scanned in conjunction with the objective to equally weight all axial information of the object in the projections;

3. Refractive index differences do not significantly affect reconstructions for data acquired using high NA condensers; and

4. Improved scanning based on a priori information is necessary for high NA condensers to eliminate blooming effect.

The first two points realize that the smaller depth of field of high NA condensers seems to have both advantages and disadvantages, where it more accurately represents the object dimensions, but it also does not provide even illumination. This improved understanding appears to indicate that the small depth of field of a high NA condenser requires that the condenser scan in conjunction with the objective in order to accurately depict larger objects. Without scanning the condenser, the object is not evenly illuminated meaning the contribution to projections is disproportionately weighted towards those regions of the cell, which are closest to the condenser focal plane. Scanning the condenser in conjunction with the objective not only provides better illumination of the cell, but it might also be possible to reduce the scan range from 360° to 180°. The decision to scan over the entire 360° was made to average out differences between projections acquired with 180° of separation, which were believed to be a result of scattering. These results suggest that these differences are in fact more a result of disproportionate illumination rather than scattering, which has a smaller role in image reconstruction than initially believed. If these results continue to hold true it would play a vital role in improving projection acquisition time as only half the number of projections would be required. Future work must be done to optimize the amount and interval of rotation taking into account larger cell like objects, which could alter the scattering hypothesis.

The chosen micro-shell material properties indicate for these particular simulations pure refraction provides greater contrast compared to pure absorption. However, experimental implementation of OPTM reduces the effect of refractive index contrast by closely matching the refractive index of the immersion oil, micro-capillary, and

surrounding media to the absorptive stained cell in order to highlight the absorption contrast mechanism. Obviously cells contain organelles whose refractive indices are not all the same and therefore cannot be matched with the surrounding media. Fortunately, the use of a high NA condenser seems to mitigate distortions, caused by pure refraction, in the reconstruction. The greater number of incident angles offsets or averages out scattering resulting from pure refraction. Smaller NA condensers, however, are easily scattered in one direction or another, altering the reconstruction to a greater extent. Objects with refractive indices much different than the surrounding media may distort this claim, but this should not be a problem for biological cells.

Seemingly one of the few downsides of using high NA condensers in OPTM is due to blooming of out of focus light, which is outside the lateral dimensions of the object itself. The easiest way to combat this blooming effect is to only scan the axial distance of the object and not beyond the object dimensions as simulated in Fig. 3.7. This method would eliminate a large percentage of the energy outside of the object dimensions. Alternatively, each focal plane could be acquired as a separate image, which would be individually segmented leaving only the object before summing the stack of images to produce a projection. This method could produce even more accurate reconstructions, but it would require alternative software and hardware to deal with this additional data.

Beyond the application of OPTM, the model presented could be used to better understand many different microscopy applications, especially those based on coherent illumination where some of the assumptions used for this work would not be necessary. For example, the model could be altered to simulate transmission mode

Optical Coherence Tomography (OCT) microscopy or phase contrast techniques, such as holography, for improved device implementation [17]. While OPTM tries to reduce the refractive index contrast mechanism, other techniques characterize cells by their organelle scattering. The model could be applied to these techniques to better understand the organelle originated light scattering signature of cancerous and noncancerous cells under focused illumination. Previous work individually evaluated the impact of each organelle on scattering utilizing plane wave illumination [31, 32], which produces a much different scattering pattern compared to focused illumination. Other work has utilized focused illumination to show there are different scattering processes associated with cancerous and noncancerous cells [112], but it does not pinpoint each organelles direct impact on the scattering process. Application of this model could bridge the gap between these manuscripts and provide a greater understanding of the light scattering properties associated with different organelles, both cancerous and noncancerous, for focused illumination. The results of this type of study could be applicable outside of microscopy in areas, such as flow cytometry, where cells are analyzed based on their scattering signature. The model presented above would require little alterations to simulate collection of scattered light produced by coherent, laser light incident on cells. Computational modeling has many applications throughout microscopy and general imaging where it provides the ability to better understand the impact of light absorption and scattering on image formation for improved image analysis and interpretation.

3.5 Conclusion

An algorithm is presented to examine OPTM, which is designed with the use of high NA condensers and objectives. The algorithm is used to examine the effect of condenser NA and micro-shell complex refractive index as a first example. The results of such analysis showed the benefits of using high NA condensers when it comes to representing the dimensions of the cell, but that high NA requires scanning the condenser in conjunction with the objective to better illuminate the entire cell. Also, the use of a high NA condenser reduces the effect of scattering on the reconstruction. The one downside is the introduction of blooming, which can lead to misrepresentations of the cell and could require alternative implementations. In the future, the algorithm will be experimentally validated using microspheres with known refractive indices and radii. Also, future algorithm development will incorporate other effects, such as non-linear scanning and incomplete micro-capillary rotation, to understand how each one affects the entire image formation process. From these results, development efforts will be triaged to improve the image formation process and enhance the diagnostic capabilities of the Cell-CT.

Chapter 4

MIE THEORY

4.1 Background

The original modeling technique relies on the FDTD method to calculate scattering around the object and the Stratton-Chu vectorial diffraction integrals to map this scattering to an infinite plane near the focal plane (see Fig. 3.1) [22, 104]. The near-field scattering calculated on the infinite plane is subsequently mapped to a final intensity image [85]. FDTD has many advantages such as the ability to look at arbitrary objects and interrogate a number of frequencies at one time; however, its computational cost can be quite high. In fact, the computational cost of FDTD has been described as the major limitation for 2D applications [120] and expansion to OPTM requiring as many as 500 projection images for non radially symmetric 3D objects seems nearly impossible.

As a means to mitigate this computational inefficiency, an alternative frequency domain technique is introduced to calculate near-field scattered light of a microsphere illuminated with a coherent, focused illumination source. This technique is directly comparable to the FDTD methodology, providing a framework to verify and optimize the FDTD simulation parameters and perform simulations that are computationally impractical using FDTD. Traditionally, the Mie theory has been used to calculate the scattering due to a microsphere, illuminated by a plane wave in both the near-

field [100] and the far-field [40]. In this case, near-field Mie theory [100] is combined with a technique capable of rotating the direction of the illuminating plane wave [32] to calculate the near-field scattering produced by a microsphere from a focused pulse. The focused pulse is similar to the one described in Chapter 3.2.1, which is the superposition of plane waves originating from directions within the condenser's NA. Rather than computing fields on an infinite plane in a two-part algorithm, like FDTD and the Stratton-Chu integrals, Mie theory accomplishes this task in a single procedure (see Fig. 4.1). While fields on this infinite plane are normally mapped to a final intensity image for modeling OPTM, this chapter is limited to the near-field scattering calculation to directly compare the computational cost of each method. However, the entire process to form a projection using Mie theory is very generally discussed in the form of visual for loops to compare the process with the FDTD method.

4.2 Theory

The difference between the original implementation and the one used for this work is the illumination is implemented below using an analytical method capable of determining the electromagnetic fields at any arbitrary point. By using this analytical method, the resampling portion of the original algorithm can be ignored [21]. The model provides the ability to simulate images of a microsphere with arbitrary size and material properties sitting in media with any refractive index. Since the micro-capillary and slide/coverslip provide near refraction free imaging they are ignored for this analysis [35]. Future research could be performed to include their minor effects

in the model. For this particular work, a variation of the original implementation is used where two steps are combined so that imaging is accomplished in three parts: illumination [15], near-field scattering [108], and image formation [85]. This implementation is computationally efficient compared to the original implementation, but it is limited to only looking at microspheres and not arbitrary objects. A general diagram of the modeling components used in image formation is illustrated in Fig. 4.1. The illumination is computed using an analytical method to compute the near-field scattering (scattering is used broadly to encompass the effects of refraction, reflection, and absorption) on an infinite plane in the direction of the condenser. The scattering calculated on this plane is mapped to the final image. Projections are produced by scanning the focal plane of the objective through the cell, which are subsequently reconstructed using the filtered backprojection.

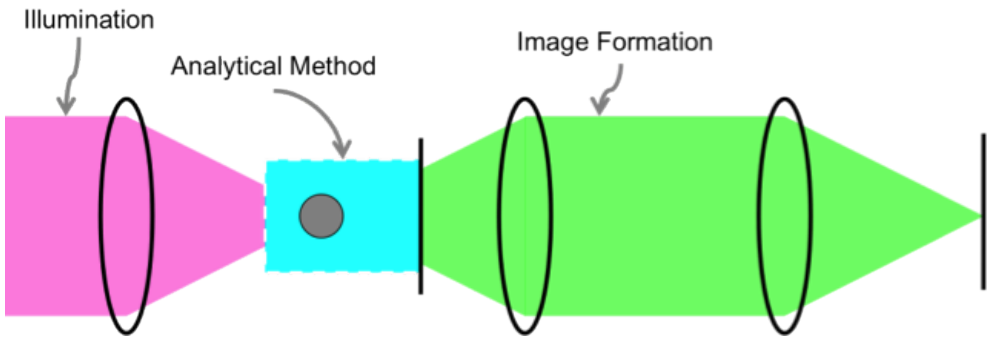

Figure 4.1: Mie theory diagram of the image formation model for a high NA bright-field, transmission microscope. The model consists of three main parts: illumination, analytical method, and image formation.

4.2.1 Illumination

Illumination is mathematically derived in the frequency-domain using coherent, polarized light, which is focused through a thin aplanatic converging lens [98]. Light rays polarized in the x-direction travel parallel to the optical axis interacting with the lens before being diffracted by the exit pupil. The direction of each ray after interacting with the lens is determined by geometric optics where each ray describes the direction and polarization of different plane waves propagating proximal to the focus. The resulting electric field around the focal plane is a superposition of plane waves [119]:

$$\begin{aligned} E_c(r_P) &= \frac{f}{2\pi c}\iint_S \frac{\cos^{1/2}(\theta_i)}{s_z} E_S(r)\exp\left[(ikr_p\cos\left(\varphi_i-\varphi_p\right)\sin\theta_i)\right] \\ &\quad \times \exp\left[(ikz_p\cos\theta_i)\right]\, ds_x ds_y \end{aligned} \tag{4.1}$$

integrated over the domain $S = \{(s_x, s_y)\in\mathbb{R}^2 \mid s_x^2+s_y^2 \leq n\sin\theta_{max}\}$ where f is the focal length of the condenser and c is the speed of light. The Cartesian coordinate variables of integration s_x, s_y, and s_z are directly matched with their spherical coordinate counterparts where $\theta_i = \cos^{-1}(s_z)$ and $\varphi_i = \text{atan2}(s_y, s_x)$. The maximum θ' is θ_{max}, which is the maximum angle of intersection with the optical axis as defined by the numerical aperture ($NA = n\sin(\theta_{max})$). $E_s(r)$ are the electromagnetic fields calculated from each plane wave incident from (θ_i, φ_i). The $cos^{1/2}(\theta_i)$ factor is a result of the intensity law of geometric optics, dampening the intensity of waves coming from the edge of the lens as compared to those propagating a shorter distance from the center of the lens [23]. Finally the sphere position (r_p, φ_p, z_p) is only included

in the phase terms, meaning every plane wave can be computed first and then the superposition can be performed subsequently for every desired scan position. The focused pulse can be evaluated for any desired wavelength and the equation can be approximated discretely using numerical integration methods.

4.2.2 Analytical Method

The scattered light from each plane wave necessary for Eq. 4.1 is calculated using near-field Mie theory [108]. Traditionally, Mie theory is used to simulate scattered fields from an x-polarized plane wave propagating in the z-direction; however, Török *et al.* presented another method allowing plane waves to propagate from arbitrary directions within the condenser NA [119]. Their technique utilizes far-field Mie theory to look at gold spheres small enough that scanning is not required, thus the computational advantages of the technique are not fully realized. Rather than altering Mie theory such that it calculates scattering from incident rays propagating from arbitrary directions, the computational plane behind the sphere is altered to include the appropriate yaw, pitch, and roll such that the fields calculated are the correct ones for the desired incident ray.

Near-field Mie theory is based on Bromwich functions to calculate scattering of a plane wave due to a sphere with a diameter d and a complex refractive index of $m = n(1 - ik)$ where $k = \omega(\epsilon\mu)^{1/2}$ is the wavenumber [108]. The sphere, positioned at the origin, scatters an x-polarized plane wave of wavelength, λ, traveling along the z-axis. The scattered light can be observed at any arbitrary observation point

$r = (r, \theta, \phi)$ and the spherical electric fields at observation point r are:

$$
\begin{aligned}
E_r^S &= E_0 \cos\phi \sum_{n=1}^{infty} i^{n+1}(-1)^n \frac{2n+1}{n(n+1)} a_n \left[\zeta_n''(kr) + \zeta_n(kr)\right] P_n^1(\cos\theta) \\
E_\theta^S &= \frac{E_0}{kr} \cos\phi \sum_{n=1}^{infty} i^{n+1}(-1)^n \frac{2n+1}{n(n+1)} \left[a_n \zeta_n'(kr)\tau_n - i b_n \zeta_n(kr)\pi_n(\cos\theta)\right] \\
E_\phi^S &= -\frac{E_0}{kr} \sin\phi \sum_{n=1}^{infty} i^{n+1}(-1)^n \frac{2n+1}{n(n+1)} \left[a_n \zeta_n'(kr)\pi_n - i b_n \zeta_n(kr)\tau_n(\cos\theta)\right]
\end{aligned} \tag{4.2}
$$

where E_0 is the intensity of the plane wave, $P_n^1(\cos\theta)$ are the associated Legendre polynomials of the first kind, and $\pi_n(\cos\theta)$ and $\tau_n(\cos\theta)$ are the Legendre functions. The primes indicate the derivative of the function with respect to the value in the parentheses. The $\zeta_n(kr)$ function is a complex combination of spherical Bessel and Hankel functions and a_n and b_n are known as the scattering coefficients, dependent on size parameters and half-ordered Bessel functions. The infinite discrete summations are truncated by the Wiscombe's criterion:

$$
n_{max} = \text{round}\left[2 + k_0 r + 4(k_0 r)^{1/3})\right] \tag{4.3}
$$

where the higher order functions are dampened by the $((2n+1))/((n(n+1)))$ coefficients reducing their overall contribution.

The scattering from the sphere is calculated on a single infinite plane distal to the condenser focal plane where the plane is rotated using a matrix formalism such that the fields calculated are the correct ones for the desired incident ray. The fields computed on this altered plane are then rotated back such that they are aligned with the original coordinate system. These rotations are performed using rotation matrices

dependent on the incident direction [119]:

$$\mathrm{RW}(\theta_i, \phi_i) = \begin{pmatrix} \cos\theta_i \cos^2\phi_i + \sin^2\phi_i & -\sin(\theta_i/2)\sin(2\phi_i) & -\cos\phi_i \sin\theta_i \\ -\sin(\theta_i/2)\sin(2\phi_i) & \cos^2\phi_i + \cos\theta_i \sin^2\phi_i & \sin\phi_i \sin\theta_i \\ -\cos\phi_i \sin\theta_i & -\sin\phi_i \sin\theta_i & \cos\theta_i \end{pmatrix} \tag{4.4}$$

where plane waves originate from the angles (θ_i, ϕ_i) are systematically determined by the NA and the mutual coherence sampling theorum [7]. The microsphere scattered light is calculated where there are two coordinate systems: the standard coordinates and another coordinate system that aligns with each incident plane wave indicated by a prime. The original observation points on the infinite plane are rotated by the incident ray using the rotation matrix:

$$r = \mathrm{RW}(\theta_i, \phi_i) \cdot r' \tag{4.5}$$

to compute near-field Mie theory in the incident plane wave coordinate system. After computing all the desired electromagnetic fields on the rotated infinite plane, the fields are converted into Cartesian coordinates:

$$\begin{aligned} E_x^S &= \sin(\theta)\cos(\phi)E_r^S + \cos(\theta)\cos(\phi)E_\theta^S - \sin(\phi)E_\phi^S \\ E_y^S &= \sin(\theta)\cos(\phi)E_r^S + \cos(\theta)\sin(\phi)E_\theta^S + \cos(\phi)E_\phi^S \\ E_z^S &= \cos(\theta)E_r^S - \sin(\phi)E_\theta^S \end{aligned} \tag{4.6}$$

which are then rotated back to the original Cartesian coordinate system by:

$$\mathbf{E}_S(r') = \mathrm{RW}^{-1}(\theta_i, \phi_i) \cdot \mathbf{E}'_S(r') \tag{4.7}$$

where $r' = \mathrm{RW}^{-1}(\theta_i, \phi_i) \cdot r$. This rotation matrix method provides the ability to compute electric fields on the same infinite plane for every incident angle. These fields are combined using Eq. 4.1 where the microsphere location can be altered to scan the focused pulse in the imaging plane.

4.2.3 Image Formation and Reconstruction

Image formation, objective scanning, and reconstruction are performed using the same algorithms presented previously in Section 3.2 and published in [23]; here they are only briefly summarized. The entire procedure is depicted in Fig. 4.2, which is directly comparable to the FDTD procedure illustrated in Fig. 3.3. The electromagnetic fields computed on the infinite plane are mapped to the final image using the Debye-Wolf integral [121] where the image of each equivalent magnetic dipole on the infinite plane is computed separately before performing a coherent superposition to determine the image at the detector. This process computes an image for a focused pulse at a single position, which potentially is not wide enough to fully illuminate the entire object. The object is fully illuminated by scanning the focused pulse based on Rayleigh criteria where the image from each scan position is integrated to build a single in-focus image and a broadband image is formed by repeating the process for every desired wavelength.

The Debye-Wolf integral allows the infinite plane to be placed at any arbitrary

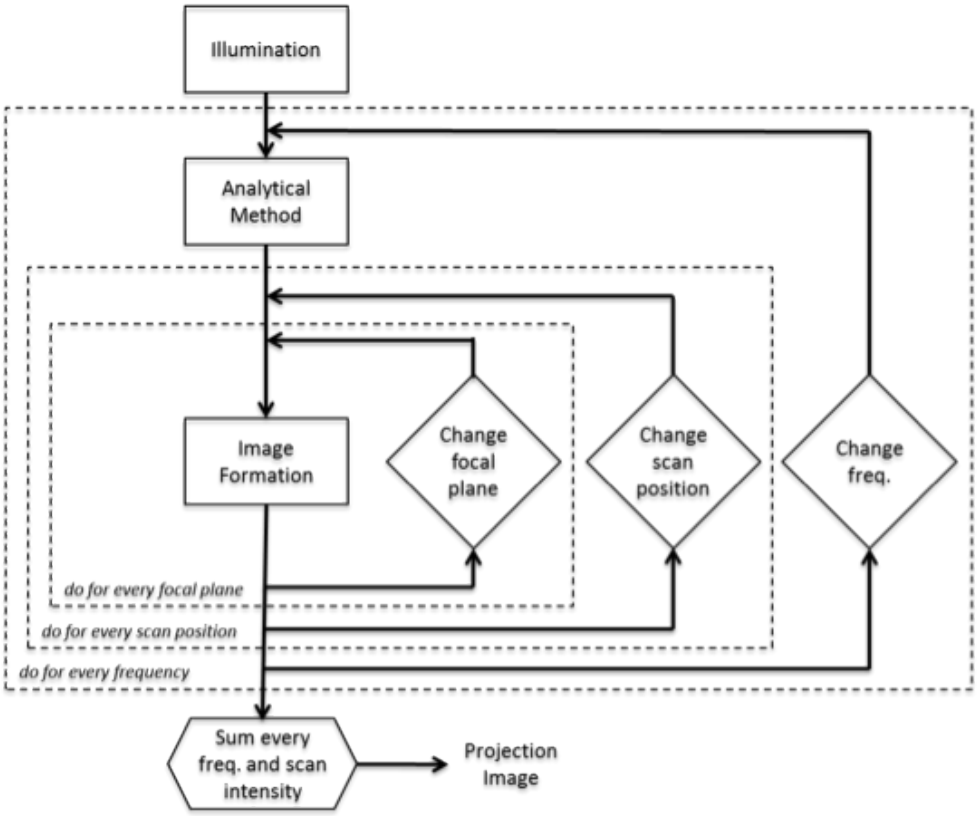

Figure 4.2: Diagram of the process to simulate an OPTM projection image using visual for-loops. The illumination is defined for the desired illumination source and NA, which is incorporated in the analytical method to determine the scattering on an infinite plane near the microsphere. The near-field scattering is used to compute an image at every desired focal plane for all scan positions to illuminate the entire cell. Then the analytical method is performed for another desired frequency and images are computed for all of the same focal planes. Each of these images is finally summed to produce a single projection image. Projection images are acquired for each rotation of the cell and these projections are reconstructed into a three-dimensional image in a final post-processing step (not shown).

position relative to the condenser focal plane such that scanning the objective is accomplished by re-computing only the final portion of the imaging algorithm (see Fig. 3.2). The images for each scan position are then integrated to find a projection and projections are formed for every angle of rotation in the micro-capillary before

reconstructing a 3D image using the using the filtered backprojection [54]. The filtered backprojection is performed for each position along the optical axis such that 1D projections are transformed to 2D slices rather than transforming 2D data to 3D. The final reconstructed image is a 3D representation of the entire cell, which can be analyzed to understand the impact that each parameter has on the final reconstruction.

4.3 Methods

The technique described in this chapter is directly compared with the FDTD and Stratton-Chu method presented in Chapter 3 though a microsphere is imaged instead of a micro-shell. In order to match those results and compare the computational cost of each method, the near-field scattering plane is set to 2.5 μm from the condenser focal plane using a 1.5 μm radius microsphere with a refractive index of 1.40 (comparable to cytoplasm [12]) in media with a refractive index of 1.45 (refractive index of glycerol [75]). The condenser NA is set at 1.3. The focused pulse is scanned in a single radial direction away from the center of the microsphere utilizing the fact that the scattered fields produced from one radial distance are approximately the same for each angle of rotation around the sphere. Scanning is performed from 0.075 μm to 1.8 μm in 0.075 μm increments (24 scan positions) and the infinite plane is 24 μm wide in both lateral directions with 0.1 μm sampling. Each simulation probes 555.3nm, 581.7nm, and 610.8 nm wavelength light.

The FDTD grid, in the original method, is 360×240×240 points where the one length is extended such that scanning is accomplished inside a single grid. The in-

cident plane waves are introduced into the FDTD grid using the TFSF formulation where the TFSF coefficients are pre-computed and periodically loaded into memory throughout the time stepping. Pre-computing the TFSF coefficients allows the entire focused pulse to be introduced in the same time required for a single plane wave. The fields computed in the FDTD grid are mapped to the infinite plane using the mixed surface implementation of the Stratton-Chu integrals [22] employing the same parameters as described above. Both sets of simulations are performed on a 2.13GHz dual quad core workstation running Linux and are performed in parallel using the MPI. While each simulation could be parallelized among more processors, the available computer cluster is made up of many nodes with greatly varying processor speeds and this procedure allows for a more direct comparison of the computational cost.

The computational cost of each simulation is loosely analyzed by looking at the time required to compute each step of the respective algorithm. Furthermore, the number of rays, frequencies, and scans performed directly scales various parts of each algorithm. Each of these variables is probed to determine their effect on the overall computational cost. The computational cost of the FDTD and Stratton-Chu simulation is represented by the following pseudo equation:

$$C_{FDTD} = t_{TFSF}R + (t_{FDTD} + t_{Stratton-Chu}F)S \tag{4.8}$$

where t is the time required for to compute the TFSF coefficients, run the FDTD method, and perform the Stratton-Chu resampling, R is the number of rays, F is the number of frequencies, and S is the number of scans. The TFSF time is the time to

compute coefficients for a single plane wave and the number of rays directly scales this time. The first term is pre-computed to run the simulation and allow a desired focused pulse to be used for any number of objects provided they fit in the total-field portion of the FDTD grid. Removing this first term from Eq. (4.8) is referred to as the pre-computed FDTD algorithm for the remainder of the chapter. This term is removed because often times it might be important to look at the same sized objects with different refractive indices and in this case, the TFSF coefficients have already been computed. The number of scans necessary to illuminate the microsphere determines the algorithm's computational cost.

The near-field Mie theory has a much easier computational cost pseudo equation:

$$C_{Mie} = t_{Mie} RF \tag{4.9}$$

where t_{Mie} is the time required for to compute a single plane wave using Mie theory. This time is directly scaled by the number of rays and the number of desired frequencies. Illumination scanning is not represented in this equation because it is a negligible time cost as a result of Eq. (4.1).

4.4 Results and Discussion

The original FDTD method and the new near-field Mie theory were performed on the same microsphere with the same refractive index such that they can provide verification for each method. Fig. 4.3 shows two example near-field intensity images computed using near-field Mie theory at 2.5 μm from the condenser's focal plane. The intensity is the absolute value of the electric fields squared. For all scan positions and

wavelengths compared, the two methods produced a Pearson Correlation coefficient greater than 0.9997 making them nearly identical. The slight variations are due to various numerical artifacts inherent in FDTD (i.e. numerical dispersion [115]]) and computer simulations (i.e. bit rounding).

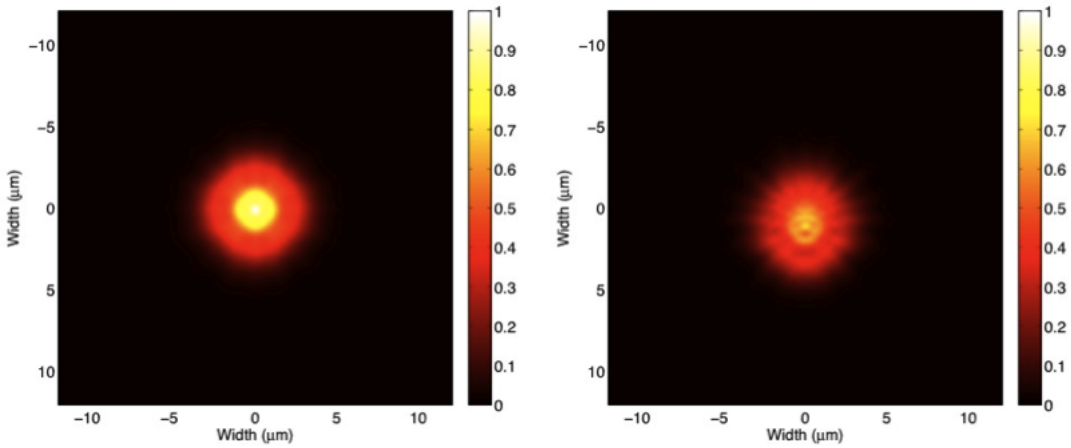

Figure 4.3: Example intensity plane of the scattered electric fields at 2.5 μm from the condenser's focal plane where the focused pulse is located laterally at 0.075 μm (left) and 0.75 μm (right) relative to the center of the sphere. The images are produced with 555.3 nm wavelength light and both are normalized by the maximum intensity value obtained in the 0.075 μm scan. The corresponding FDTD intensity planes are not shown as their Pearson correlation coefficient with the Mie theory generated planes is above 0.9997.

The computational cost of each method is compared to explore the advantages and disadvantages of each technique. Table 4.1 provides an approximate computational cost of each time variable in Eqs. (4.8) and (4.9) as calculated on the single machine. From these time costs, it is possible to start to paint a picture of where each method provides the smallest computational cost. Fig. 4.4 plots the computational cost of the FDTD algorithm, the pre-computed FDTD algorithm, and the Mie theory algorithm.

Table 4.1: Approximate computational cost of each time variable in Eqs. (4.8) and 4.8).

Variable	Time (minutes)
t_{TFSF}	3
t_{FDTD}	38
$t_{Stratton-Chu}$	48
t_{Mie}	0.5

While the number of rays, scans, and frequencies are plotted separately, the number of rays and scans are interlinked. As the NA is increased, more rays are necessary to approximate the focused illumination, which in turn requires more scans because the PSF is smaller. Additionally, the refractive index mismatch between the media and the sphere has a slight impact on the time cost for Mie theory and not the FDTD algorithm; however, it is ignored because the difference is so small that it will have negligible impact on the overall calculations. To illustrate how rays, scans, and frequencies independently affect each simulation, the number of frequencies is held constant at 3, the number of rays is held constant at 488, and the number of scans is held constant at 24, except when that particular parameter is being altered. These are the same parameters used in the 1.3 NA FDTD simulation in Chapter 3 and [23].

Fig. 4.4 shows the large computational advantage of Mie theory over the two variations of the FDTD algorithm. If the TFSF coefficients are pre-computed then the FDTD algorithm can be computationally more efficient for simulations where three or less scans are necessary. Additionally, while not seen on the graph, the pre-computed FDTD algorithm becomes computationally more efficient only when more than 2912 rays are used to approximate the illumination. In all other cases the Mie

theory is computationally advantageous over the FDTD method.

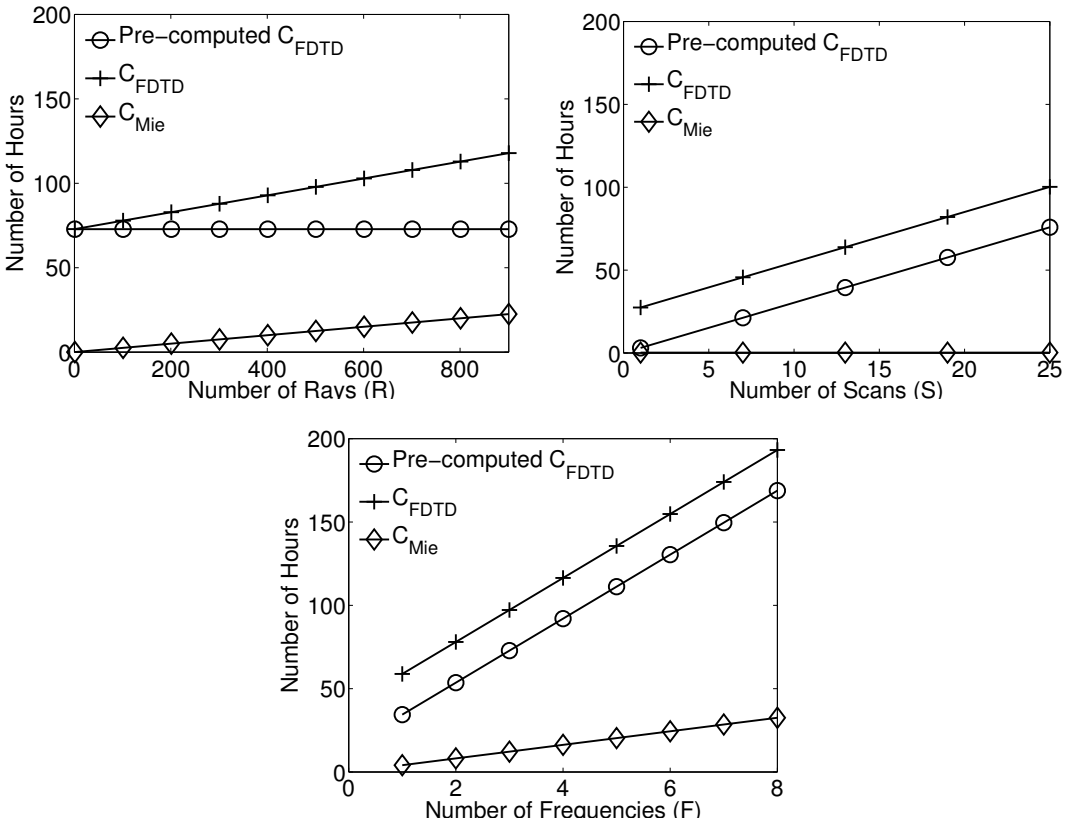

Figure 4.4: The computational cost of the FDTD/Stratton-Chu algorithm, the FDTD/Stratton-Chu algorithm where the TFSF coefficients were pre-computed, and the Mie theory algorithm for varying number of rays (top left), number of scans (top right), and number of frequencies (bottom). The number of frequencies is held constant at 3, the number of rays is held constant at 488, and the number of scans is held constant at 24 for each simulation except with that particular parameter is being altered.

The computational advantages of Mie theory could provide an opportunity to investigate many image formation effects in OPTM that are not computationally possible using FDTD. One example is the axial displacement of microspheres in the micro-capillary in comparison to the condenser focal plane. In OPTM, microspheres

immersed in optical gel are pushed through the micro-capillary where they are not necessarily positioned at the rotational axis of the micro-capillary. Therefore, the microsphere follows a circular path around the micro-capillary axis of rotation and its axial position changes relative to the condenser focal plane. These axial displacements will have an effect on the projections produced potentially resulting in variations in the reconstruction. This particular simulation would be computationally prohibitive using FDTD where illumination for each of the 500 projections could take 100 hours or more to run. On the other hand, Mie theory allows the same illumination to be accomplished in a single run since the microsphere is arbitrarily placed after computing the scattering from each plane wave (see Eq. 4.1).

The size of the microsphere plays an important role in the computational cost of both the FDTD and the Mie theory algorithms. Not only does it affect the run times, but it also requires a variable number of scans to adequately illuminate the entire sphere. For example, increasing the microsphere size will increase the run time of both FDTD and Mie theory, but it will also require an increased number of scans, which will more drastically affect the FDTD method as scans do not modulate the Mie theory. The computational cost for a single microsphere size is presented due to the large number of variables that would be required to be changed for variable sizes. However, it is important to note that the computational cost of the FDTD algorithm is $O(N^3)$, while Mie theory is not affected to the same extent due to Wiscombe's criterion. Thus increasing the size of the microsphere does not have the same effect on the computational cost of Mie theory as it does on FDTD. There is, however, one major tradeoff associated with Mie theory. The implementation only provides the

ability to image microspheres and not arbitrary objects, such as cells. Mie theory has also been developed for cylinders [41] and stratified spheres [118], but analytical methods are not available for arbitrary objects. The stratified sphere and cylindrical object types are associated with more sophisticated theory leading to more difficult implementations. On the other hand, the FDTD method can be utilized to model OPTM for symmetric objects, such as a hallow sphere; however, its computational cost could prohibit its usage for non-symmetric objects requiring scanning not on a single radial direction but across the entire object's dimensions and where 500 projection images could be necessary to accurately perform a 3D reconstruction.

4.5 Conclusion

A computationally efficient Mie theory technique is presented to compute near-field scattering from focused illumination where the algorithm utilizes rotation matrices to compute scattering due to plane waves propagating from arbitrary directions. The computational cost of the algorithm is compared to the FDTD method presented in Chapter 3. In almost all cases, the computational advantages of the Mie theory technique supersede those of FDTD for imaging microspheres. The method presented in this chapter makes it possible to determine, among other things, the impact of axial displacements on projections and ultimately the final 3D reconstruction in OPTM.

Chapter 5

EXPERIMENTAL COMPARISION

5.1 Background

Microscope design normally relies exclusively on experimental methods. A researcher develops an idea, implements it in hardware, and tests the device to determine the problems. Newer generation devices are then designed by iteratively refining the idea in a slow, expensive loop based on hypotheses formed from the previous generation. More recently, computer processing speed and parallelization techniques have made simulation a viable method to perform microscope design where researchers can quickly and inexpensively test hypotheses. However, in many cases assumptions still must be made to produce results in a reasonable time frame. These assumptions can lead to results that are not seen experimentally. Rather than using experimental methods or simulations separately, design should be performed using both methods in conjunction. This chapter illustrates one example within OPTM where the combination of both methods is driving improved microscope design and will ultimately lead to quantitative microscopy.

In OPTM cells are not necessarily embedded at the center of the micro-capillary lumen, so for every angle of rotation the cell changes position (see Fig. 5.1). In order to account for this changing position, a tracking system is employed to monitor the cell position and to scan the objective a pre-defined distance above and below

the cell. At the same time, the condenser focal plane is fixed at the center of the micro-capillary. As the micro-capillary is rotated, the center of mass of the cell is directly matched with the condenser focal plane at exactly two locations in the circle of rotation and away from the focal plane for every other rotation. Measuring this effect quantitatively with a test target placed at exact trajectory radii is nearly impossible; instead this particular work utilizes the Mie theory formulation, presented in Chapter 4, to simulate microsphere images and provides a relative experimental comparison. The use of both experimental methods and simulations provide the ability to refine conclusions and improve system design in a more robust methodology.

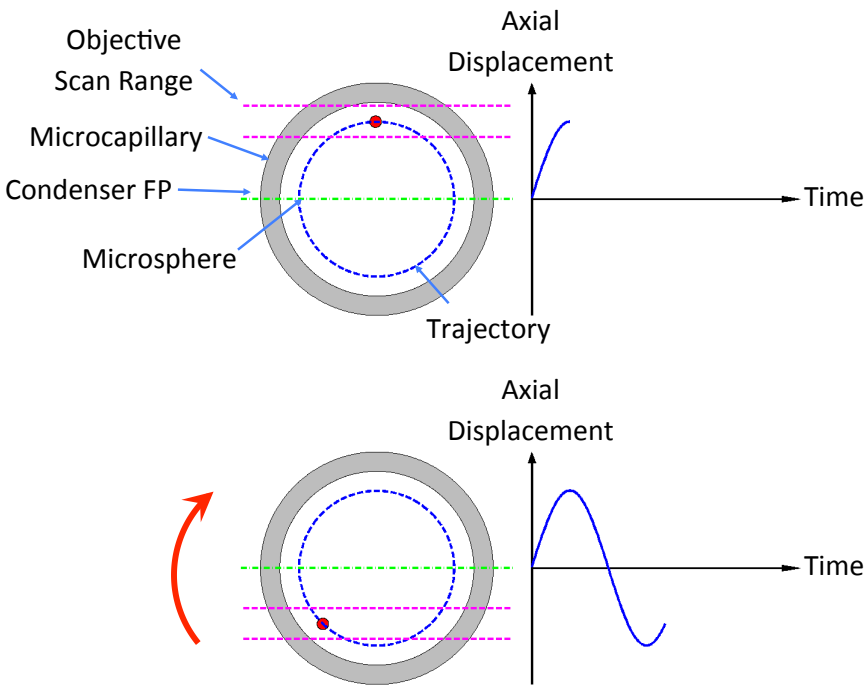

Figure 5.1: Illustration of the simulation performed for this work at two time points. A microsphere is placed inside the micro-capillary. As the micro-capillary (and microsphere) rotate clockwise, the microsphere centroid is plotted on the right where the objective scan range is axially displaced with the microsphere, while the condenser focal plane remains at the center of the micro-capillary.

5.2 Methods

5.2.1 Simulation

The simulation produces reconstructions of purely scattered light where coherent illumination interacts with the object to form an image. Despite the fact that OPTM is based on bright-field microscopy, coherent focused illumination is appropriate due to the coherence length provided by a 60 nm bandpass filter [23]. Furthermore, current modeling techniques based on partially coherent illumination are unable to model axial displacements [16]. The focused pulse, used for this work, is capable of incorporating axial displacements though it represents an extreme case, and simulation conclusions should be tempered through experimental methods. This computational model is described in Chapter 4 and published elsewhere [25], but a brief description is provided to orient the reader. The model is composed of three parts (see Fig. 4.1): mathematical description of the illumination, calculation of the scattering around a microsphere, and remapping the scattering to the final image.

As described in Chapter 4, the focused illumination is broken down into component parts where plane waves with different amplitudes propagate from different directions within the NA to interact with the microsphere. The interaction of each plane wave with the microsphere is calculated independently and then subsequently combined before calculating the final image. This understanding is particularly important for this work where the microsphere is constantly changing axial positions relative to the condenser focal plane as it rotates in the micro-capillary. Therefore the interaction of the microsphere with each plane wave is calculated once, and then the scattering

from each plane wave is combined for each desired microsphere position. The final image at each objective focal plane is calculated from this superposition.

Pure scattering reconstructions of a 1.5 μm radius microsphere are produced with 588 nm wavelength light where the microsphere and media have refractive indices of 1.45 and 1.50, respectfully. Analysis provided in Chapter 3 shows that the addition of biologically relevant refraction does not significantly alter the reconstruction when illumination is provided by a high NA condenser [25]. The single wavelength provides accurate results for the 60 nm bandpass experimental setup [25] and the axial displacement of the microsphere follows a trajectory as seen in Fig. 5.1 where the radius ranges from 0 μm to 20 μm in 5 μm increments. These radii sample possible trajectories inside the 25 μm radius micro-capillary though the micro-capillary is not included in the simulation since its refractive index is matched to the optical gel [35].

Five hundred projections are simulated over 360° for each trajectory using matching 100× condensers and objectives with no aberrations and NAs of 1.3. The condenser focal plane is fixed to the center of the micro-capillary while the objective scans 5 μm peak-to-valley (PTV) around the microsphere center of mass. The in-focus images are calculated from -400 μm to 400 μm at 8 μm increments mimicking pixel spacing in standard CCD and CMOS cameras. The projections for each simulation are reconstructed into a 3D image using filtered backprojection with a Ram-Lak filter [55]. The algorithm is implemented in MATLAB and C++ with the MPI library to parallelize the calculations across a computer cluster. Even with this setup, the simulation takes approximately five days to compute on 56 nodes.

5.2.2 Experimental

Uniform silica microspheres (Bangs Laboratories Inc., Fishers IN) are imaged to mimic the size of cell nuclei with a radius of 1.565 μm. The microspheres are carefully chosen for their material composition and their refractive index. The silica composition is important since Xylene, which melts and distorts the size of plastic, is used to remove water in the cell preparation technique. Furthermore, microspheres are typically classified by their refractive indices with little absorption present. This contrast combination is opposite of the cells typically imaged using the Cell-CT, so the microsphere was iteratively chosen whose refractive index is 1.43-1.46. This refractive index range provides enough contrast from the 1.51 refractive index optical gel to be barely visible, but not enough that light is refracted off of the surface.

The contrast is marginally enhanced by washing the microspheres in Hematoxylin and centrifuging the solution for three, 2min cycles. After the last cycle, the pellet is washed with Xylene and suspended in Smart Gel OCF-452H (Nye Lubricants Inc., Fairhaven MA). The microsphere and gel solution is injected into a fused-silica capillary (Polymicro Technologies, Phoenix AZ) and imaged using the Cell-CT. Illumination and imaging are provided by matching 100x oil immersion objectives with 1.3 NAs (Olympus, Center Valley PA). The microspheres follow 0μm and 23.435μm trajectories where the second microsphere is bound to the 25μm radius micro-capillary inner wall. 72 projections are acquired over 360° by scanning the objective FP 5μm PTV around the microsphere center of mass. The objective is moved to the microsphere center of mass at each rotation using a MIPOS 500 PZT Scanner (Piezosystem Jenna, Hopedale MA) and projections are formed by remotely scanning the objective

FP in a secondary lens setup to refocus the light to all desired FPs [8]. The secondary setup consists of an objective matching the illumination/imaging ones and a custom circular mirror displaced using a PA 25/14 SG Stack Actuator (Piezosystem Jenna). Following image acquisition, the projections are processed by subtracting the background and performing median filtering to further increase contrast. The microsphere projections are registered using Phase Correlation [61] and reconstructed using the filtered backprojection.

5.3 Results and Discussion

5.3.1 Simulation Results

X, Y, and Z cross sections of the simulation reconstructions are provided in Fig. 5.2. Visually, the 0 μm reconstruction provides the most accurate portrayal of the microsphere physical dimensions extending to the edge of the 1.5 μm radius. The contrast also remains fairly constant throughout the microsphere except for a dip near the center, which is a result of destructive interference. As the trajectory radius is increased, the reconstructions do not maintain the same physical dimensions and the contrast is no longer constant. The 5 μm reconstruction (Fig. 5.2, 2nd row) is smaller in size and the total contrast is only 52% of the 0 μm 3D image. As the trajectory radius increases, the total contrast continues to decline and at radii greater than 10 μm the majority of the contrast is at a sharp peak in the center of the reconstruction. In this case, the peak is due to the extreme focusing used for this work and shows that the microsphere is focusing the light more than the condenser.

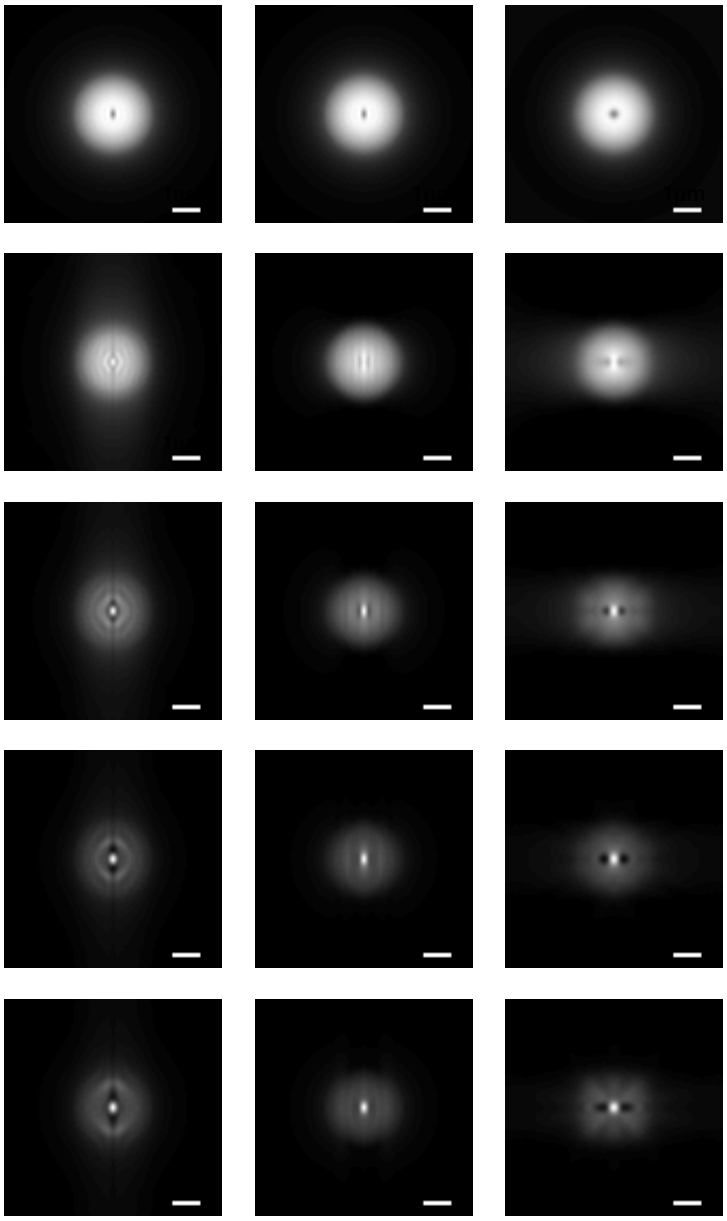

Figure 5.2: X (left column), Y (middle column), and Z (right column) cross sections of the reconstructions produced using the 0 μm (1st row), 5 μm (2nd row), 10 μm (3rd row), 15 μm (4th row), and 20 μm (5th row) radii simulation trajectories. Each image is normalized by the maximum value in the 0 μm total reconstruction. The scale bars are $1\mu m$.

5.3.1.1 Analyzing Contrast

The first means to synthesize the results presented in Fig. 5.3 is done by analyzing the average contrast throughout the idealized microsphere dimensions. Specifically a mask is created using the idealized microsphere dimensions where everything outside of idealized microsphere radius is eliminated and the contrast within the microsphere dimensions is summed to produce a single number. The total contrast within each microsphere reconstruction is normalized by the total contrast in the 0 μm radius, providing a good indication of how well the condenser provides illumination when the microsphere is away from the condenser focal plane. As predicted, the contrast decreases as the trajectory radius increases. More interestingly, the contrast decreases by approximately 58% almost immediately as the trajectory radius is increased from 0 μm to 5 μm. This means that even small displacements of the object from the condenser focal plane hurts the contrast in the reconstruction. As the trajectory radius is further increased the reduction in contrast is less significant.

5.3.1.2 Analyzing Asymmetry

One of the obvious inconsistences in the reconstructions produced from the microsphere placed away from the center of rotation is asymmetry or spatial distortion. As a means to quantify radial asymmetry, the 3D reconstruction is resampled using vectors positioned from the center of the microsphere to the outer portion of the reconstruction. If the reconstruction is radially symmetric then each of these vectors would be the exact same, while asymmetry causes discrepancies between the resampled vectors. Fig. 5.4 provides a pictorial description of this process.

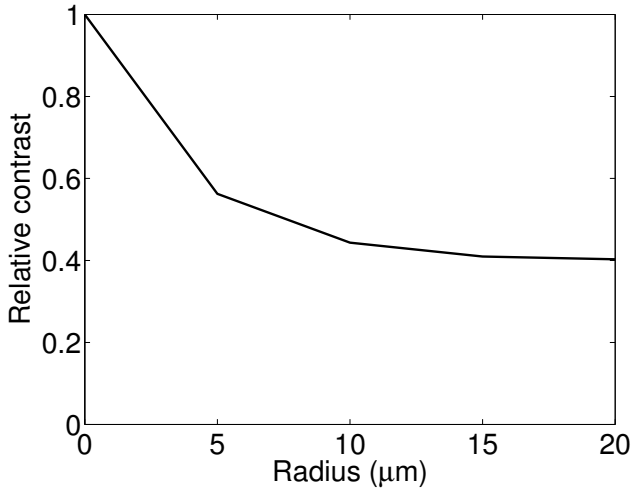

Figure 5.3: Plot of the relative contrast within the idealized dimensions of the microsphere reconstruction provided by the different trajectory radii.

In total 5000 vectors were used to resample the reconstruction where the angular directions were determined using the extended midpoint numerical integration technique. The vectors resampled the original reconstructions using with linear interpolation from 0 to 4 μm in increments of 0.08 μm. The vector length is based on the size of the images computed for the simulations, which encapsulates the majority of the energy. The results are presented in the left plot of Fig. 5.5. The idealized image shows the vectors extending to the microsphere 1.5 μm radius and all the vectors sampled from the different directions are the exact same. While the 0 μm reconstruction does not show the exact same binary values or microsphere dimensions as the idealized image, its vectors are almost exactly the same. As the radius is increased, there are flares in two particular regions of each of the other reconstructions. The increase in intensity at the center of each microsphere also increases as the trajectory radius increases.

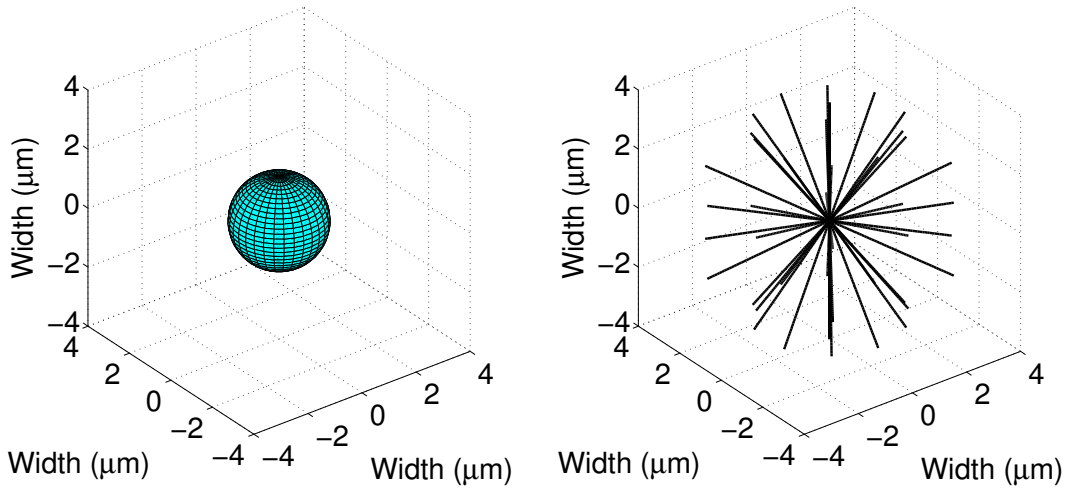

Figure 5.4: Pictorial description of the process used to analyze asymmetry in the reconstructions. The 1.5 μm radius microsphere (on the left) is resampled using vectors originating from the center of the microsphere (on the right) protruding 4 μm radially. The vectors are subsequently compared with each other to look at the overall radial symmetry of the reconstruction using the Sum Squared Error.

Each of the resampled reconstructions is summed along the arbitrary angle direction to produce the expected value at every radial distance. The expected value vector is compared with every resampled vector using Sum Squared Error (SSE) and the variance is normalized by the 0 μm reconstruction. Overall the variance increases as the trajectory radii increases except for the 20 μm trajectory (see right plot in Fig. 5.5). In this particular case, it seems that the reduction in contrast at this radius means there is less variation from the mean as compared to the 15 μm radius. From 0 μm to 5 μm, the variance jumps almost 11 times and is the most significant jump in the entire plot. This result backs up the conclusions from the contrast analysis and shows that future simulations should be performed within the 0 μm to 5 μm range to better understand image degradation.

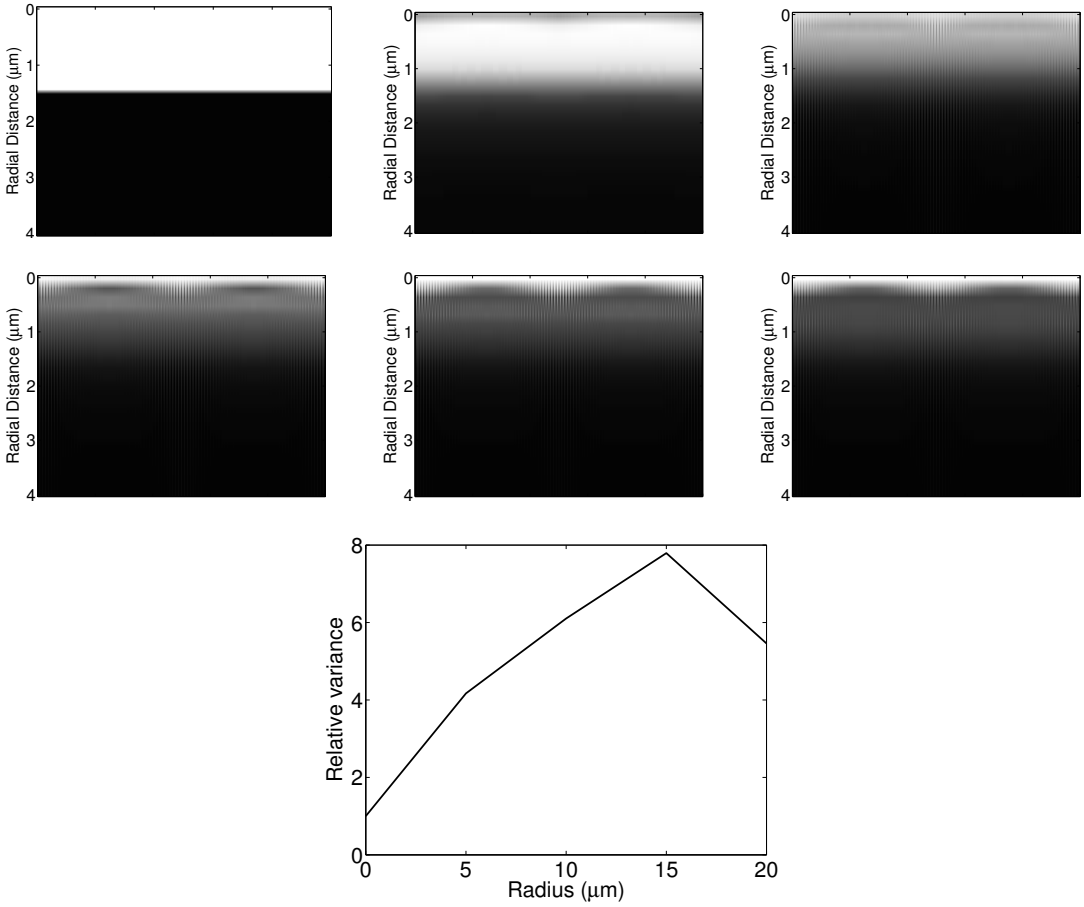

Figure 5.5: Images of the resampled vectors (top) used to analyze the asymmetry found in the reconstructions and the variance among the vectors along the radial angle (bottom). The angular location of the vectors is ignored since they are inconsequential. In the ideal case (top left of top plot) each of the vectors should be the exact same and the intensity should be white inside the dimensions of the microsphere and black outside. As the radius is increased, radial asymmetry becomes more apparent. The variance decreases at the last radius probably due to the reduced contrast provided by the illumination.

5.3.1.3 Projection Intensity

The intensity of each projection highlights the reason why the reconstructions are hindered by poor contrast and asymmetry. Fig. 5.6 shows the total contrast in each

projection as a function of trajectory axial height from the bottom of the micro-capillary to the top. The resulting intensity profile looks like a *sinc* function where the main lobe ranges $\pm 3.5 \mu m$ and the baseline value for projections outside this range is approximately 37% of the maximum intensity. As the trajectory radius is increased, a greater number of projections are contained outside the main intensity lobe, causing reduced contrast in the reconstruction. Also noticeable for the large trajectory radii reconstructions is the fact that the X and Y cross-sections are not the same. This discrepancy is another artifact caused by the intensity gradient around the condenser focal plane and accentuated by the slice-by-slice reconstruction used for this work. The size and shape of objects are distorted in a single slice where the intensity variation makes objects look oblong.

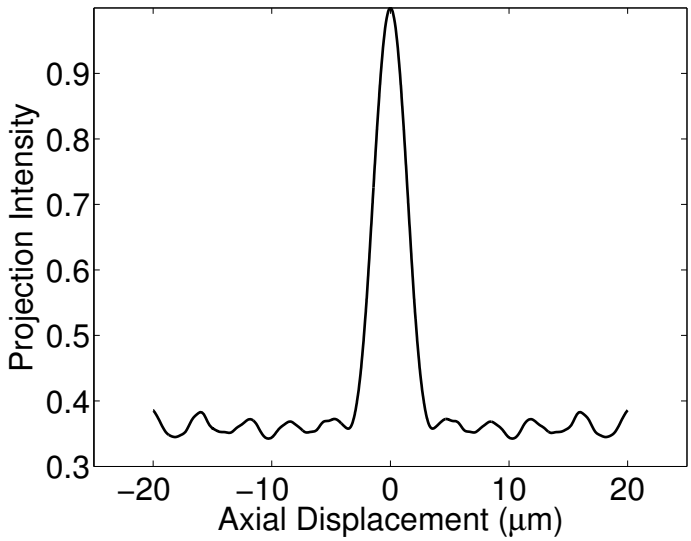

Figure 5.6: Normalized intensity versus axial displacement in projections computed using simulation where the microsphere centroid is changed from -20 μm to 20 μm.

5.3.2 Experimental Results

The experimental projections are much more difficult to acquire than a typical cell where the similar refractive indices of the microsphere and optical gel do not produce enough contrast for computer tracking. In order to combat this problem, the objective focal plane was originally scanned the full diameter of the micro-capillary to acquire projections. Under this procedure, the microspheres were fully visible around the condenser focal plane, but they disappeared near the top and bottom of the micro-capillary where they are over 20 μm away from the condenser focal plane. Further investigation of the simulation results revealed that projection intensity is a function of axial height as already discussed in Fig. 5.6. This improved understanding, provided by the simulation, led to reducing the objective scan range to 5 μm PTV, adding Hematoxylin, and manually tracking the microsphere.

Experimental cross sections are shown in Fig. 5.7 where both reconstructions well represent the microsphere physical dimensions. The intensity in the $0\mu m$ reconstruction is even throughout the entire microsphere whereas the $23.435\mu m$ image is brighter at the edges and darker in the middle. This result is opposite of the simulations due to the surface-bound Hematoxlyin, which is providing greater contrast at large trajectory radii. Before adding Hematoxlyin, the projections at distances far from the condenser FP were brightest in the center of the microsphere. Similar to the simulation results, the processed projections also have reduced intensity near the top and bottom of the micro-capillary (Fig. 5.8 right plot), except at the most negative displacements where a cloud of noise resulting from an unclean optical path is boosting the microsphere intensity. The unprocessed projections (Fig. 5.8 left plot), which are not as affected

by this noise cloud, show the intensity is reduced on either side of the condenser FP. The $0\mu m$ trajectory agrees with these results maintains at least 95% of the maximum intensity across all projections. The intensity gradient suggests that disappearance of the microspheres in the extended scan range projections was due to the high intensity near the condenser FP, which was averaging out the low contrast microsphere. If the microsphere was replaced with a larger or higher absorptive object then there would probably be enough contrast that they would not disappear in these full range scans. However the projections acquired far away from the condenser FP would have less of a contribution in the reconstruction and could produce non-symmetric artifacts as seen in the simulation results. These artifacts could be very detrimental in techniques requiring a larger capillary, such as one imaging needle biopsy tissue [18].

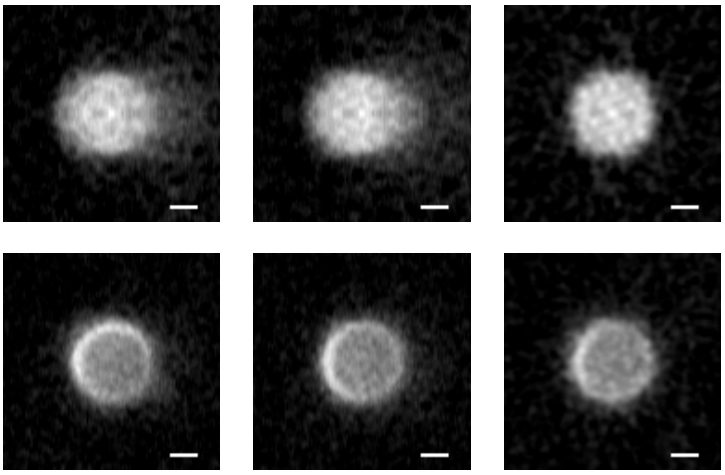

Figure 5.7: X (left), Y (middle), and Z (right) cross sections of the experimentally acquired microsphere. The objective focal plane is scanned 5 μm PTV around the microsphere center of mass. The scale bars are $1\mu m$.

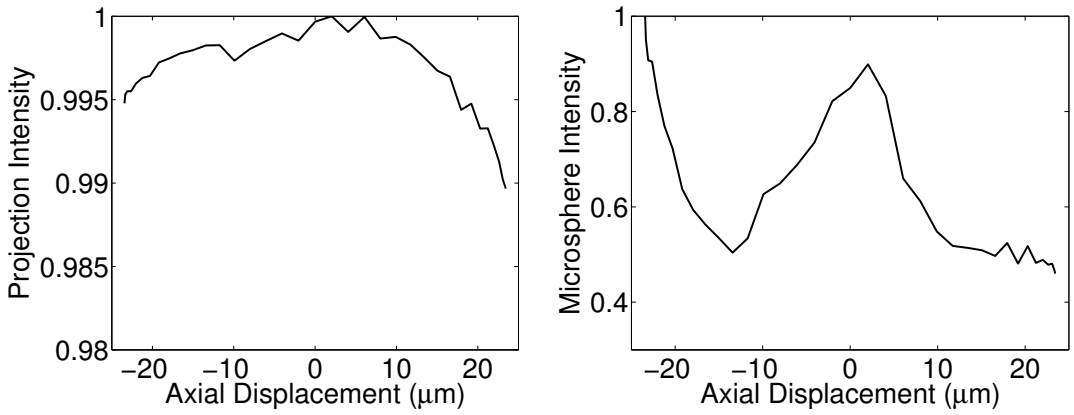

Figure 5.8: Normalized intensity versus axial displacement in experimentally acquired projections before (left) and after (right) subtracting background and median filtering.

5.4 Conclusion

This work demonstrates that a fixed condenser leads to projections whose intensities vary based on their axial distance to the condenser FP. Furthermore, these intensity gradients can lead to artifacts that distort the observed cell shape. The results presented above were not apparent previously in cells and were only found by this combination of simulations and experiments. Using both techniques, hypotheses were quickly tested in simulation and then improved experiments were designed to verify the results. These results are driving improved microscope design where VisionGate has fabricated a third generation of the Cell-CT. This article provides the first description of the new Cell-CT design that not only moves the condenser FP with the cell centroid, but also improves throughput to <2.5sec/cell by remotely scanning the objective FP. Preliminary reconstructions are qualitatively better than the previous generation based on the fixed condenser and future studies will confirm this quantita-

tively. The use of both simulation and experiments could improve microscope design for other applications as well and ultimately lead to more predictable performance for 3D cell imaging and diagnosis of disease.

Chapter 6

BEER-LAMBERT LAW

6.1 Background

Optical microscopes are the primary technology used within the field of clinical cytology where disease detection and diagnosis are performed by imaging fixed cells stained with absorptive dyes, such as Hematoxylin & Eosin. Ever since Antonie van Leeuwenhoek began applying microscopes to biomedical imaging by analyzing red blood cells in the 1660s, there has been limited improvement in mapping image pixel values to specific organelle optical properties. Instead, cytology is still a qualitative field, limited by an expert's ability to visually correlate cellular abnormalities with disease outcomes. Other imaging modalities have quantitative scales, which improves the sensitivity and specificity of disease detection. In Computed Tomography, for example, pixels are matched with tissue density through the Hounsfield Unit [46]. The future of optical microscopy will provide a similar ability to relate pixels values directly with cellular scattering and absorptive properties. Ultimately this type of development should improve the sensitivity and specificity of cytological disease detection. Several groups are currently working on developing new devices that relate cell scattering with disease progression [95, 112]. While that direction has shown promise, this particular work aims to make absorption-based techniques, currently the clinical gold standard, quantitative through the application of an improved Beer-

Lambert law.

Beer-Lambert law is an optical relationship that associates light transmission with the absorptive properties of the material through which it passes. In its traditional form, the law was derived for an unpolarized, monochromatic plane wave interacting with the normal boundary of a non-scattering material. Based on known illumination intensity, output intensity, and the path length, one can determine the absorption coefficient of the material. The law has far reaching impacts in many different fields including analytical chemistry to determine dilute molecular concentrations using spectroscopy [37], biology to measure light intensity irradiated on plants for daily canopy photosynthesis [101], and as previously mentioned, Computed Tomography [46]. In each of these cases, the application of Beer-Lambert law has provided the theoretical basis for transforming these technologies from qualitative classifiers to quantitative measurements.

The original Beer-Lambert law derivation is quite restricting in that it is only applicable for light, with a single wavelength, traveling in a single direction, interacting with an object that has no pure refraction. In order to ease some of these restrictions, correction factors have been introduced to deal with slight scattering errors [102, 28]. In a similar fashion, Beer-Lambert has been expanded to work with dispersive media with a high concentration of particles [29], mono- [27] and poly-dispersive aerosol media [26], and scattering by aggregates of random particles [63]. However, there has never been a form of Beer-Lambert that accommodates focused illumination. Due to this restriction, it has had limited influence on the field of optical microscopy where arguably it could have the greatest impact. The work presented below, describes a

superposition Beer-Lambert law with a theoretical comparison to show the foundation for future development of a Hounsfield-like unit that correlates absorption with cancer related chromatin abnormalities.

6.2 Theory

The original Beer-Lambert law says that the absorption is exponentially related to the absorption coefficient and the path length:

$$I_f = I_o \exp(-\alpha l) \tag{6.1}$$

where I_f is the final intensity, I_o is the initial intensity, α is the absorption coefficient, and l is the path length the light travels through the material. The absorption coefficient is wavelength dependent (λ_0) and directly related to the complex portion of the refractive index or the extinction coefficient, κ, where $\alpha = 4\pi\kappa/\lambda_0$. These same ideas are directly applicable to a superposition Beer-Lambert law for high NA illumination, which is based on theory derived for microscope computer simulations.

The theory for simulating partially coherent bright-field microscopy simplifies the illumination by discretely sampling the condenser lens with a number of rays (see Fig. 6.1) where the rays propagate from the lens towards the focus. Each ray actually represents a pair of orthogonally polarized plane waves whose amplitudes and directions are determined by geometric optics [16]. By averaging the intensity calculated from the two orthogonally polarized plane waves, the light polarization along a single ray (see Fig. 6.1) is eliminated leaving unpolarized light. The unpolarized light from each ray is then summed to produce the final image.

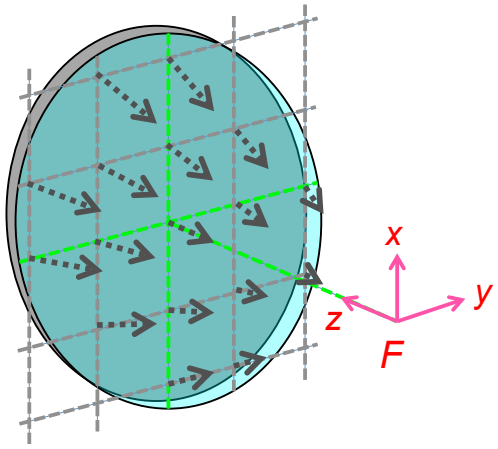

Figure 6.1: The condenser is sampled by a number of rays evenly spaced on a Cartesian coordinate system where each ray travels from the lens toward the focus, F. Each ray represents a pair of plane waves with orthogonal polarizations.

The superposition of unpolarized light provides the basis for a superposition Beer-Lambert law where each ray in Fig. 6.1 represents a single Beer-Lambert law calculation. The intensity calculated from each Beer-Lambert law is weighted by the same geometric optics theory used in the simulations. Based on this understanding, a superposition Beer-Lambert law is proposed for high NA, partially coherent illumination as:

$$I_f = I_o \iint_S \cos^{1/2}(\theta') \exp(-\alpha l(\theta', \varphi'))\, ds'_x\, ds'_y \tag{6.2}$$

where the function is integrated over the domain $S = \{(s_x, s_y) \in \mathbb{R}^2 \mid s_x^2 + s_y^2 \leq n \sin\theta_{max}\}$. The Cartesian coordinate variables of integration s'_x, s'_y, and s'_z are directly matched with their spherical coordinate counterparts where $\hat{\theta}' = \cos^{-1}(s'_z)$ and $\hat{\varphi}' = \text{atan2}(s'_y, s'_x)$. The maximum θ' is θ_{max}, which is the maximum angle of intersection with the optical axis as defined by the NA (NA$= n\sin(\theta_{max})$). The $\cos^{1/2}(\theta')$ factor is a result of the intensity law of geometric optics, dampening the

intensity of waves coming from the edge of the lens as compared to those propagating from the center of the lens [97]. The path length is now dependent on the direction of the ray.

The number of rays required to accurately sample the condenser is dictated by the sampling theorem such that there is no statistical correlation between two adjacent points on the sample plane. The so-called "mutual coherence function" [7] quantifies this correlation and provides a means to determine the appropriate anti-aliasing criteria. A closed form solution provided in Chapter 3 and [14] is replicated here:

$$\Delta s_x \leq \frac{2\pi f}{k \max\{D, W_c\}}, \ \Delta s_y \leq \frac{2\pi f}{k \max\{D, W_c\}} \tag{6.3}$$

where f is the frequency, D is the sample dimension, W_c is the value at which the mutual coherence function falls below a negligible value ($W_c = 1/(k \sin(\theta_{max})) = 1/(k_0 \mathrm{NA}_{illum})$), and the smallest wavelength in the excitation dictates the wavenumber for the anti-aliasing condition.

6.3 Methods

A 1.5 μm radius microsphere with a refractive index of $1.45 + j0.001$ (similar to that found in [68]) is situated in optical gel with a refractive index of 1.45 (similar to glycerol [75]). The microsphere is illuminated in a setup illustrated in Fig. 6.2 where the condenser NA ranges from 0.1 to 1.3 in increments of 0.4 and the illumination light is narrowband at 588nm. The light scattered by the microsphere is calculated on a plane situated one wavelength away from the edge of the microsphere and whose dimensions are 6 μm by 6 μm in increments of $\lambda/15$. The attenuation on the scat-

tering plane is calculated using Beer-Lambert, the superposition Beer-Lambert, and the partially coherent illumination theory [16]. In each of the Beer-Lambert law calculations, I_o is set to one, though the Beer-Lambert superposition and the partially coherent illumination results are normalized by:

$$\sum_j \left(\Delta s_x \Delta s_y \cos^{1/2}(\theta_n)\right)^2 \tag{6.4}$$

where j is the number of θs required by Δs_x, Δs_y, and the mutual coherence function. This normalization allows direct comparison with the original Beer-Lambert law results.

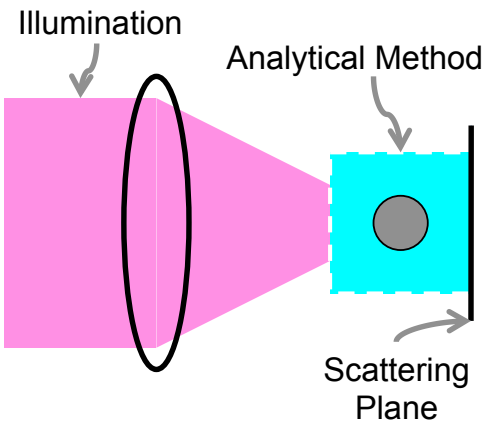

Figure 6.2: Simulation setup where a microsphere is illuminated by light focused by a condenser (not to scale). The illumination is described mathematically and the total intensity is calculated on the scattering plane using either the Beer-Lambert law or a variation of Mie theory.

The results from the proposed Beer-Lambert law formulation are directly compared to partially coherent illumination theory (described above) [16] albeit calculated using near-field Mie theory [108] instead of the FDTD method. The original

near-field Mie theory is only valid for x-polarized plane waves propagating in the z-direction where the $(\cos\phi\sin\theta, \cos\phi\cos\theta, -\sin\phi)$ vector is incorporated in Eqs. 33-35 in [108] to dictate the polarization. In addition to the x-polarized wave, the orthogonal y-polarized plane wave can be calculated using the same equations where the $(\sin\phi\sin\theta, \sin\phi\cos\theta, \cos\phi)$ polarization vector is used instead. Furthermore, the direction of both polarized waves can be rotated using a technique presented in Chapter 4 and [119]. Therefore, each ray in Fig. 6.1 specifies the direction for the two orthogonally polarized plane waves and the intensity calculated from the two plane waves is averaged to determine the intensity for that particular ray. The total image intensity is a summation of the intensity from all of the rays. The term Mie theory is used to describe partially coherent illumination for the remainder of this article.

6.4 Results and Discussion

The results from changing the condenser NA are shown in Fig. 6.3 for the original Beer-Lambert law, the proposed superposition Beer-Lambert law, and the Mie theory modeling. All three methods are accurate for illumination provided by the 0.1 and 0.5 NAs, but at a NA of 0.9, the Mie theory and superposition Beer-Lambert start to deviate from the original Beer-Lambert law. The resulting plots have less attenuation at the center as the light spreads out laterally. Fig. 6.4 shows the SSE between the two Beer-Lambert laws and Mie theory. The original Beer-Lambert law begins to accumulate error at 0.7 NA, which is exactly where the paraxial simplifications are no longer applicable and the same point where Fresnel and Fraunhofer diffraction are no longer valid [86]. At the 1.3 NA, the proposed Beer-Lambert law only results

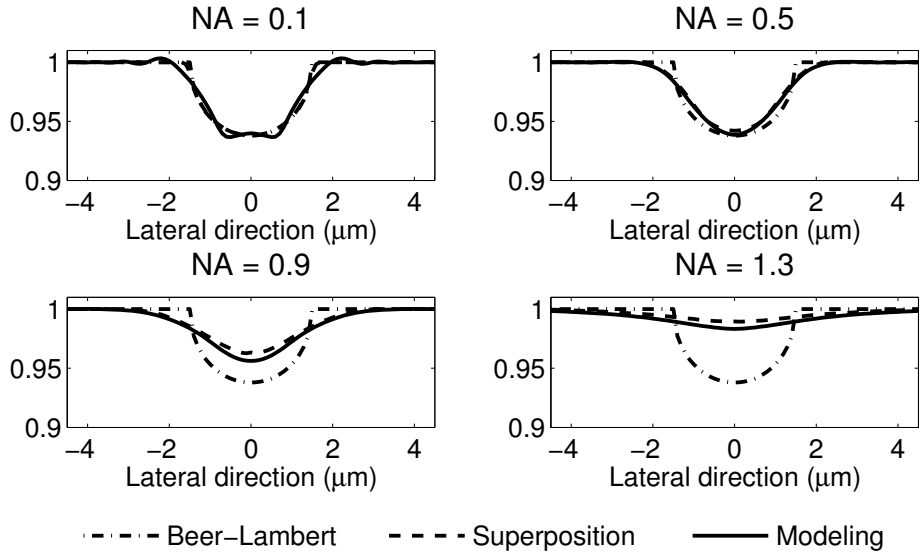

Figure 6.3: The attenuation through the microsphere is calculated using the original Beer-Lambert law, the proposed superposition Beer-Lambert law, and the Mie theory modeling. The results are plotted for NAs ranging from 0.1 to 1.3 in increments of 0.4.

in 5% of the error contained in the original Beer-Lambert results and the proposed Beer-Lambert law has less than 1% of the maximum error contained in the original formulation for all NAs less than 1.0.

The deviations between the proposed Beer-Lambert law and the Mie theory results (Fig. 6.3) are attributed to scattering. Fig. 6.5 shows the SSE between the two Beer-Lambert laws and the Mie theory as a function of microsphere extinction coefficient where the error exponentially increases as the extinction coefficient gets larger. While the microsphere and optical gel have the same real refractive component, the extinction coefficient still translates into some scattering in Mie theory that is ignored in Beer-Lambert. This understanding is validated by analyzing the extinction, scattering, and absorption efficiencies in standard single-wave Mie theory [90].

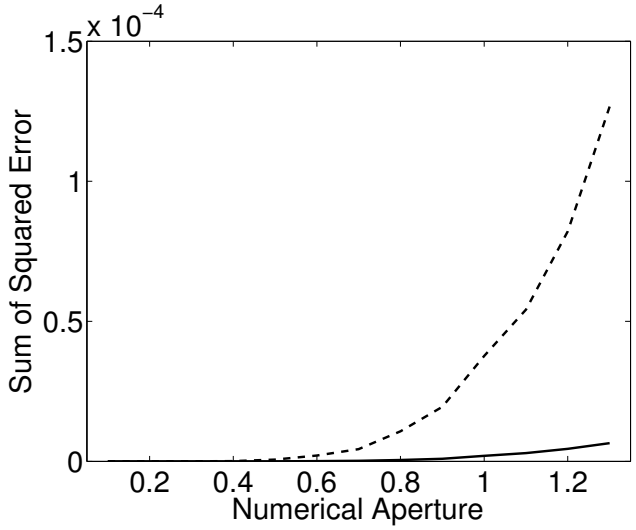

Figure 6.4: The SSE between the two Beer-Lambert laws and Mie theory are plotted for varying condenser NA ranging from 0.1 to 1.3 in increments of 0.1. The original Beer-Lambert SSE is plotted as a dashed line and the proposed Beer-Lambert SSE is plotted as a continuous line.

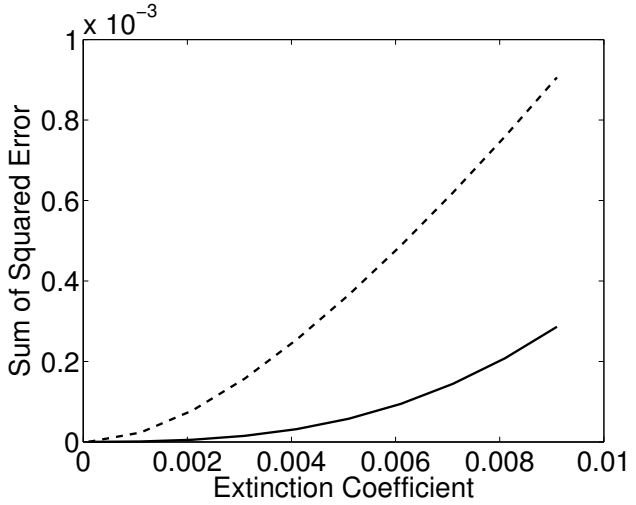

Figure 6.5: The SSE between the two Beer-Lambert laws and Mie theory are plotted for varying extinction coefficients where the NA is held at 0.9. The original Beer-Lambert SSE is plotted as a dashed line and the proposed Beer-Lambert SSE is plotted as a continuous line.

Fig. 6.6 shows the axial cross section through the microsphere as calculated using the original Beer-Lambert law and the proposed Beer-Lambert law where the microsphere is illuminated with a NA of 0.9. In the original Beer-Lambert, light travels from top to bottom and is slowly attenuated as it moves through the microsphere. The attenuation displays a parabolic nature along the lateral dimension due to the differences in path length (i.e. light doesn't go through very much of the microsphere near the $\pm 1.5 \mu m$ lateral dimensions, but goes through the full diameter at 0 μm). As soon as the light exits on the other side, the attenuation remains the exact same for infinity. The 0.9 NA illumination produces results similar to the original Beer-Lambert law near the top, but as light travels through more of the microsphere, the parabolic nature of the intensity is decreased. At the bottom edge of the microsphere, the light is focused, but the intensity starts to spread out at 3.0 μm.

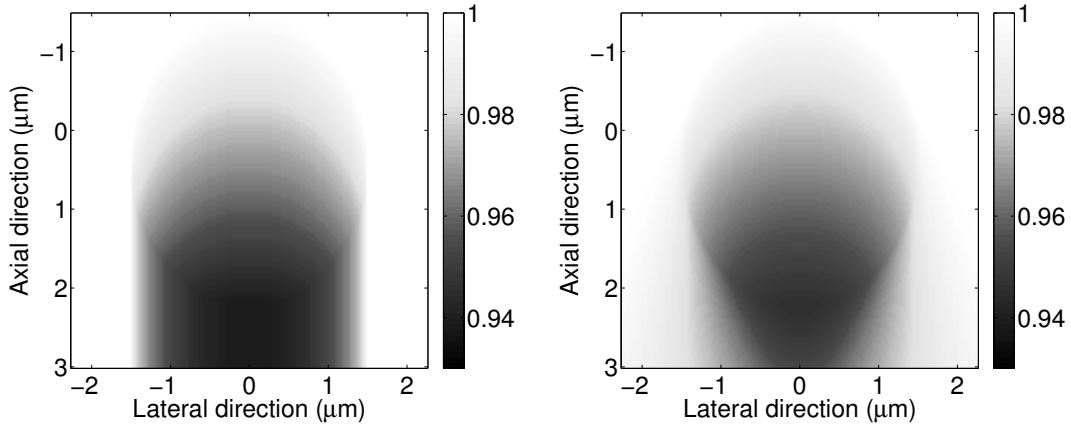

Figure 6.6: Axial cross section of the intensity drop through microsphere as determined by the original Beer-Lambert law (on the left) and the superposition Beer-Lambert law (on the right) illuminated with rays from a 0.9 NA condenser. The axial length of the plot is extended to 3 μm to show the light after exiting the microsphere.

6.5 Conclusion

The proposed Beer-Lambert law (Eq. 6.2) provides a fundamental improvement to understanding and predicting light attenuation in microspheres due to high NA illumination. Beyond microspheres, the new formulation could have an even greater impact in clinical cytology where pixel values could be directly related to cellular absorptive properties. Similar to the way scattering is currently employed to quantitatively detect cancer, this method could also quantitatively detect variations in absorption to diagnose cancer. The superposition Beer-Lambert law is compared to the theoretical Mie theory in order to eliminate potential experimental errors. Future experimental verification will require microspheres with calibrated absorptivity. The algorithm should also be applied to heterogeneous objects, such as cells, to better understand how organelles would affect these calculations. Organelles within the same cell have different real refractive indices, which would cause increased scattering and complicate conclusions drawn from this work. However, previous simulations of nucleus-like objects predict that high NA illumination would mitigate the effect of scattering since waves propagate from many angles [23]. If this hypothesis is incorrect, then scattering correction factors could be used to improve the results.

This work could also be used to re-design filtered backprojection for OPTM. As previously mentioned, filtered backprojection is based on parallel ray projections, which is not accurate for OPTM (see Fig. 6.6). This work could be used to design an alternative reconstruction algorithm that is more accurate for concentration measurements, such as chromatin, ultimately improving the sensitivity and specificity of cancer diagnosis in OPTM.

Chapter 7

FUTURE DIRECTIONS AND CONCLUSION

7.1 Future Directions

The computer model presented above can be used in many ways beyond those presented in this dissertation. For example, the model can be used to continue analyzing OPTM image formation, working towards the development of quantitative microscopy, and improving the reconstruction algorithm. There are also a number of ways single-cell OPTM can be improved, as well as, expanding the technique to analyze larger samples. In each case, this research provides the foundation for improved understanding and implementation of a clinically viable device.

7.1.1 Modeling

7.1.1.1 Analyzing OPTM

Tables 7.1, 7.2, and 7.3 highlight the possible effects that can be probed using this computer model where they are divided into three categories: sample, instrument, and reconstruction. The sample effects deal specifically with the position and contrast mechanisms of the object, while the instrument effects are due to potential problems with mechanical parts. The reconstruction effects are different than the sample and instrument effects in that rather than providing the ability to understand how the final image is affected by a particular effect, they allow for direct testing of potential

improvements. The research presented above only analyzes a subset of the sample and instrument effects and future work should be performed to analyze the remainder, in order to determine their overall effect on OPTM image formation.

Each of the models presented above provides a unique opportunity to analyze OPTM and bright-field microscopes in general. In almost every case, the FDTD model would be preferred due to its ability to analyze an arbitrary object like a cell or micro-shell. Micro-shells provided much greater insight in Chapter 3 than would have been gained by analyzing a microsphere. However, computational cost considerations often inhibit the use of the FDTD model and the Mie theory model provides adequate enough insight through microsphere analysis. These same thought processes should go into analyzing the remainder of the effects laid out in Tables 7.1-7.3. For example, analyzing the impact of scattering from multiple neighboring cells on the final reconstruction would require the use of the FDTD algorithm. Other effects, such as slow rotation and hysteresis of the micro-capillary, could be analyzed through the use of one of the models depending on the Cell-CT generation. For the first and second generation devices, these effects would be best analyzed using the Mie theory model because the fixed condenser focal plane would play a significant effect on the final analysis. For the third generation Cell-CT based on the moving condenser focal plane, these effects would be best analyzed using the FDTD algorithm since analysis could be performed using a micro-shell or an arbitrary object. Computational cost would be less of a concern in this last analysis.

Perhaps, a new model could be developed in the future that provides the same insight as the original FDTD algorithm with better computational cost. This new

model could calculate scattering from plane waves separately using the FDTD method and the Stratton-Chu diffraction integrals before subsequently combining the individual responses to form the total response. This technique would be very similar to the Mie theory model and allow other objects besides microspheres to be analyzed. The initial calculation of each plane wave would have a high computational cost, but the subsequent combination would be very low and allow experiments like the fixed condenser focal plane one to be performed using a micro-shell. This new experiment would probably provide even greater insight than the previous one. The computational cost of computer simulations could also be reduced by transferring the algorithms to Graphic Processing Units (GPUs), which have proven recently to provide super-computer-like reductions in processing time at lower computer costs. By parallelizing simulations among a large number of inexpensive GPUs, the processing time could be further reduced and allow more difficult simulations to be complete.

Table 7.1: Sample effects that could be probed using the computational models.

Contribution of refractive index in image contrast	Refractive index and absorption have important roles in determining the final reconstruction. Their roles are further enhanced by sample staining effects that could vary between samples.
Microsphere location	The microsphere rotates in the micro-capillary such that its axial position changes relative to the condenser focal plane.
Multiple cells	Multiple cells neighboring each other could impact the reconstructions where the illumination would be altered. This problem would be enhanced if the cells are in the same axial plane.
Arbitrary object	Cells with organelles will have a different scattering pattern compared to a microsphere, which could have an effect whether or not OPTM accurately predicts image formation.

Table 7.2: Instrument effects that could be probed using the computational models.

Micro-capillary wobble	Cells with organelles will have a different scattering pattern compared to a microsphere, which could have an effect whether or not OPTM accurately predicts image formation.
Moving condenser focal plane	Cells with organelles will have a different scattering pattern compared to a microsphere, which could have an effect whether or not OPTM accurately predicts image formation.
Axial scanning	The focal plane of the objective is scanned through the cell based on *a priori* information, but errors might occur such that the focal plane does not scan through the entire cell.
Slow rotation	As rotational speed of the micro-capillary is monitored the optical gel/cell mixture may not rotate at the same rate.
Micro-capillary hysteresis	The micro-capillary might experience hysteresis as it rotates causing non-smooth rotation; therefore, rotations could be acquired at unexpected locations.

In the future, after each of the sample and instrument effects are incorporated into the computational models, a complete sensitivity model of OPTM should be developed where distributions of errors are associated with each effect. From these distributions, a Monte Carlo method [78] could select random sets of imaging parameters to simulate reconstructions using the OPTM model. These reconstructions could be analyzed to build a sensitivity model of OPTM to understand the overall effect of each parameter on image formation while other parameters are also in flux. Building this type of sensitivity model would not only provide a complete understanding of the entire image formation process, but it would also propel OPTM towards quantitative microscopy where the effects can be statistically removed from the reconstructions.

Table 7.3: Reconstruction effects that will be probed using the computational models.

Parallel light approximation	The reconstruction technique utilizes the filtered back-projection based on parallel light propagation. This is has yet to be verified using high NA lenses.
Filter selection for reconstruction	If the filtered back-projection is the best method for reconstruction, then the filter should be optimized. This work utilizes the ramp filter, while VisionGate utilizes a slight variation of the ramp.
Deconvolution during axial scan	Rather than producing the projection images by optically integrating, equally spaced images could be acquired during scanning through the cell. These images could be individually deconvolved prior to summing them to produce a projection image.

The models also provide the opportunity to better investigate reconstruction effects that would otherwise be fairly difficult to implement experimentally. If the superposition Beer-Lambert law is incorrect experimentally and the parallel light approximation is applicable, then work could be performed to design the most appropriate filter for use in the filtered backprojection. The appropriate filter selection is often an important research and design question where there are generic filters such as Hanning and Hamming [92] and more specialized ones for specific applications. It is possible that one of these filters would provide a better opportunity to accurately reconstruct cellular images than the other.

Another idea is rather than optically integrating through the cell, OPTM could collect axial stacks that could be deconvolved prior to summation. Deconvolution of each image would potentially improve the resolution by mitigating the smearing effect of the PSF. This particular effect might be difficult to actually implement as deconvolution relies on Fourier modeling techniques that break down at high NA

[86]. Finally, the simulation of OPTM provides a means of evaluating independent factors that cannot be decoupled experimentally. By better understanding how these independent factors affect the entire process it should be possible to improve the overall diagnostic capabilities of OPTM that would otherwise be impossible using pure experimental processes.

7.1.1.2 Quantification using Beer-Lambert Law

One of the main advantages of this dissertation is the new formulation of the Beer-Lambert law for high NA microscopy. This particular discovery could have significant application in a large range of optical microscopy techniques, including standard bright-field microscopy used in the clinic everyday. While there are many problems that need to be overcome before quantitative microscopy is possible [131], the formulation of the superposition Beer-Lambert law provides a main pillar for this development. A future project should be performed to determine whether the law is accurate for potential clinical use.

Unfortunately, validation will be a very difficult assignment even using simple objects such as microspheres. Not only will standard experimental problems be difficult to overcome (e.g. noise), but readily available microspheres do not have the appropriate material properties. Microspheres are generally classified by their refractive indices with no appreciable absorption, which is not appropriate for Beer-Lambert law experiments. Custom-made microspheres composed of colored glass whose refractive index matches the surrounding media will need to be manufactured. Even after manufacturing the microspheres, it remains to be seen if the camera is able

to detect the absorption variations along a single plane and if diffraction from light collection through the objective will limit the accuracy of the results. While cells stained with absorptive dyes would be an easier experimental method, there would be no way to determine whether variations in intensity are a result of absorption or refractive index scattering. A simple object that can also be modeled using either the Mie theory or FDTD methods presented above would provide further validation between the experimental and simulation results. If the superposition Beer-Lambert law continues to show promise in these simple objects then it should be explored in cells.

7.1.1.3 Beer-Lambert Law based Reconstruction

The superposition Beer-Lambert law also could play a fundamental role in re-designing the OPTM reconstruction algorithm, which relies on the filtered backprojection method. As discussed previously, filtered backprojection assumes parallel ray projections where light travels in a single direction, entering the cell on the top of the cell and exiting on the bottom after being attenuated by the cellular absorption. The idea of parallel ray projections is illustrated by the original Beer-Lambert law results in the left plot of Fig. 6.6. If parallel rays were actually the case for high NA microscopy then the objective focal plane could sample the attenuated light for each rotation at a single position after exiting the cell. However, a number of rays propagate from different directions within the NA. The more accurate superposition Beer-Lambert law results are shown in the right plot of Fig. 6.6 where light propagates from different directions. In order to produce better reconstructions, a new reconstruction algorithm should be

designed taking into account the way light propagates from the high NA condenser.

The left illustration in Fig. 7.1 represents the standard filtered backprojection method where pixels are projected along a single axial direction based on the assumption that waves traveled in single direction with no scattering. The new Beer-Lambert law shows that pixel intensities are the result of waves propagating from every direction within the NA. An alternative reconstruction algorithm (right illustration in Fig. 7.1) could be designed such that pixels are backprojected as a right circular cone (in 3D space) whose radius is determined by the NA of the condenser illumination. In many ways this idea is almost the opposite of the standard cone-beam reconstruction technique used in modern CT scanners. This new method would eliminate the need to scan the objective focal plane. In fact, it would require that the objective focal plane not scan, which would improve throughput.

There are many points that would need to be considered before implementing this algorithm. For example, the algorithm would still require the location of the centroid of each cell for every position of rotation. Also, for ease of implementation, the objective focal plane would need to be at the exact same axial distance from the centroid for every rotation, so that the pixels from one rotation would align with pixels from another rotation. The algorithm would be computationally intensive compared to the current slice-by-slice reconstruction algorithm because the projections would be backprojected into 3D space. The algorithm would also require a substantially different, and probably more difficult, filtering technique because it would no longer be a simple 1D convolution. Filtering is used to account for the fact that low frequency information is over expressed in the projections compared to high frequency informa-

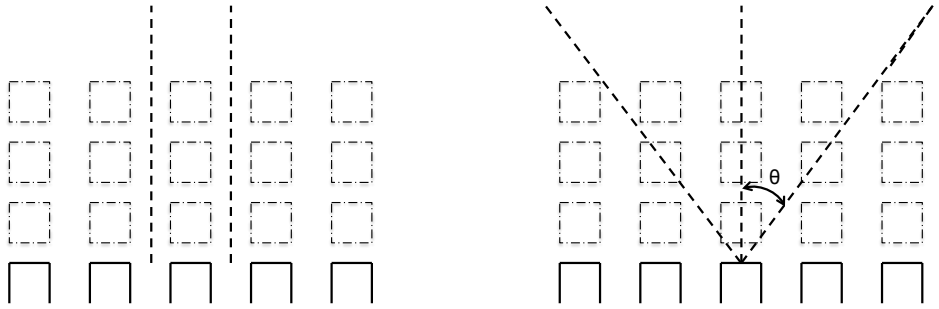

Figure 7.1: 2D illustrations of the standard backprojection method (left) and a potential new backprojection method based on the superposition Beer-Lambert law (right) for a single projection angle. The open squares at the bottom represent the pixels in the projections and the dashed grid of squares represents the reconstruction pixels. The value of the center projection pixel is backprojected to the reconstruction pixels within the long dotted lines for each method. The standard backprojection method projects the pixel value along a single line in the reconstruction whereas the new backprojection method would project the projection pixel value along a cone dependent on the maximum angle of light propagation (θ determined by the NA).

tion. Accounting for differences between low and high frequency information in the slice-by-slice reconstruction will be much more difficult in 3D cone reconstructions.

7.1.2 Future of OPTM

7.1.2.1 Single Cell Analysis

The Cell-CT continues to demonstrate promise in single cells analysis for the early detection and diagnosis of disease; however, there are a number of technological and scientific steps that must be overcome before it is a clinically viable device. Besides sensitivity and specificity, the major concern for deploying an early detection procedure on a large population is throughput. Studies have shown that early detection of

lung cancer could require imaging 1000 cells or more [80]. If analysis of each cell takes minutes, or even a few seconds, then the technique will not be fast enough to compete with other devices even if the sensitivity and specificity are that much better.

The first and second generation Cell-CTs took approximately one minute to acquire five hundred projections. Recent developments using remote scanning [24] have increased throughput by greater than thirty times. While this improvement is substantial, even greater improvements in throughput are probably necessary. One method to further improve throughput is with the use of hydrodynamic focusing to direct cells toward the center of the micro-capillary. This would improve throughput by eliminating the need to determine the trajectory of the cell centroid prior to projection acquisition and also would eliminate the need to continually move the objective to scan the cell. As discussed above, throughput could also be improved by designing a reconstruction algorithm that only requires a single intensity plane after the condenser light has passed all the way through the cell. While the actual reconstruction algorithm would be computationally more intensive, the principle rate-limiting step is projection acquisition as the reconstruction could be parallelized among many computer processors.

Other avenues to increase throughput include packing multiple cells in the camera field of view and/or looking at cells in a progression from 1D to 2D to 3D. At each step in the progression, an algorithm could determine whether it is worthwhile looking at the cell in a higher dimension. While there are a number of ways throughput could be improved, this continues to be a major detriment for clinical viability, especially when compared to Image and Flow cytometers. Those devices are capable of analyzing tens

of thousands [4] and hundreds of thousands of cells per second, respectively.

7.1.2.2 Core Biopsy Analysis

A new direction for OPTM is analysis of fine needle core biopsies [105]. Standard biopsy procedures collect superficial cells from a potential mass in a hollow needle. The cells are then ejected from the needle and spread out on a slide before being fixed, stained, and viewed by a pathologist on a microscope. Based on the individual cell structure, the pathologist determines whether abnormalities associated with cancer or disease is present. The main problem with this procedure is caused by spreading the cells on a slide, thereby eliminating potential morphological analysis that could provide additional information about the location and extent of the disease. The invasiveness of cancer can also be determined from tissue biopsy rather than cell biopsy, which affects the treatment of the patient. Rather than spread the cells on a slide, our group is working on a method to collect cells in the hollow needle, then fix, stain, and image the biopsy as a 3D core where clinicians will be able to analyze the resulting images for both intracellular and extracellular abnormalities.

As with single-cell analysis, there are a number of scientific and technical problems that need to be overcome before this method is clinically viable. Scientifically, the main problem with large specimen is scattering where light waves do not produce images representative of the tissue structure. This problem is the reason light is often not used diagnostically for any application beyond a millimeter. One of the main ways to circumvent the scattering problem is the use of an optical clearing agent. The clearing agent is designed to have a refractive index similar to the cell membrane

and is used to replace the tissue fluid. As the refractive index mismatch is diminished, the scattering in the tissue is reduced.

One of the main technical problems is producing a reliable means to extract the tissue from the biopsy needle, fixing and stain it, and then applying the clearing agent before getting the tissue into the microcapillary. There are a number of ongoing studies to determine the best way to perform this procedure. Another technical problem is related to the size of the specimen, where the core height is often 2-3 mm long. At the same time, the field of view for a 100× Olympus objective is only 81 μm in its longest dimension, so multiple frames must be collected and stitched together in order to produce a single core biopsy image [18]. Despite these technical problems, core biopsy analysis could be the future of OPTM. Most of the throughput problems in the single cell analysis OPTM would not be relevant for core biopsies where analysis of a 3 mm core would require approximately 38 frames with a 100× objective.

7.2 Conclusions

This dissertation outlines a computer simulation algorithm and corresponding experiments to examine OPTM image formation in a robust methodology. The computer simulations of OPTM will allow the Cell-CT to have higher sensitivity and specificity for cancer diagnoses than would have otherwise been possible. Without the simulations, it would have been nearly impossible to quickly and inexpensively test various imaging parameters or understand how cell optical properties affect the final reconstruction. Experiments also played an important role by providing a means to refine simulation hypotheses, thereby providing a more complete understanding. The

results of this work are providing quantitative conclusions that are driving improved implementation of OPTM in the Cell-CT. This work is also applicable outside of OPTM where the model could be used to simulate all bright-field microscopy. Using the simulation could provide a means to determine the best device parameters, as well as, better understanding of biological absorption and scattering from both cancerous and non-cancerous specimen.

Due to increases in computing power and theoretical understanding of microscopes, this dissertation provides a concrete example of improving microscope design through both experimental methods and simulations. Not only do simulations provide improved understanding, but they also provide a means to develop devices in a more expedient and efficient manner. This evolution in design, incorporating both simulations and experiments, should be utilized by other groups and companies as they develop novel microscopes in the future.

The theoretical understanding provided by this work also led to the development of the high NA illumination Beer-Lambert law, which could have the greatest impact of this dissertation due to its universal application to optical microscopy. In the future, optical microscopes will develop quantitative ways to relate the image pixel values back to organelle absorption and scattering processes. The development of these quantitative scales will provide significant advancements in disease detection and diagnosis.

Beyond the microscope simulation, the key benefit of OPTM is the reconstruction of submicron, isometric images of cellular and chromatin structure using a complete range of contrast agents. Isometric, 3D resolution represents the cells comprehen-

sively, providing the clinician with complete freedom to select the ideal cutting plane that affords the greatest diagnostic value. Furthermore, the 3D features measured within the volumetric image for disease classifications and computer-aided diagnoses are more sensitive and robust when there is no dependence on 2D slice-selection and orientation biases. Classifiers based on current absorption-based morphological features, rival the diagnostic ability of a highly trained cyto-technologist or pathologist. These features will no doubt find augmentations as 3D quantitation improves and fluorescence based indications are added, opening a host of new applications.

Questions arise as to how new tools and understanding from the research community will be integrated into clinical diagnosis, especially early cancer diagnosis. For example, nanoscale scattering signatures of cells can be measured and correlated to feature sizes below that of conventional optical microscopes, while accurately diagnosing cancer [2, 112, 126, 69]. The nanoscale can now be reached with new super-resolution optical microscopes that rely on fluorescence [44, 47, 53]. However, a major impediment to translation into clinical pathology is lack of communication between the two communities of researchers and clinicians [36, 123]. OPTM is expected to play a role in the many steps in this translation process. The first step is to help move conventional cytology and pathology from reliance on 2D images to visualizing and quantifying features using 3D volumetric images [81]. A second step is the development of high-throughput, quantitative cell imaging and multimodal analysis platforms based on OPTM. Since the human observer is expected to be the rate-limiting step in making a diagnosis from a 3D multimodal image, the next step in translation is to fully automate diagnostic OPTM systems. The work presented

above provides the means by which to analyze OPTM and improve its overall clinical implementation for the purpose of providing early lung cancer diagnoses with high sensitivity and specificity.

BIBLIOGRAPHY

[1] D. R. Aberle, A. M. Adams, C. D. Berg, W. C. Black, J. D. Clapp, R. M. Fagerstrom, I. F. Gareen, C. Gatsonis, P. M. Marcus, and J. D. Sicks. Reduced lung-cancer mortality with low-dose computed tomographic screening. *New Engl. J. Med.*, 365:395–409, 2011.

[2] N. Anderson, J. Houghton, S. J. Kirk, D. Frank, J. Ranger-Moore, D. S. Alberts, D. Thompson, and P. H. Bartels. Malignancy-associated changes in lactiferous duct epithelium. *Anal. Quant. Cytol. Histol.*, 25:63–72, 2003.

[3] J. P. A. Baak. *Manual of Quantitative Pathology in Cancer Diagnosis and Prognosis*, 1991.

[4] D. A. Basiji, W. E. Ortyn, L. Liang, V. Venkatachalam, and P. Morrissey. Cellular image analysis and imaging by flow cytometry. *Clin. Lab. Med.*, 27:653, 2007.

[5] J. P. Berenger. A perfectly matched layer for the absorption of electromagnetic waves. *J. Comput. Phys.*, 114:185–200, 1994.

[6] A. Böcking. Cytological vs histological evaluation of percutaneous biopsies. *Cardiovasc. Inter. Rad.*, 14:5–12, 1991.

[7] M. Born and E. Wolf. *Principles of optics: electromagnetic theory of propagation, interference and diffraction of light.* Pergamon Press, 1980.

[8] E.J. Botcherby, R. Juškaitis, M.J. Booth, and T. Wilson. Aberration-free optical refocusing in high numerical aperture microscopy. *Opt. Lett.*, 32:2007–2009, 2007.

[9] N. N. Boustany, S. A. Boppart, and V. Backman. Microscopic imaging and spectroscopy with scattered light. *Annu. Rev. Biomed. Eng.*, 12:285–314, 2010.

[10] J. Bradl, B. Rinke, B. Schneider, P. Edelmann, H. Krieger, M. Hausmann, and C. Cremer. Resolution improvement in 3d microscopy by object tilting. *Microsc. Anal.*, 44:9–11, 1996.

[11] J. P. Brody and S. R. Quake. A self-assembled microlensing rotational probe. *Appl. Phys. Lett.*, 74:144–146, 1999.

[12] A. Brunstin and P. F. Mullaney. Differential light-scattering from spherical mammalian-cells. *Biophys. J.*, 14(6):439–453, 1974.

[13] E.J. Candes, J. Romberg, and T. Tao. Robust uncertainty principles: exact signal reconstruction from highly incomplete frequency information. *IEEE T. Inform. Theory*, 52:489–509, 2006.

[14] I. R. Çapoglu, J. D. Rogers, A. Taflove, and V. Backman. The microscope in a computer: Image synthesis from three-dimensional full-vector solutions of maxwell's equations at the nanometer scale. *Prog. Optics*, 57, 2012.

[15] I. R. Çapoglu, A. Taflove, and V. Backman. Generation of an incident focused light pulse in fdtd. *Opt. Express*, 16(23):19208–19220, 2008.

[16] I. R. Çapoglu, C. A. White, J. D. Rogers, H. Subramanian, A. Taflove, and V. Backman. Numerical simulation of partially coherent broadband optical imaging using the finite-difference time-domain method. *Opt. Lett.*, 36:1596–1598, 2011.

[17] W. Choi, C. Fang-Yen, K. Badizadegan, S. Oh, N. Lue, R. R. Dasari, and M. S. Feld. Tomographic phase microscopy. *Nat. Methods*, 4:717–719, 2007.

[18] K.F. Chou, Q. Miao, R.L. Coe, and E.J. Seibel. 3d imaging of fine needle aspirates using optical projection tomographic microscopy. *J. Cytol. Histol.*, S2:001, 2013.

[19] T. H. Chow, W. M. Lee, K. M. Tan, B. K. Ng, and C. J. R. Sheppard. Resolving interparticle position and optical forces along the axial direction using optical coherence gating. *Appl. Phys. Lett.*, 97:231113, 2010.

[20] H. R. Chuang and L. C. Kuo. 3d fdtd design analysis of a 2.4-ghz polarization-diversity printed dipole antenna with integrated balun and polarization-switching circuit for wlan and wireless communication applications. *IEEE T. Microw. Theory*, 51:374–381, 2003.

[21] R. L. Coe, Q. Miao, K. F. Chou, M. G. Meyer, and E. J. Seibel. *Advanced Biophotonics: Tissue Optical Sectioning*, chapter Isometric 3D Imaging of Cellular Samples Using Optical Projection Tomographic Microscopy. Taylor & Francis, 2013.

[22] R. L. Coe and E. J. Seibel. Improved near-field calculations using vectorial diffraction integrals in the finite-difference time-domain method. *J. Opt. Soc. Am. A*, 28:1776–1783, 2011.

[23] R. L. Coe and E. J. Seibel. Computational modeling of optical projection tomographic microscopy using the finite difference time domain method. *J. Opt. Soc. Am. A*, 29(12):2696–2707, 2012.

[24] R. L. Coe and E. J. Seibel. Experimental and theoretical analysis for improved microscope design of optical projection tomographic microscopy. *Opt. Lett.*, submitted for publication, 2013.

[25] R.L. Coe and E.J. Seibel. Modeling microsphere axial displacement in optical projection tomographic microscopy to analyze effects on filtered backprojection reconstruction. In *Biomedical Applications of Light Scattering VII*, volume 85920G, San Francisco, CA, 2013. SPIE Photonics West.

[26] A. Deepak and M. A. Box. Forward corrections for optical extinction measurements in aeresol media. 2: Polydispersions. *Appl. Optics*, 17:3169–3176, 1978.

[27] A. Deepak and M. A. Box. Forward scattering corrections for optical extinction measurements in aerosol media. 1: Monodispersions. *Appl. Optics*, 17:2900–2908, 1978.

[28] D. T. Delpy, M. Cope, P. van der Zee, S. Arridge, S. Wray, and J. Wyatt. Estimation of optical path length through tissue from direct time of flight measurements. *Phys. Med. Biol.*, 33:1433–1442, 1988.

[29] V. P. Dick. Applicability limits of beer's law for dispersion media with a high concentration of particles. *Appl. Optics*, 37:4998–5004, 1998.

[30] H.-U. Dodt and K. Becker. Confocal microscopy in transmitted light. *Confocal, Multiphoton, and Nonlinear Microscopic Imaging*, 2003.

[31] R. Drezek, A. Dunn, and R. Richards-Kortum. Light scattering from cells: finite-difference time-domain simulations and goniometric measurements. *Appl. Opt.*, 38:3651–3661, 1999.

[32] R. Drezek, A. Dunn, and R. Richards-Kortum. A pulsed finite-difference time-domain (fdtd) method for calculating light scattering from biological cells over broad wavelength ranges. *Opt. Exp.*, 6:147–157, 2000.

[33] R. Erni, M. D. Rossell, C. Kisielowski, and U. Dahmen. Atomic-resolution imaging with a sub-50-pm electron probe. *Phys. Rev. Lett.*, 102(9):096101, 2009.

[34] J. Y. Fang and D. W. Xeu. Numerical errors in the computation of impedances by fdtd method and ways to eliminate them. *IEEE Microw. Guided W.*, 5:6–8, 1995.

[35] M. Fauver, E. J. Seibel, J. R. Rahn, M. G. Meyer, F. W. Patten, T. Neumann, and A. C. Nelson. Three-dimensional imaging of single isolated cell nuclei using optical projection tomography. *Opt. Exp.*, 13:4210–4223, 2005.

[36] D. Zink A. H. Fischer and J. A. Nickerson. Nuclear structure in cancer cells. *Nat. Rev. Cancer*, 4:677–687, 2004.

[37] K. Fuwa and B. L. Vallee. The physical basis of analytical atomic absorption spectrometry. *Anal. Chem.*, 35:942–946, 1963.

[38] S. J. Jang J. M. Gardner and J. Y. Ro. Diagnostic approach and prognostic factors of cancers. *Adv. Anat. Pathol.*, 18:165–172, 2011.

[39] Y. Garini, B. J. Vermolen, and I. T. Young. From micro to nano: recent advances in high-resolution microscopy. In *Curr. Opin. Biotech.*, volume 16, pages 3–12, 2005.

[40] G. Gouesbet. Generalized lorenz-mie theory and applications. *Part. Part. Syst. Char.*, 110:22–34, 1994.

[41] G. Gouesbet and L. Mees. Generalized lorenzmie theory for infinitely long elliptical cylinders. *J. Opt. Soc. Am. A*, 16(6):1333–1341, 1999.

[42] C. Guiffaut and K. Mahdjoubi. Perfect wideband plane wave injector for fdtd method. *in Proc. IEEE Antennas Propagation Soc. Intl. Symp.*, pages 236–239, 2000.

[43] M. G. L. Gustafsson. Surpassing the lateral resolution limit by a factor of two using structured illumination microscopy. *J. Microsc-Oxford*, 198:82–87, 2000.

[44] B. Hein, K. I. Willig, and S. W. Hell. Stimulated emission depletion (sted) nanoscopy of a fluorescent protein-labeled organelle inside a living cell. *Proc. Nat. Acad. Sci.*, 105:14271–14276, 2008.

[45] F. F. Hirsch, D. T. Merrick, and W. A. Franklin. Role of biomarkers for early detection of lung cancer and chemoprevention. *Eur. Respir. J.*, 19:1151–1158, 2002.

[46] G. N. Hounsfield. Computed medical imaging. *Science*, 210:22–28, 1980.

[47] B. Huang, W. Wang, M. Bates, and X. Zhuang. Three-dimensional super-resolution imaging by stochastic optical reconstruction microscopy. *Science*, 319:810–813, 2008.

[48] D. C. Ihde. Chemotherapy of lung cancer. *New Engl. J. Med.*, 327:1434–1441, 1992.

[49] A. Ishimaru. *Electromagnetic wave propagation, radiation, and scattering*. Prentice Hall, Englewood Cliffs, N.J., 1991.

[50] S. Jaffer and I. J. Bleiweiss. Beyond hematoxylin and eosinthe role of immunohistochemistry in surgical pathology. *Cancer Invest.*, 22:445–465, 2004.

[51] A. Jemal, K. C. Chu, and R. E. Tarone. Recent trends in lung cancer mortality in the united states. *J. Natl. Cancer I.*, 93:277–283, 2001.

[52] N. Johnson, M. Krebs, R. Boudreau, G. Giorgi, M. LeGros, and C. Larabell. Actin-filled nuclear invaginations indicate degree of cell de-differentiation. *Differentiation*, 71:414–424, 2003.

[53] M. F. Juette, T. J. Gould, M. D. Lessard, M. J. Mlodzianoski, B. S. Nagpure, B. T. Bennett, S. T. Hess, and J. Bewersdorf. Three-dimensional sub-100 nm resolution fluorescence microscopy of thick samples. *Nat. Methods*, 5:527–529, 2008.

[54] A. C. Kak and M. Slaney. *Principles of computerized tomographic imaging*. IEEE Press, New York, 1988.

[55] A. C. Kak and M. Slaney. *Principles of computerized tomographic imaging*. Society for Industrial and Applied Mathematics, Philadelphia, PA, 1988.

[56] S. Kawata and S. Minami. The principle and applications of optical microscope tomography. *Acta Histochem. Cytoc.*, 19:73–81, 1986.

[57] S. Kawata, O. Nakamura, and S. Minami. Optical microscope tomography. i. support constraint. *J. Opt. Soc. Am. A*, 4:292–297, 1987.

[58] S. Kikuchi, K. Sonobe, and N. Ohyama. Three-dimensional microscopic computed tomography based on generalized radon transform for optical imaging systems. *Opt. Commun.*, 123:725–733, 1996.

[59] S. Kikuchi, K. Sonobe, L. S. Sidharta, and N. Ohyama. Three-dimensional computed tomography for optical microscopes. *Opt. Commun.*, 107:432–444, 1994.

[60] Y. L. Kim, Y. Liu, R. K. Wali, H. K. Roy, M. J. Goldberg, A. K. Kromin, K. Chen, and V. Backman. Simultaneous measurement of angular and spectral properties of light scattering for characterization of tissue microarchitecture and its alteration in early precancer. *IEEE J. Sel. Top. Quant.*, 9:243–256, 2003.

[61] C. D. Kuglin and D. C. Hines. The phase correlation image alignment method. *Proc. of IEEE Int. Conf. Systems, Man and Cybernetics*, pages 163–165, 1975.

[62] V. Kumar and S. L. Robbins. *Robbins basic pathology*. Saunders/Elsevier, 2007.

[63] P. Latimer. Experimental tests of theoretical method for predicting light scattering by aggregates. *Appl. Optics*, 24:3231–3239, 1985.

[64] V. Lauer. New approach to optical diffraction tomography yielding a vector equation of diffraction tomography and a novel tomographic microscope. *J. Microsc-Oxford*, 205:165–176, 2002.

[65] X. Li, A. Taflove, and V. Backman. Modified fdtd near-to-far-field transformation for improved backscattering calculation of strongly forward-scattering objects. *IEEE Antenn Wirel Pr*, 4:35–38, 2005.

[66] B. M. Ljung. *Koss' Diagnostic Cytology and its Histopathologic Bases*, chapter Techniques of fine-needle aspiration, smear preparation, and principles of interpretation, pages 1056–1080. Lippincott Williams & Wilkins, 2006.

[67] R. J. Luebbers, K. S. Kunz, M. Schneider, and F. Hunsberger. A finite-difference time-domain near zone to far zone transformation. *IEEE T Antenn Propag*, 39:429–433, 1991.

[68] X. Ma, J. Q. Lu, R. S. Brock, K. M. Jacobs, P. Yang, and X.-H. Hu. Determination of complex refractive index of polystyrene microspheres from 370 to 1610 nm. *Phys. Med. Biol.*, 48:4165–4172, 2003.

[69] C. MacAulay, S. Lam, P. W. Payne, J. C. LeRiche, and B. Palcic. Malignancy-associated changes in bronchial epithelial cells in biopsy specimens. *Anal. Quant. Cytol. Histol.*, 17:55–61, 1995.

[70] N. Ikeda C. MacAulay, S. Lam, J. LeRiche, P. Payne, D. Garner, C. Konaka, H. Kato, and B. Palcic. Malignancy associated changes in bronchial epithelial cells and clinical application as a biomarker. *Lung Cancer*, 19:161–166, 1998.

[71] T. Martin. An improved near- to far-zone transformation for the finite-difference time-domain method. *IEEE T. Antenn. Propag.*, 46:1263–1271, 1998.

[72] T. Martin. On the fdtd near-to-far-field transformations for weakly scattering objects. *IEEE T. Antenn. Propag.*, 58:2794–2795, 2010.

[73] T. Martin and L. Pettersson. Dispersion compensation for huygens' sources and far-zone transformation in fdtd. *IEEE T. Antenn. Propag.*, 48:494–501, 2000.

[74] N. Martini, J. Bewersdorf, and S. W. Hell. A new high-aperture glycerol immersion objective lens and its application to 3d-fluorescence microscopy. *J. Microsc-Oxford*, 206:146–151, 2002.

[75] N. Martini, J. Bewersdorf, and S. W. Hell. A new high-aperture glycerol immersion objective lens and its application to 3d-fluorescence microscopy. *J. Microsc-Oxford*, 206(Pt. 2):146–151, 2002.

[76] J. O. D. McGee, P. G. Isaacson, and N. A. Wright. *Oxford textbook of pathology.* Oxford University Press, 1992.

[77] D. Merewether, R. Fisher, and F. W. Smith. On implementing a numeric huygen's source scheme in a finite difference program to illuminate scattering bodies. *IEEE T. Nucl. Sci.*, 27:1829–1833, 1980.

[78] N. Metropolis and S. Ulam. The monte carlo method. *J. Am. Stat. Assoc.*, 44:335–341, 1949.

[79] M. G. Meyer, M. Fauver, J. R. Rahn, T. Neumann, and F. W. Patten. Automated cell analysis in 2d and 3d: A comparative study. *Pattern Recogn.*, 42:141–146, 2009.

[80] M. G. Meyer, F. W. Patten, T. Neumann, J. W. Hayenga, D. E. Steinhauer, J. R. Rahn, and A. C. Nelson. The lung cell evaluation device (luced): Early detection of lung cancer in sputum based on 3d morphology. In J. R. Jett, editor, *13th World Conference On Lung Cancer*, page S378, San Francisco, 2009.

[81] Q. Miao, A. P. Reeves, F. W. Patten, and E. J. Seibel. Multimodal 3d imaging of cells and tissue: Bridging the gap between clinical and research microscopy. *Ann. Biomed. Eng.*, 40:263–276, 2012.

[82] G. Mie. Articles on the optical characteristics of turbid tubes, especially colloidal metal solutions. *Ann Phys-Berlin*, 25:377–445, 1908.

[83] M. Minsky. *Microscopy Apparatus*. U.S. Patent Number 3 013 467, 1957.

[84] C. F. Mountain. Revisions in the international system for staging lung cancer. *Chest*, 111:1710–1717, 1997.

[85] P. R. T. Munro and P. Török. Calculation of the image of an arbitrary vectorial electromagnetic field. *Opt. Exp.*, 15(15):9293–9307, 2007.

[86] N. Nakajima. Phase retrieval from a high-numerical-aperture intensity distribution by use of an aperture-array filter. *J. Opt. Soc. Am. A*, 26:2172–2180, 2009.

[87] O. Nakamura, S. Kawata, and S. Minami. Optical microscopye tomography. ii. nonnegative constraint by a gradient-projection method. *J. Opt. Soc. Am. A*, 5:554–561, 1988.

[88] T. Neumann, M. G. Meyer, F. W. Patten, F. L. Johnson, Y. S. Erozan, W. J. Frable, P. K. Gupta, M. B. Zaman, and A. C. Nelson. Premalignant and malignant cells in sputum from lung cancer patients. *Cancer Cytopathol.*, 117:473–481, 2009.

[89] T. Neumann, Q. Miao, J. Yu, M. Fauver, M. Meyer, J. R. Rahn, C. A. Lancaster, E. J. Seibel, and A. C. Nelson. Simultaneous 3d imaging of morphology and nanoparticle distribution in single cells with the cell-ct technology. In *Engineering in Medicine and Biology Society, 2008*, 2008.

[90] H.M. Nussenzveig and W.J. Wiscombe. Efficiency factors in mie scattering. *Phys. Rev. Lett.*, 45(18):1490–1494, 1980.

[91] M. Oheim. High-throughput microscopy must re-invent the microscope rather than speed up its functions. *Brit. J. Pharmacol.*, 152:1–4, 2007.

[92] A. V. Oppenheim, R. W. Schafer, and J. R. Buck. *Discrete-Time Signal Processing*. Prentice-Hall, 2nd edition, 1999.

[93] C. W. Penney and R. J. Luebbers. Input impedance, radiation-pattern, and radar cross-section of spiral antennas using fdtd. *IEEE T. Antenn. Propag.*, 42:1328–1332, 1994.

[94] T. L. Petty. The early identification of lung carcinoma by sputum cytology. *Cancer*, 89:2461–2464, 2000.

[95] J. Pyhtila, R. Graf, and A. Wax. Determining nuclear morphology using an improved angle-resolved low coherence interferometry system. *Opt. Exp.*, 11(25):3473–3484, 2003.

[96] O. M. Ramahi. Near- and far-field calculations in fdtd simulations using kirchhoff surface integral representation. *IEEE T. Antenn. Propag.*, 45:753–759, 1997.

[97] B. Richards and E. Wolf. Electromagnetic diffraction in optical systems. ii. structure of the image field in an aplanatic system. *Proc. R. Soc. A*, 253:358–379, 1959.

[98] B. Richards and E. Wolf. Electromagnetic diffraction in optical systems. ii. structure of the image field in an aplanatic system. *Proc. R. Soc. A*, 253(1274):358–379, 1959.

[99] D. J. Robinson and J. B. Schneider. On the use of the geometric mean in fdtd near-to-far-field transformations. *IEEE T. Antenn. Propag.*, 55:3204–3211, 2007.

[100] J. A. Roden and S. D. Gedney. Convolution pml (cpml): An efficient fdtd implementation of the cfspml for arbitrary media. *Microw. Opt. Techn. Let.*, 27:334–339, 2000.

[101] P. J. Sands. Modelling canopy production. ii. from single-leaf photosynthetic parameters to daily canopy photosynthesis. *Aust. J. Plant Physiol.*, 22:603–614, 1995.

[102] A. Sassaroli and S. Fantini. Comment on the modified beer-lambert law for scattering media. *Phys. Med. Biol.*, 49:N255–N257, 2004.

[103] J. B. Schneider and K. Abdijalilov. Analytic field propagation tfsf boundary for fdtd problems involving planar interfaces: Pecs, te, and tm. *IEEE T. Antenn. Propag.*, 54:2531–2542, 2006.

[104] J. J. Schwartz, S. Stavrakis, and S. R. Quake. Colloidal lenses allow high-temperature single-molecule imaging and improve fluorophore photostability. *Nat. Nanotechnol.*, 5:127, 2009.

[105] E. J. Seibel, Q. Miao, R. L. Coe, P. G. Reinhall, and D. W. Storti. *Optical Projection Tomography Microscope (OPTM) for large specimen sizes.* U.S. Patent Number 13 091 088, submitted Apr. 20, 2011.

[106] P. J. Shaw, D. A. Agard, Y. Hiraoka, and J. W. Sedat. Tilted view reconstruction in optical microscopy. three-dimensional reconstruction of drosophila melanogaster embryo nuclei. *Biophys. J.*, 55:101–110, 1989.

[107] F. Slimani, G. Grehan, G. Gouesbet, and D. Allano. Near-field lorenz-mie theory and its application to microholography. *Appl. Opt.*, 23:4140–4148, 1984.

[108] F. Slimani, G. Grehan, G. Gouesbet, and D. Allano. Near-field lorenz-mie theory and its application to microholography. *Appl. Opt.*, 23(22):4140–4148, 1984.

[109] C. Smithpeter, A. K. Dunn, R. Drezek, T. Collier, and R. Richards-Kortum. Near real time confocal microscopy of cultured amelanotic cells: Sources of signal, contrast agents and limits of contrast. *J. Biomed. Opt.*, 3:429–436, 1998.

[110] V. Starkuviene and R. Pepperkok. The potential of high-content high-throughput microscopy in drug discovery. *Brit. J. Pharmacol.*, 152:62–71, 2007.

[111] E. H. Stelzer and S. Lindek. Fundamental reduction of the observation volume in far-field light microscopy by detection orthogonal to the illumination axis: confocal theta microscopy. *Opt. Commun.*, 111:536–547, 1994.

[112] H. Subramanian, P. Pradhan, Y. Liu, I. R. Capoglu, J. D. Rogers, H. K. Roy, R. E. Brand, and V. Backman. Partial-wave microscopic spectroscopy detects subwavelength refractive index fluctuations: an application to cancer diagnosis. *Opt. Lett.*, 34:518–520, 2009.

[113] H. Subramanian, H. K. Roy, P. Pradhan, M. J. Goldberg, J. Muldoon, R. E. Brand, C. Sturgis, T. Hensing, D. Ray, A. Bogojevic, J. Mohammed, J. Chang, and V. Backman. Nanoscale cellular changes in field carcinogenesis detected by partial wave spectroscopy. *Cancer Research*, 69:5357, 2009.

[114] Y. Sung, W. Choi, C. Fang-Yen, K. Badizadegan, R. R. Dasari, and M. S. Feld. Optical diffraction tomography for high resolution live cell imaging. *Opt. Exp.*, 17:266–277, 2009.

[115] A. Taflove and S. C. Hagness. *Computational electrodynamics: the finite-difference time-domain method*. Artech House, 2005.

[116] A. Taflove and K. Umashankar. Radar cross-section of general 3-dimensional scatterers. *IEEE T. Electromagn. C.*, 25:433–440, 1982.

[117] M. J. Thun, L. M. Hannan, L. L. Adams-Campbell, P. Boffetta, J. E. Buring, D. Feskanich, W. D. Flanders, S. H. Jee, K. Katanoda, L. N. Kolonel, I. M. Lee, T. Marugame, J. R. Palmer, E. Riboli, T. Sobue, E. Avila-Tang, L. R. Wilkens, and J. M. Samet. Lung cancer occurrence in never-smokers: an analysis of 13 cohorts and 22 cancer registry studies. *PLoS Med.*, 5:e185, 2008.

[118] O. B. Toon and T. P. Ackerman. Algorithms for the calculation of scattering by stratified spheres. *Appl. Opt.*, 20(20):3657–3660, 1981.

[119] P. Török, P. D. Higdon, R. Juskaitis, and T. Wilson. Optimising the image contrast of conventional and confocal optical microscopes imaging finite sized spherical gold scatterers. *Opt. Commun.*, 155:335–341, 1998.

[120] P. Török, P. R. T. Munro, and E. E. Kriezis. Rigorous near- to far-field transformation for vectorial diffraction calculations and its numerical implementation. *J. Opt. Soc. Am. A*, 23(3):713–722, 2006.

[121] P. Török, P. R. T. Munro, and E. E. Kriezis. High numerical aperture vectorial imaging in coherent optical microscopes. *Opt. Exp.*, 16(2):507–523, 2008.

[122] M. Totzeck. Numerical simulation of high-NA quantitative polarization microscopy and corresponding near-fields. *Optik*, 112:399–406, 2001.

[123] L. D. True and C. D. Jordan. The cancer nuclear microenvironment: Interface between light microscopic cytology and molecular phenotype. *J. Cell. Biochem.*, 104:1994–2003, 2008.

[124] K. Umashankar and A. Taflove. A novel method to analyze electromagnetic scattering of complex objects. *IEEE T. Electromagn. C.*, 24:397–405, 1982.

[125] J. C. E. Underwood. *General and systematic pathology*. Churchill Livingstone, 2004.

[126] P. Wang, R. K. Bista, W. E. Khalbuss, W. Qiu, S. Uttam, K. Staton, L. Zhang, T. A. Brentnall, R. E. Brand, and Y. Liu. Nanoscale nuclear architecture for cancer diagnosis beyond pathology via spatial-domain low-coherence quantitative phase microscopy. *J. Biomed. Opt.*, 15:066028, 2010.

[127] World Health Organization. *Cancer [Fact Sheet No. 297]*, 2012 edition.

[128] World Health Organization. *Histological typing of lung tumours*, 1982.

[129] C. H. Yang and J. Mertz. Transmission confocal laser scanning microscopy with a virtual pinhole based on nonlinear detection. *Opt. Lett.*, 28:224–226, 2003.

[130] K. Yee. Numerical solution of initial boundary value problems involving maxwell's equations in isotropic media. *IEEE T. Antenn. Propag.*, 14:302–307, 1966.

[131] I. T. Young. Quantitative microscopy. *IEEE Eng. Med. Biol.*, 15:59–66, 1996.

[132] S. H. Yuspa. Overview of carcinogenesis: past, present and future. *Carcinogenesis*, 21:341–344, 2000.

VITA

Ryan L. Coe

Address: 2512 E. Madison St. Apt. 305, Seattle, WA 98112
Email: ryancoe@uw.edu | Web: www.linkedin.com/in/ryancoe

EDUCATION

Bioengineering, University of Washington 2008 - 2013
Doctor of Philosophy in Dr. Eric J. Seibel's Human Photonics Laboratory

Foster School of Business, University of Washington 2010 - 2013
Technology Entrepreneurship Certificate

Biomedical Engineering, University of Virginia 2004 - 2008
Bachelor of Science in Biomedical Engineering with Distinction

PROFESSIONAL EXPERIENCE

VisionGate, Inc. (www.visiongate3d.com) 2008 - 2013
Research Assistant

- Developing a novel 3D microscope for the early detection of cancer
- Coordinating efforts to develop quantitative microscopy techniques through use of a computer simulation to optimize the microscope
- Work performed as part of a collaborative effort with the Human Photonics Laboratory at the University of Washington

Applied Precision, Inc. - GE Healthcare (www.api.com) Summer 2012
General Electric Early Identification Program Intern

- Implemented the foundation for an objective quality assurance program for super resolution microscopes
- Work performed in conjunction with Engineering Innovation Fellowship Program

PocketSonics, Inc. (www.pocketsonics.com) Spring 2006
Research Assistant

- Worked on developing a novel, ultra-portable ultrasound device for point-of-care guidance of vascular access
- Facilitated implementation of ultrasound image processing

ACADEMIC RESEARCH

Bioengineering, University of Washington 2008 - 2013
Research performed in Eric J. Seibels Human Photonics Laboratory
Thesis: *Computational Modeling of Optical Projection Tomographic Microscopy*

- Developing and employing simulation to optimize microscope imaging parameters and to develop quantitative microscopy techniques for the early detection of cancer
- Assisted in writing a successful grant on quantitative OPTM worth ~$325k
- Virtual School of Computational Science and Engineering - Petascale Programming Environments and Tools (July 2010)

Biomedical Engineering, University of Virginia 2004 - 2008
Research performed in William F. Walkers Ultrasound Laboratory
Thesis: *Software Design of Portable and Generic Routines for Motion Estimation*

- Developed and validated a novel motion estimation algorithm
- Assessed accuracy of elastography algorithm for non-invasive tumor detection

TEACHING EXPERIENCE

Contemporary Light Microscopy and Biophotonics Spring 2009 *Teaching Assistant*

- Designed and taught two theoretical and hands-on image processing lectures for 30 person graduate level class
- Assistant in Laboratory section aimed at building microscopes
- Grading homework and tests for class

UNDERGRADUATE ADVISING

Sirena Merfalen

- Research Project: Quantitative standards to assess Fluorescent photobleaching

Kenny Chou

- Research Project: Enhancing computational performance of image dilation with a CUDA enabled GPU
- Research Project: 3D imaging of Fine Needle Aspirates using Optical Projection Tomographic Microscopy
- Participated in Undergraduate Research Symposium in 2011 and 2012
- Received two Washington Research Foundation (WRF) Fellowships worth $12k

LEADERSHIP

Science and Engineering Business Assoc. (www.uwseba.com) 2009 - 2013
Executive management in student operated non-profit organization bridging the gap between scientists and the business community

- VP of Finance: Executed board approved budgets with prompt collection and dispersion of payments for the organization, classified as a 501(c)(6) non-profit
- Career Fair Coordinator: Coordinated the University of Washingtons largest career fair, with 120 companies in attendance, generating $84k gross profits
- Officer of Membership/VP of Membership: Revamped the membership process, increasing the number of active members by 33%

VOLUNTEER EXPERIENCE

Youth Tutoring Program 2009 - 2011

- Tutoring for five low- and mixed-income public housing communities in partnership with the Seattle Housing Authority
- Serving as a role model helping to provide a safe, positive, and stimulating environment where students explore learning and experience academic and personal success

Martha Jefferson Hospital 2006 - 2007
Madison House Medical Extern - Operating Room

- Observed differences between private and academic hospitals
- Learned state of the art sterilization techniques for surgical settings

University of Virginia Hospital 2005 - 2006
Madison House Medical Extern - Thoracic Cardiovascular Post Operative Unit

- Acquired clinical knowledge about cardiac medical devices
- Observed cardiac Surgeries

HONORS

- National Science Foundation Graduate Research Fellowship worth ~$180k
- National Science Foundation and American Society of Engineering Education (ASEE) Engineering Innovation Program Fellowship worth $13k
- 1st Place team in the University of Washington Venture Capital Investment Competition

EXTRACURRICULAR ACTIVITES

- Bioengineering Graduate Student Affairs Co-Chair (2009-2010)
- Student Advisory Board to the Department Chair (2009-2010)
- Student Engineering Council (2010)

JOURNAL ARTICLES

1. R.L. Coe and E.J. Seibel, "Improved Beer-Lambert law for high numerical aperture illumination in optical microscopy," submitted for publication, *Opt. Lett.* 2013.
2. R.L. Coe and E.J. Seibel, "Experimental and theoretical analysis for improved microscope design of Optical Projection Tomographic Microscopy," accepted with mandatory revisions, *Opt. Lett.* 2013.
3. K.F. Chou, Q. Miao, R.L. Coe, and E. J. Seibel, "3D imaging of Fine Needle Aspirates using Optical Projection Tomographic Microscopy," *J. Cytol. Histol.* vol. S2:001, 2013.
4. R.L. Coe and E.J. Seibel, "Computational Modeling of Optical Projection Tomographic Microscopy using the Finite Difference Time Domain Method," *J. Opt. Soc. Am. A*, vol. 29(12) pp. 1-12, 2012.
   *Selected for Virtual Journal for Biomedical Optics
5. R.L. Coe and E.J. Seibel, "Improved near-field calculations using vectorial diffraction integrals in the finite-difference time-domain Method," *J. Opt. Soc. Am. A*, vol. 28(8) pp.1776-83, 2011.
   *Selected for Virtual Journal for Biomedical Optics
   *Selected for Labome.Org
6. F. Viola, R.L. Coe, D.A. Guenther, K. Owen, and W.F. Walker, "MUlti-Dimensional Spline-Based Estimator (MUSE) for Motion Estimation: Algorithm Development and Initial Results," *Ann. Biomed. Eng.*, vol. 36 (12) pp. 1942-1960, 2008.

CONFERENCE PAPERS

1. R.L. Coe and E.J. Seibel, "Modeling microsphere axial displacement in optical projection tomographic microscopy to analyze effects on filtered backprojection reconstruction," 2013 SPIE Photonics West, San Francisco, CA, 8592-16.
2. R.L. Coe and E.J. Seibel, "Analyzing the effect of absorption and refractive index on image formation in high numerical aperture transmission microscopy of single cells," 2013 SPIE Photonics West, San Francisco, CA, 8592-23.

3. R.L. Coe and E.J. Seibel, "Application to High Numerical Aperture Image Formation Theory to OPTM," 2012 Engineering Innovation Fellowship Program Conference, Washington DC, USA.
4. F. Viola, D.A. Guenther, R.L. Coe, and W.F. Walker, "Multi-Dimensional Spline-Based Non-Rigid Image Registration," 2007 SPIE Medical Imaging Symposium, San Diego, USA.
5. W.F. Walker, D.A. Guenther, R.L. Coe, and F. Viola, "A Novel Spline-Based Algorithm for Multi-Dimensional Displacement and Strain Estimation," 2006 IEEE Ultrasonics Symposium, Vancouver, Canada.

BOOK CHAPTERS

1. R.L. Coe, Q. Miao, K.F. Chou, M.G. Meyer, and E.J. Seibel (2013). Isometric 3D Imaging of Cellular Samples Using Optical Projection Tomographic Microscopy. In R.K. Wang and V.V. Tuchin (Eds.), Advanced Biophotonics: Tissue Optical Sectioning (1st edition, pp. 581-620). New York, New York: Taylor & Francis.

PUBLISHED IMAGES

1. Cover Image on Advanced Biophotonics: Tissue Optical Sectioning (1st edition), edited by R.K. Wang and V.V. Tuchin, New York, New York: Taylor & Francis (2013).

PATENTS

1. E.J. Seibel, Q. Miao, R.L. Coe, P.G. Reinhall, D.W. Storti, "Optical Projection Tomography Microscope (OPTM) for Large Specimen Sizes." Patent Application No. 13/091,088 submitted 4/20/2011.